NUMERICAL SIMULATION OF LATERAL JETS IN SUPERSONIC CROSSFLOW OF MISSILES USING COMPUTATIONAL FLUID DYNAMICS

A THESIS SUBMITTED TO
THE GRADUATE SCHOOL OF NATURAL AND APPLIED SCIENCES
OF
MIDDLE EAST TECHNICAL UNIVERSITY

BY

EFE CAN DAĞLI

IN PARTIAL FULFILLMENT OF THE REQUIREMENTS
FOR
THE DEGREE OF MASTER OF SCIENCE
IN
MECHANICAL ENGINEERING

JUNE 2019

Approval of the thesis:

NUMERICAL SIMULATION OF LATERAL JETS IN SUPERSONIC CROSSFLOW OF MISSILES USING COMPUTATIONAL FLUID DYNAMICS

submitted by **EFE CAN DAĞLI** in partial fulfillment of the requirements for the degree of **Master of Science in Mechanical Engineering Department, Middle East Technical University** by,

Prof. Dr. Halil Kalıpçılar
Dean, Graduate School of **Natural and Applied Sciences** _____

Prof. Dr. M. A. Sahir Arıkan
Head of Department, **Mechanical Engineering** _____

Prof. Dr. M. Halûk Aksel
Supervisor, **Mechanical Engineering, METU** _____

Examining Committee Members:

Assoc. Prof. Dr. M. Metin Yavuz
Mechanical Engineering, METU _____

Prof. Dr. M. Halûk Aksel
Mechanical Engineering, METU _____

Prof. Dr. Kahraman Albayrak
Mechanical Engineering, METU _____

Assist. Prof. Dr. Özgür Uğraş Baran
Mechanical Engineering, METU _____

Assist. Prof. Dr. Onur Baş
Mechanical Engineering, TEDU _____

Date: 12.06.2019

I hereby declare that all information in this document has been obtained and presented in accordance with academic rules and ethical conduct. I also declare that, as required by these rules and conduct, I have fully cited and referenced all material and results that are not original to this work.

Name, Surname: Efe Can Dağlı

Signature:

ABSTRACT

NUMERICAL SIMULATION OF LATERAL JETS IN SUPERSONIC CROSSFLOW OF MISSILES USING COMPUTATIONAL FLUID DYNAMICS

Dağlı, Efe Can
Master of Science, Mechanical Engineering
Supervisor: Prof. Dr. M. Halûk Aksel

June 2019, 120 pages

In this thesis, numerical simulation method for modelling lateral jet in supersonic crossflow is presented. Lateral jet control provides high maneuverability to the missile at difficult flow conditions. Besides, jet in a crossflow case has a highly complicated flow domain which should be examined using numerical or experimental methods. In this study, numerical methods are used. The thesis consists of two main sections. In the first section, a validation study is conducted for numerical simulation method using experimental results of a generic missile geometry with lateral jet from literature. First, grid independency and turbulence model studies are conducted for validation model. In the turbulence model study k-ε Realizable and k-ω SST turbulence models have been used and results show that, k-ε Realizable model results in closer results to the experimental data. Moreover, surface pressure distribution data from experiment is used for validating numerical simulation method. Hence, results of the numerical simulation are in a good agreement with the experimental results except for some deviations at the recirculation region. In the second section, a parametric study is conducted for generating a database of jet and crossflow interactions using the validated numerical simulation method. In the parametric study, a slender missile geometry with lateral jet is used. Examined parameters are jet location, jet spouting

angle, free-stream and jet flow velocity, and incidence angle. It is seen that, spouting jet normally results in best maneuverability. Furthermore, jet locations result in varying performance depending on the free-stream flow velocity. Once for all, jet flow Mach is inspected and seen that, jet performance depends strongly on jet flow Mach number.

Keywords: Lateral Thruster, Side Jet, Computational Fluid Dynamics, Fluent

ÖZ

SÜPERSONİK ÇAPRAZ AKIŞ İÇERİSİNDEKİ FÜZELERE AİT YANAL JETLERİN HESAPLAMALI AKIŞKANLAR DİNAMİĞİ KULLANILARAK SAYISAL BENZETİMİ

Dağlı, Efe Can
Yüksek Lisans, Makina Mühendisliği
Tez Danışmanı: Prof. Dr. M. Halûk Aksel

Haziran 2019, 120 sayfa

Bu tez çalışmasında, süpersonik çapraz akış içindeki yan jetin sayısal modellenme metodu sunulmuştur. Yan jet kontrolü, zorlu akış koşullarında füzeye yüksek manevra kabiliyeti sağlar. Ancak çapraz akış içindeki yan jet problemi oldukça karmaşık bir akış alanına sahiptir ve bu akış alanının sayısal veya deneysel yöntemler kullanılarak incelenmesi gerekmektedir. Bu çalışmada sayısal yöntemler kullanılmıştır. Bu tez iki ana bölümden oluşmaktadır. Birinci bölümde, literatürden yan jet içeren jenerik bir füze geometrisine ait deneysel sonuçlar kullanılarak sayısal modelleme yöntemi için bir doğrulama çalışması yapılmıştır. Öncelikle, doğrulama modeli için çözüm ağından bağımsızlık ve türbülans modeli çalışmaları yapılmıştır. Türbülans modeli çalışmasında ‘k-ε Realizable’ ve ‘k-ω SST’ türbülans modelleri kullanılmış olup, ‘k-ε Realizable’ modelinin deneysel verilere daha yakın sonuçlar verdiği görülmüştür. Buna ek olarak, sayısal modelleme yöntemini doğrulamak için literatürden yüzey basıncı verisi kullanılmıştır. Doğrulama çalışması, sayısal modelleme ve deney sonuçlarının sirkülasyon bölgesindeki bazı sapmalar haricinde uyumlu olduğunu göstermiştir. İkinci bölümde, jet ve çapraz akışın etkileşimine ilişkin bir veri tabanı oluşturmak için doğrulanan sayısal modelleme yöntemi kullanılarak bir parametrik çalışma gerçekleştirilmiştir. Parametrik çalışmada yan jet içeren narin bir füze

geometrisi kullanılmıştır. Bu kısımda incelenen parametreler; jet konumu, jet püskürtme açısı, serbest akış ve jet akışı hızları ve hücum açısıdır. Jet çıkış düzlemine dik olarak püskürtülen jetin en iyi manevra kabiliyetine yol açtığı görülmüştür. Ayrıca, farklı jet konumlarının performansı, serbest akışın hızına bağlı olarak değişmektedir. Son olarak, jet akışı Mach sayısı incelenmiş ve jet performansının jet akışı Mach sayısına önemli ölçüde bağlı olduğu görülmüştür.

Anahtar Kelimeler: Yanal İtici, Yan Jet, Hesaplamalı Akışkanlar Dinamiği, Fluent

Dedicated to My Family

ACKNOWLEDGEMENTS

I would like to express my deepest gratitude to my supervisor Dr. M. Halûk Aksel for his vital guidance and advice throughout the thesis.

I would also like to thank my manager Dr. Emel Mahmutyazıcıoğlu for her advice and criticism on the course of the study. I also want to thank my colleagues in the Aerodynamics Department of Roketsan for all their help and support during the thesis.

Greatest support and encouragement throughout the study is given by Aslı Taşpolatoğlu, she is the one overcoming the difficulties with me. I am very thankful for her help from the beginning to the end of the study.

I am very grateful to my parents Mrs. Sema Dağlı, Mr. Ünal Dağlı and my brother Mr. Atakan Dağlı for their unreserved love, help, and motivation. They have always supported me without any hesitation. Without them, this work would not be even started.

I want to express my sincere thanks to my friends, Mr. Ozan Şayir, Mr. Emre Gümüşsu, and Mr. Mete Atasoy for their valuable comments and support during this study.

TABLE OF CONTENTS

LIST OF TABLES

TABLES

LIST OF FIGURES

FIGURES

LIST OF ABBREVIATIONS

ABBREVIATIONS

a, α	Angle of Attack
Aftjet	Backward Jet Location
CFD	Computational Fluid Dynamics
CG	Center of Gravity
DNS	Direct Numerical Simulation
Forejet	Forward Jet Location
LES	Large Eddy Simulation
PR	Pressure Ratio
RANS	Reynolds Averaged Navier Stokes

LIST OF SYMBOLS

SYMBOLS

$\vec{A}$	Surface Area Vector
C_A	Axial Force Coefficient
C_N	Normal Force Coefficient
C_m	Pitching Moment Coefficient
C_p	Pressure Coefficient
D	Diameter
dS	Surface Element of the Control Volume
E	Total Energy
F_A	Axial Force
F_N	Axial Force
f_e	Body Force
i, j, k	Unit Vectors in x, y, z Directions
k	Turbulent Kinetic Energy
K_f	Force Amplification Factor
K_m	Moment Amplification Factor
l_{ref}	Reference Length
m	Pitching Moment
$\dot{m}$	Mass Flow Rate

M	Mach Number
$\vec{n}$	Normal of the Surface
P	Pressure
q_∞	Dynamic Pressure
$\dot{q}$	Rate of the Heat Transfer
$\vec{r}$	Vector between Cell Centers
R	Gas Constant
S_{ref}	Reference Area
t	Time
T	Static Temperature
u, v, w	Velocity Components in x, y, z Directions
u_τ	Friction Velocity
V	Volume
$\vec{\vartheta}$	Velocity
W_{i0}	Weight Matrix
x, y, z	Cartesian Coordinates
y^+	Dimensionless Wall Distance
α	Angle of Attack
Γ_ϕ	Diffusion Coefficient
γ	Ratio of Specific Heats
ε	Turbulent Dissipation Rate

μ	Dynamic Viscosity
μ_t	Turbulent Viscosity
ρ	Density
τ_{ij}	Viscous Stress Tensor
Ω	Small Portion of the Control Volume
τ_w	Wall Shear Stress
ϕ	Roll Angle
ψ	Spouting Angle
ω	Specific Dissipation Rate
∇	Gradient Operator

Subscripts

f	Face
inf, ∞	Free-stream
jet	Jet Flow
jet-i	Jet and Free-Stream Interaction
0	Total (Stagnation) Properties

CHAPTER 1

INTRODUCTION

Maneuver capability is crucial for a missile since its aim is to hit the target. Hence, a missile should be controllable during the cruise and precise at the endgame. Maneuver capability is achieved by several control techniques. The conventional technique is aerodynamic control surfaces, however, that highly depends on free-stream flow, i.e., at high altitudes and/or low-speeds effectiveness of surfaces drops abruptly due to low dynamic pressure. In order to deal with the efficiency drop at low dynamic pressures, modern techniques such as thrust vector and side jet control are being used. This study focuses on the side jet control. Furthermore, side jet mounted missiles have high maneuver capability and short response time.

In the near future, side jet control will be used more frequently in the modern missiles due to its advantages over other missile control techniques. Nevertheless, side jet causes a complicated flow field which includes shocks, separations and recirculation regions. Hence, side jet result in strong interferences with other missile components. Hence, modelling side jet and understanding the effects of side jet on the missile aerodynamic performance is vital.

In the first part of the study, complicated flow domain due to jet and free-stream flow interactions for a side jet controlled missile is presented. Also, the missiles that are using side jet control are presented.

In the second part, theory of the numerical simulation is explained. First, Navier-Stokes equations which are the three principal equations of CFD are introduced. Also, the turbulence models and the wall treatment approaches are explained in this section.

In the third part, numerical simulation method is explained in the means of the boundary and initial conditions, grid properties. Grid independency and turbulence model studies are also presented in this section. Moreover a validation study is conducted in this section by using surface pressure distribution experimental data of a supersonic missile model in the study by Gnemmi, (2008). Validation study is resulted in consistent pressure coefficients with the experimental results.

In the fourth part, conducted parametric studies are presented. In this part, a generic slender missile geometry is selected from literature, and a similar missile is modeled with a different length and diameter. Several parameters are examined for two jet locations on the missile geometry from the aspect of missile maneuverability. Examined parameters are jet spouting angle, free-stream flow velocity, incidence angle, jet flow velocity.

1.1. Aim of the Study

Understanding the highly complicated interactions of jet in a crossflow case is essential in order to provide an insight to effect on missile aerodynamic performance. Despite wind tunnel tests can be used in the examination of the missile aerodynamic performance, presenting a reliable numerical simulation method for this aim will result in accelerated and cost-effective design phases. Furthermore, jet performance is highly influenced by flight conditions and jet parameters. A well-organized investigation of these conditions and parameters will provide valuable conclusions.

Hence, the aims of the study can be summarized as,

- Characterize of the jet in a supersonic crossflow flow field
- Present an engineering approach to the modelling of jet and free stream flow interactions instead of wind tunnel tests
- Provide a database for the effects of some parameters on the jet performance which will be an input to the conceptual design phase

In the study, aerodynamic surfaces are excluded from simulations in order to obtain results that are independent of wing parameters. Adding lifting surfaces may cause in dependency of results on the lifting surface parameters such as chord, span, and location relative to lateral jet. Hence, lifting surfaces are excluded from the study, and calculations are made on slender missile geometry.

CHAPTER 2

LITERATURE SURVEY

2.1. Aerodynamic Forces and Moments

An aerial vehicle experiences forces and moments along its flight. Maneuverability and controllability of a missile can be inspected using coefficients of these forces and moments and they are presented on a generic missile configuration in Figure 2.1.

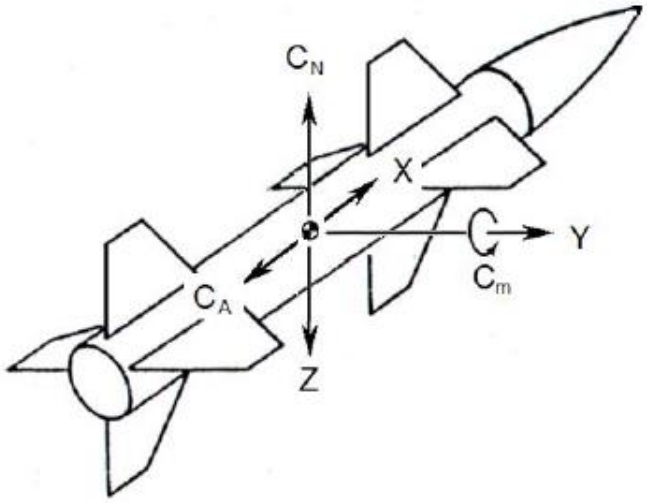

Figure 2.1. Convention for Aerodynamic Forces and Moments (Atak, 2012)

Definition of aerodynamic coefficients are presented below,

$$C_A = \frac{F_A}{q_\infty S_{ref}} \quad C_N = \frac{F_N}{q_\infty S_{ref}} \quad C_m = \frac{m}{q_\infty S_{ref}\, l_{ref}} \tag{2.1}$$

In the Equation 2.1, F_A is the axial force, F_N is the normal force, m is the pitching moment which are the forces and moment used for performance inspections in this study. In the above equations, q_∞ is the dynamic pressure, S_{ref} is the reference area and l_{ref} is the reference length.

2.2. Missile Control Systems

Missiles control their course using mechanisms during their flight. These mechanisms can be grouped into two as, conventional and other control systems. Conventional control systems are aerodynamic control surfaces. In this type of control, attitude control is accomplished by deflecting aerodynamic control surfaces hence generating pressure difference between two faces of the aerodynamic control surface. Pressure difference across two sides of a solid body generates force. One can say that, conventional control systems highly depend on free-stream flow. Depending on the missile body location, there exist three types of control aerodynamic surfaces as, canards, wings and tails. They are shown schematically in Figure 2.2, and canard, wing and tail control missiles are depicted from left to the right.

Figure 2.2. Conventional Missile Control Alternatives (Fleeman, 2006)

For a missile with wing control, control panel loads will be greater since wings should be bigger to compensate maneuverability requirements. For canard control, control surfaces might stall at high angles of attack and cause vortex shedding on the aft-mounted fixed lifting surfaces (such as wings and tails), which creates a roll moment on the aft section of the missile. Tail control would decrease the normal force for a

statically stable missile, however it would not induce roll moment and its control panel loads will be lower than wing and canard control (Fleeman, 2006).

Other control systems are generating desired force directly, even there is no free-stream flow. Two kinds exist in this control systems group, which are thrust vector control and side jet control. Thrust vector control is deflecting rocket motor thrust in desired direction therefore extracting a maneuvering component from rocket motor thrust force. However, rocket motor thrust is used not only for missile propulsion also for attitude control, hence, missile range would decrease in thrust vector control. This should be criticized by the designers according to mission requirements. Three types of thrust vector control are presented in Figure 2.3 including the bold arrows that show thrust force. In Figure 2.3, type of thrust vector control is denoted for each configuration in the reference, however they are cut from image for neatness, and explained in the following. On the left in Figure 2.3, liquid injection in the rocket engine nozzle is presented. In this method, maneuvering force is obtained by changing the flow profile at the nozzle exit. In Figure 2.3, on the middle jet vane and on the right gimballed nozzle are given. For both jet vane and gimballed nozzle types of thrust vector control, rocket motor flow is distorted to obtain a maneuvering component from thrust force.

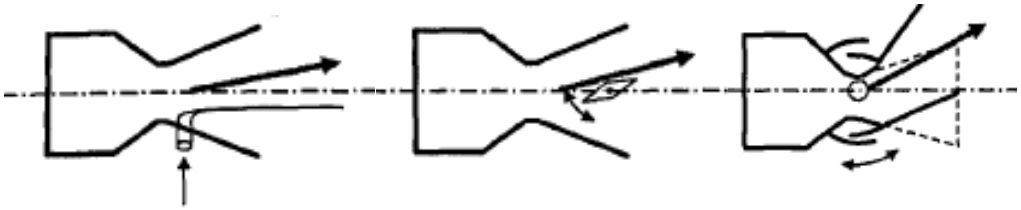

Figure 2.3. Three Types of the Thrust Vector Control (Fleeman, 2006)

Second type of other control systems is side jet control, which can be explained in words as, ejecting high pressure, high velocity gases into the free-stream flow in transverse direction. This system is named in the literature as, lateral (or side) jet,

reaction jet or lateral thruster. In thrust vector control, faster response and smaller miss distance is obtained than aerodynamic control surfaces. Furthermore, in side jet control, faster response and smaller miss distance are obtained than those by thrust vector control (Fleeman, 2006). Schematics of the side jet flow field is presented in Figure 2.4.

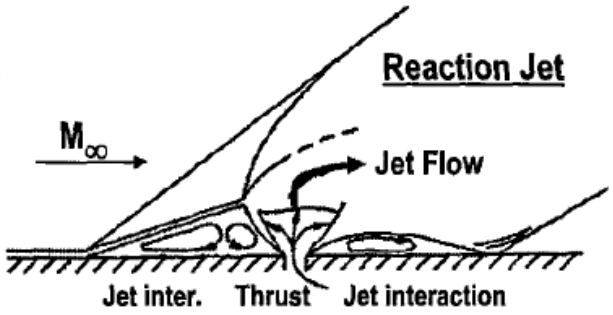

Figure 2.4. Reaction Jet Control (Fleeman, 2006)

In side jet control, desired force is obtained from jet thrust which relies on two mechanisms. First mechanism is momentum transfer, since high velocity gases are ejecting in normal direction which can be analyzed by analytical methods after some assumptions. Second mechanism is interaction of jet and free-stream flows which is more complicated than the first mechanism and should be examined by numerical methods or experiments. Ejected gas forms a plume around side jet exit, which behaves as an obstacle in the cross-flow. Due to obstruction behavior, a shock wave occurs hence high-pressure acts on the missile body at the upstream of the jet. If jet flow is discharging into a supersonic cross-flow, larger interaction forces are obtained than discharging a jet flow at the same flow conditions into the still air (Viti, Wallis, Schetz, Neel, & W. Bowersox, 2004).

Lateral thruster has some superiorities over conventional control systems such as effectiveness at low dynamic pressure which occurs at low speeds or higher altitudes, rapid reaction and high maneuverability. Maneuverability of a missile indicates

missile's capability of changing course of flight. Lateral thruster system combines the short response time with high maneuverability even at low dynamic pressures and high angle of attack. For a conventional control system, high angle of attack cause drastic efficiency drop for the fins that remain in the shadow of other components of missiles such as body itself or other fins.

Lateral thruster is a sub-system of the missile and in order to understand the fundamental principles of this system, patents about lateral thruster system are inspected. First, a patent numbered as US4967982 has been inspected. The system in patent consists of three parts which are propellant chamber, actuator system and jet exit duct. Propellant may be either solid or liquid propellant or compressed gas (US4967982, 1990; US8735788, 2014; Honeywell Inc., 2010; Moog Inc., 2017; Orth & Funk, 1967). If a pressurized gas is used (it can be even air or inert gas such as helium or nitrogen), an electrical or pneumatic valve is necessary as an actuator system in order to pass or block pressurized gas into the exit duct. If solid/liquid propellant is used in the system, an igniter system is required as an actuator to start combustion and then combustion products exhaust into the free-stream. In general, using air or inert gases as propellant results in a simpler system since the ejection of combustion products into the ambient air will sophisticate the system and flow domain. In both cases, exhausting gases to free-stream at supersonic speeds increases system efficiency due to a stronger shockwave at the upstream of the jet exit. Returning to patent US4967982, one designed a system consists of movable jet exit ducts which are attached to hinges and the hinges are parallel to the longitudinal axis of the missile. Ducts in the system are rotating around the hinges in order to obtain thrust in desired direction momentarily with the help of pneumatic actuators or electric motors. Generating thrust in desired direction provides an ability to control pitch, yaw and roll moments. In this study, a system is selected having hinges which are perpendicular to missile's longitudinal axis in order to change direction of the jet thrust and its performance is examined.

As mentioned previously, lateral jet system is an alternative missile control technique. Although it has major advantages over classical aerodynamic control systems (deflecting control surfaces) however it has also some limitations. From a general point of view classical aerodynamic control is simple and reliable, however it has some weaknesses such as,

- There will be a time lag between the steering command and maneuver of the missile. This lag caused by the deflection time of the control surfaces due to mechanical reasons and generation time of the aerodynamic forces caused by the new airframe.
- Generated aerodynamic forces are dependent on the velocity and altitude of the missile. In initial phase of flight (low velocity) and in the homing phase (higher altitudes), dynamic pressure is low and therefore, classical control is less effective than the other phases.

Lateral thruster control overcomes these problems; however, it has also some limitations such as,

- When pressurized gas or liquid/solid propellants are used, missile control by lateral thrusts are disabled after the consumption of the propellant. Hence, the lateral thruster system is suitable for short range missiles (anti-tank missiles) or short operational times such as in the terminal phase. This problem can be eliminated by using large amounts of propellants (THAAD) or combining the lateral thruster system with a classical aerodynamic control system. (PAC-3, ASTER)
- Although the consumption of propellant will cause a minor change in the location of the center of gravity; missile designer should take this change into consideration.

  Use of lateral thruster would cause a very complex flow physics around missile. Effect of the disturbed free-stream flow on the aerodynamic performance of the missile should be examined by using experimental or

validated numerical methods such as wind tunnel tests and CFD solutions (P. Champigny, 1994).

Missiles that are using lateral thruster are also presented in this section. First example is PAC-3 missile by the American Lockheed Martin company and it uses lateral thruster together with conventional aerodynamic control (Fleeman, 2006).

Figure 2.5. PAC-3 Missile (Lockheed Martin, n.d.)

French ASTER and American SM-3 Standard Missile are using all control variants as a combination. At the beginning of the flight after launch, control is achieved by movable nozzle type thrust vector control, while conventional aerodynamic control is being used during the middle phase. Consequently, at the end-game lateral jet control is used to obtain high maneuverability (Fleeman, 2006; Honeywell Inc., 2016; P. Champigny, 1994). Photograph of the ASTER missile is presented in Figure 2.6.

Figure 2.6. ASTER Missile (MBDA Systems, n.d.)

American THAAD missile does not use conventional aerodynamic control and it uses movable nozzle type thrust vector control at the launch phase and middle phase. Additionally, lateral thruster system is mounted on the missile for precise hit at high altitude (Fleeman, 2006). A photograph taken during the test fire of THAAD missile, is presented in Figure 2.7, and one can barely notice the lateral thruster plumes in the photograph.

Figure 2.7. THAAD Missile (Global Security, n.d.)

Lateral thruster is also mounted on CAMM missile by MBDA Missile Systems. A stacked picture from the test firing of the missile is presented Figure 2.8. It is obtained by combining photographs of different instants of test launch, and it shows the effectiveness of a lateral thruster system.

Figure 2.8. Test Firing of CAMM Missile (Defense Industry Daily, n.d.; Pakistan Defence, 2012)

2.3. Location of the Jet

There exist two possible scenarios for using a lateral jet on a missile which is presented schematically in Figure 2.9 (Lee, Min, & Byun, 2004).

First option is installing lateral thruster at the same location with the center of gravity of the missile along longitudinal axis. In this option, missile shifts its trajectory without changing its attitude.

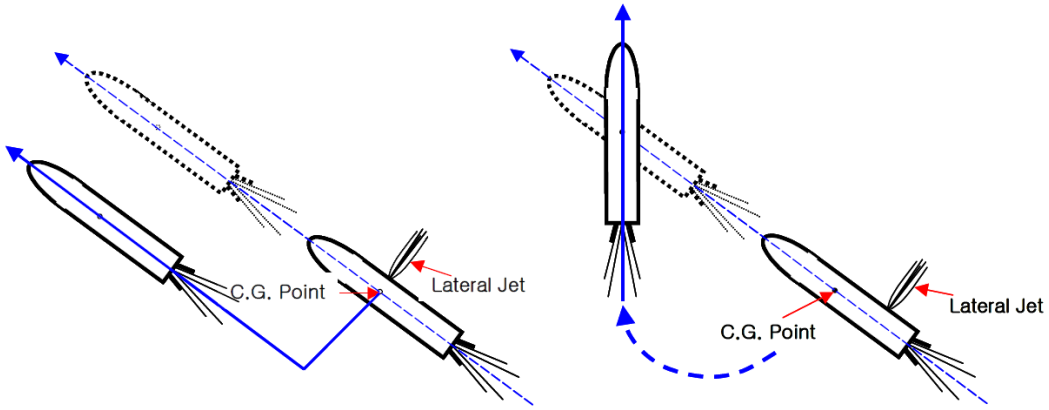

Figure 2.9. Lateral Thruster Locations

Another option is locating the side jet at a certain distance from the CG of the missile. In this option, jet thrust creates a moment about missile's center of gravity. In the first option, side jet efficiency is expected to be low since missile is moved laterally therefore a lateral drag is expected to act on the missile. However, in the first option the seeker of the missile would not lose the target while agile maneuvering takes place (P. Champigny, 1994). In the second option, missile changes its attitude to head towards the target hence missile do the maneuvering action using its own velocity therefore maneuvering takes place much faster than the first option.

2.4. Aerodynamic Interference between Jet and Free-stream Flows

Interactions can be grouped under two as, local interactions and downstream interactions. Local interactions occur around jet exit due to the behavior of the jet plume as an obstruction to the external flow and manipulate the surface pressure in the vicinity of the jet exit. Downstream interactions occur at a distance from jet exit due to the jet plume wake and affects the aerodynamic surfaces (wings, tails etc.) if they are located ahead of the jet. Local and downstream interactions shown schematically in Figure 2.10.

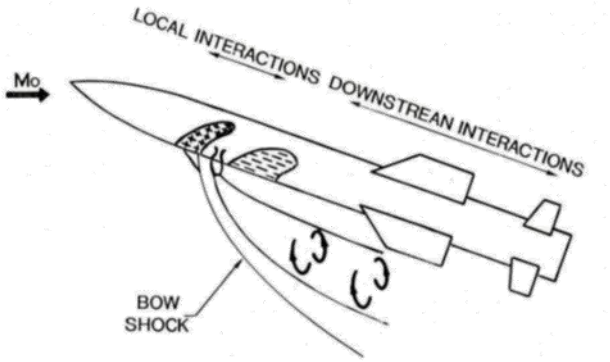

Figure 2.10. Free-stream Jet Plume Interactions (P. Champigny, 1994)

Local interactions will be examined first. As mentioned before, jet plume behaves as an obstruction to the free-stream flow. When the free-stream flow is supersonic an intense shock occurs, which is named as a bow shock in the literature and can be observed from Figure 2.11. In the figure, name of the some labels are slightly altered in order to adapt the figure into the text. The shock is 3-dimensional and wrapped by a mixing layer which is also 3-dimensional. Also due to supersonic free-stream flow separation occurs at the upstream of the jet exit. Near the jet plume, Mach disk can be observed from schematics and Schlieren photograph of the flow domain. Mach disk occurs due to under expanded axisymmetric jets which are discharging into the stationary free-stream. If such a case occurs in a supersonic free-stream, Mach disk moves towards downstream of the jet. Flow field of the jet in a crossflow case is similar to the one of the secondary injection thrust vector control. Separation region, bow shock, Mach disk and recirculation region are common in both flow domains (Erdem, 2006). Now, detailed examinations will be made for mentioned flow occurrences.

- Bow shock and separation region

  Due to high adverse pressure gradient of the jet flow, separation shock occurs. Also, jet plume acts as an obstacle to the free-stream flow, hence a bow shock forms. With increasing jet pressure or decreasing free-stream Mach number,

distance between the jet exit and bow shock increases. Likewise, separation region which occurs at the upstream of the jet, becomes larger, when jet pressure increases, as expected (P. Champigny, 1994).

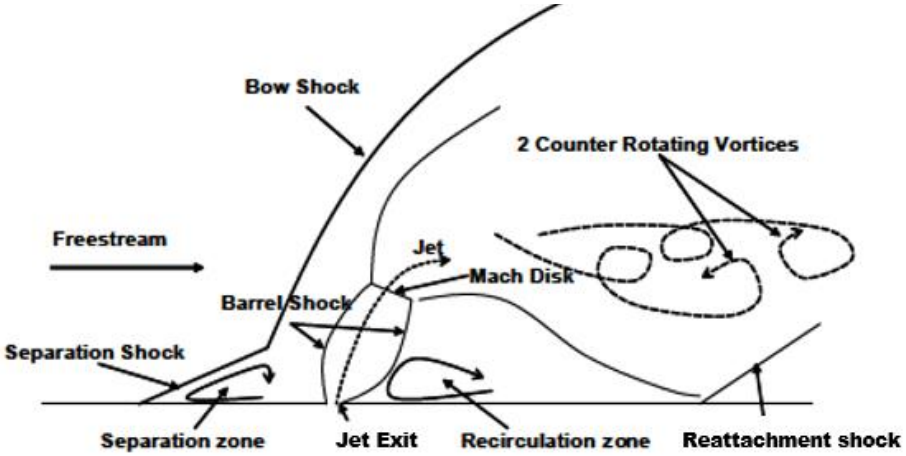

Figure 2.11. Flow Field Schematics (Lee, Min, & Byun, 2004)

- Mach disk and Barrel Shock Concept

  In Figure 2.11, one can notice the barrel shock and Mach disk in the flow field schematics. They should be explained in order to get a better insight to these concepts. For a plume, if exit pressure is higher than the that of free-stream flow, it is called under expanded. An under expanded jet plume and free-stream flow interactions are presented in Figure 2.12.

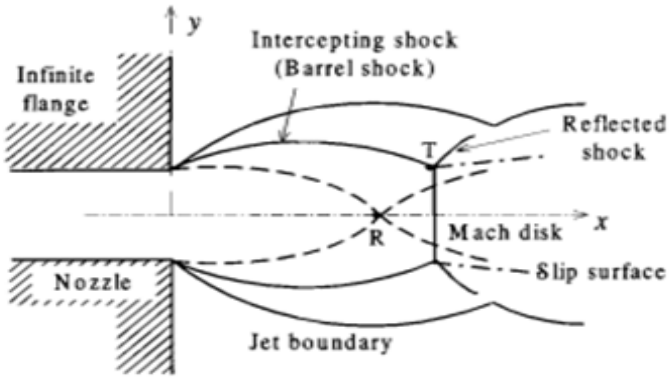

Figure 2.12. Flow Structure of the Under-expanded Jet Plume (Irie, Yasunobu, Kashimura, & Setoguchi, 2003)

An under expanded jet plume goes through expansion waves at the jet exit. Expansion waves cause the flow to deflect outwards from the jet exit, hence, jet boundary expands first, as can be noticed from Figure 2.12 (Edgington-Mitchell, Honnery, & Soria, 2014). Expansion waves reflect as compression waves from constant pressure jet boundary at almost constant angle and due to interception of these waves a barrel shock forms. For highly under expanded jets (ratio of jet to the free-stream pressure is high), a normal shock occurs perpendicular to jet centerline. For highly under expanded jets, barrel shock interacts with a normal shock (Mach disk) at point T and reflects as reflected shock. The highly under expanded jet case is shown in Figure 2.12 with solid lines. Consequently, velocity of the main flow drops across the Mach disk. If pressure ratio is decreased up to some point, Mach disk does not occur. This situation is represented with dashed lines in Figure 2.12. Since Mach disk does not exist, barrel shock intersects with itself at point R and at the downstream it continues compression-expansion and so on (Arnold Engineering Development Center, 1976; Chang & Chow, 1974; Edgington-Mitchell et al., 2014; Irie et al., 2003).

In general sense, the location of the Mach disk is important since it is giving an idea about the jet flow path. Increasing the free-stream Mach number or inclining the jet with a cant angle towards downstream is expected to move

Mach disk towards downstream. Also, with an increasing Mach number or pressure of the jet flow, Mach disk may move away from the jet exit (P. Champigny, 1994).

- Recirculation region

  At the downstream of the jet, another separation region can be observed. In this region, pressure and velocity are lower than the free-stream conditions which occur due to jet plume wake. At the downstream of the recirculation region, reflected shock impinges on the wall causing the reattachment shock as shown in Figure 2.11. The reattachment shock forms to make flow parallel to wall. (Ağsarlıoğlu, 2011; Cassel, 2003; Christie, 2010).

- Pressure distributions

  Surface pressure distribution has major importance since it shows the regions improving or reducing the jet performance. Also, lateral jet CFD solutions should be validated using the experimental data for surface pressure distribution.

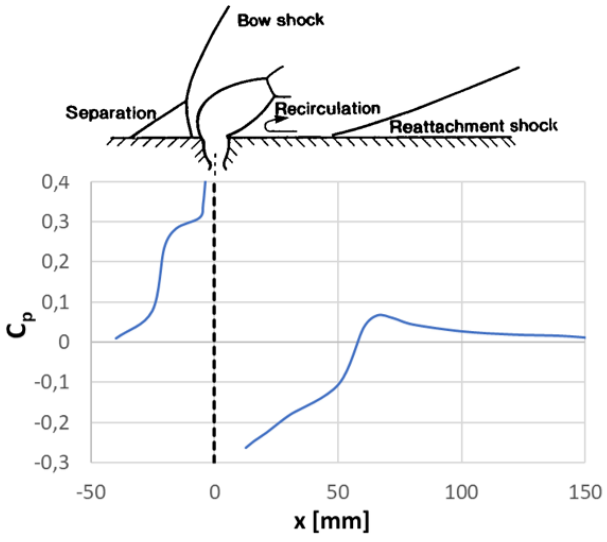

Figure 2.13. Surface Pressure Distribution (P. Champigny, 1994)

A characteristic pressure distribution for a lateral jet in a supersonic cross-flow is presented in Figure 2.13. Data of Figure 2.13, is taken from the notes of Champigny et al., but it is replotted again for neatness, while schematics are used directly from the reference. C_p values are the experimental results obtained from an under expanded lateral jet operating in a supersonic free-stream. Examining the figure, at the upstream of the jet due to interaction of jet and free-stream flow high pressure values are observed in the experiments. Moving away from the jet, first recirculation region is observed at the downstream region, and low pressures occur here as expected. Moving further in the downstream region, reattachment shock occurs and as a result, surface pressure increases here again but not as much as in the upstream region (Spaid & Zukoski, 1968).

Further examination of the flow field will be made using a Mach contours of a side jet case obtained by a numerical simulation from literature. Lateral jet is exhausting at sonic velocity into a supersonic free-stream at a Mach number of 4.0, with a ratio of total jet pressure to static free-stream pressure being around 500. Examining Figure 2.14, one can observe that barrel shock, Mach disk, bow shock, reattachment shock are all visible. Although names of some the flow occurrences slightly differ from the ones used so far in this study due to being from another source, they are still cognizable.

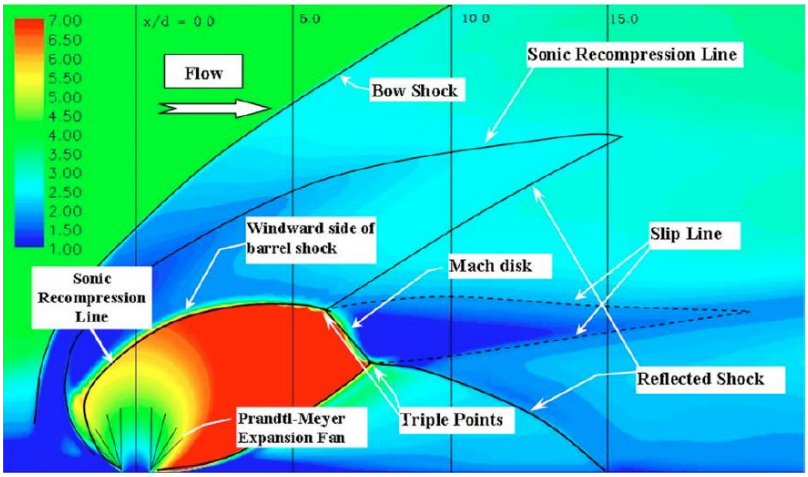

Figure 2.14. Inspection of the Flow Field in Detail (Viti, Neel, & Schetz, 2009)

Some additional comments can be made using Figure 2.14. At the vicinity of the jet exit back pressure is not homogenous unlike the case presented in Figure 2.12 which is exhausting to a still free-stream. For the current case, the pressure is greater in the windward side of barrel shock than the one in the leeward side, hence barrel shock is not symmetric around its axis. Moving further downstream of the jet, flow velocity decreases from supersonic speed to the subsonic speeds after the Mach disk as explained before. But there is an additional observation that should be pointed out, two lines enclosing the subsonic flow at the downstream of the Mach disk which are extending from the two ends of the Mach disk named as slip lines in the literature.

Jet pressure has a significant effect on the surface pressure distribution. With an increasing jet pressure, jet plume becomes a stronger obstruction such as, bow, separation and reattachment shocks get stronger gradually together with the recirculation region. Therefore, high and low-pressure values and the regions where these pressures occur, grows further (P. Champigny, 1994).

Another parameter effecting jet performance is, shape of the jet exit and it is examined in literature in various studies (P. Champigny, 1994; Zhang, Cai, & Cui, 2009). One comparison consists of circular and rectangular (may be elliptic also) jet exit shapes orientated in the streamwise direction, both having the same area. Circular jet exit generates a bigger jet obstacle and that results in larger disturbances such as recirculation and separation regions. Also, high pressure region occurring in front of the jet is bigger when a circular jet is used which has a positive effect on jet performance obviously. On the contrary, a rectangular/elliptic shaped jet located perpendicular to the streamwise direction creates a greater jet obstacle than the circular jet and the effect of the larger jet plume should be similar to the first case. Therefore, shape and orientation of the jet exit has a significant effect on the jet exit performance and should be considered. Local interactions are examined so far. Next, downstream interactions will be examined. Downstream interaction consists of vortices and a wake which are shown in Figure 2.15.

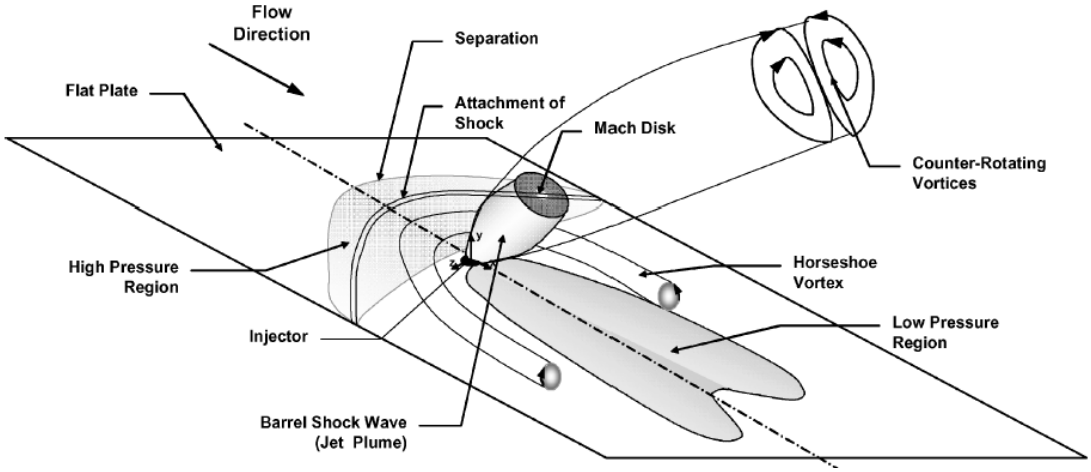

Figure 2.15. Three-dimensional Schematics of the Jet and Cross-flow Interactions (Viti et al., 2004)

In Figure 2.15, side jet and crossflow interaction on a flat plate is shown, since the flow fields for a flat plate and a body of revolution at zero incidence angle are close to each other. In the figure, separation, Mach disk, jet plume, and barrel shock are shown again. However, the attention is to the vortices and wake in this case. With a further examination of the three-dimensional schematics of the interactions, a couple of counter-rotating vortices is noticed. These vortices occur due to the of the free-stream flow, and they expand from the jet exit (Jacquin, 1994; P. Champigny, 1994). Likewise, secondary vortices are noticed in the schematics and this vortices are named as horseshoe vortices in the literature. Horseshoe vortices occur around the wings of an airplane in chordwise direction, around the bluff body of a submarine and even around a bluff body such as cylinder or rectangular prism mounted vertically on a horizontal plate. Explanation will be provided on a flat plate and a body which is a closer example to side-jet flow field interaction, although the explanation is the same for all cases obviously. In the formation of a horseshoe vortex, a free flow is approaching the obstruction with a developed boundary layer due to no-slip walls and this boundary layer copes with the tough adverse pressure gradient due to obstruction in the flow field. This results in a flow separation very close to the obstacle and plate conjunction and the separation forms a vortex which elongates around the obstacle.

The name of the vortex is given because of its shape (Eckerle & Langston, 1986; Lin, Ho, & Dey, 2008). In the jet in a cross-flow case, the analogy between the jet plume and obstruction explains the horseshoe vortex system formation. Similarly, boundary layer of the free-stream flow on the missile body walls draws closer to the jet and faces adverse pressure gradient. Due to this pressure gradient boundary layer wraps up as shown in Figure 2.15 also. Horseshoe vortex phenomenon depends on Reynolds Number and the ratio of jet and free-stream velocity (Sau, Sheu, Hwang, & Yang, 2004).

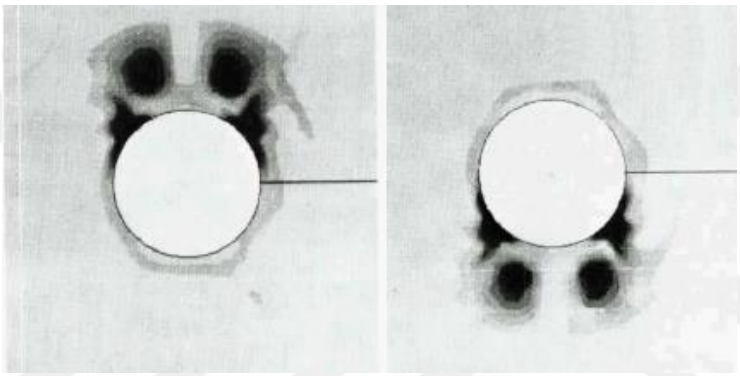

Figure 2.16. Total Pressure Contours of a Cylindrical Body without Jet (α=10, -10 from left to right) (P. Champigny, 1994)

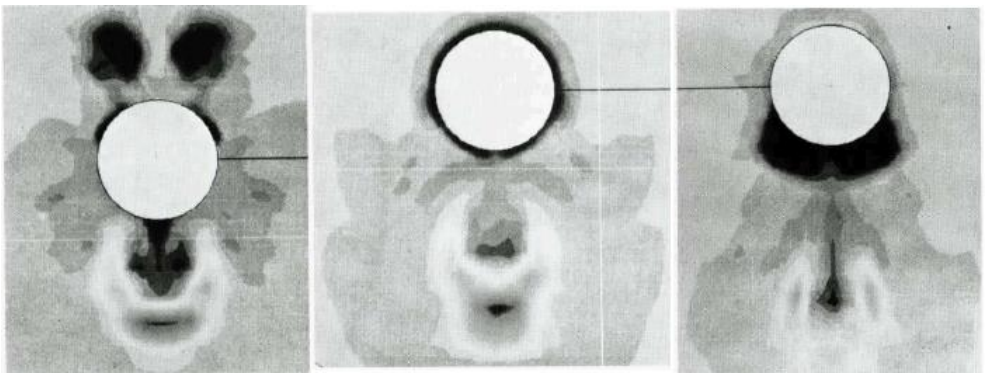

Figure 2.17. Total Pressure Contours of a Cylindrical Body with Jet (α=10,0,-10 from left to right) (P. Champigny, 1994)

One can estimate jet trajectory by examining local maximums of total pressure and temperature. Besides, vortices trajectory can be estimated by maximum vorticity locations (P. Champigny, 1994).

Effect of angle attack on the vortices occurring due to the interaction of a free-stream and jet flow can be examined in Figure 2.16 and Figure 2.17, that present the total pressure contours from literature. At positive angles of attack, the jet is at the windward side of the body (the jet is facing to the free-stream flow), jet flow path becomes closer to body. On the other hand, body vortices on the leeward side (which means the side that is opposite of the windward side) are altered to a minor extent. For negative angles of attack, body vortices are altered in such a way that only jet vortices can be observed. However jet vortices are influenced by the negative angles of attack in comparison with the pressure contours of zero incidence.

From another point of view, jet flow can alter the control surface performance significantly. In case of jet exit is in the pitch plane and located at the bottom of the missile, also the control surfaces are mounted in the downstream of the jet, induced lift on the panel will decrease the panel performance due to the low-pressure take place in the jet wake together with velocities of the vortices on the panel (P. Champigny, 1994). For another case, when panels and jet are at the same location along the longitudinal axis, and jet exit is directed towards bottom of the missile again. In this case, panel lifting performance will increase due to high pressure region at the bottom face of the panels (Ağsarlıoğlu, 2011).

Effect of incidence angle on the jet and cross-flow interaction in the pitch plane is examined in Figure 2.18 which is presented by Stahl et al. One can observe from Figure 2.18, with a decreasing incidence angle (from +15 to -10), Mach disk and bow shock are getting closer to the body as expected. On the other hand, at negative incidence angles body shock strongly impacts on the bow shock which can be observed from Schlieren images presented above.

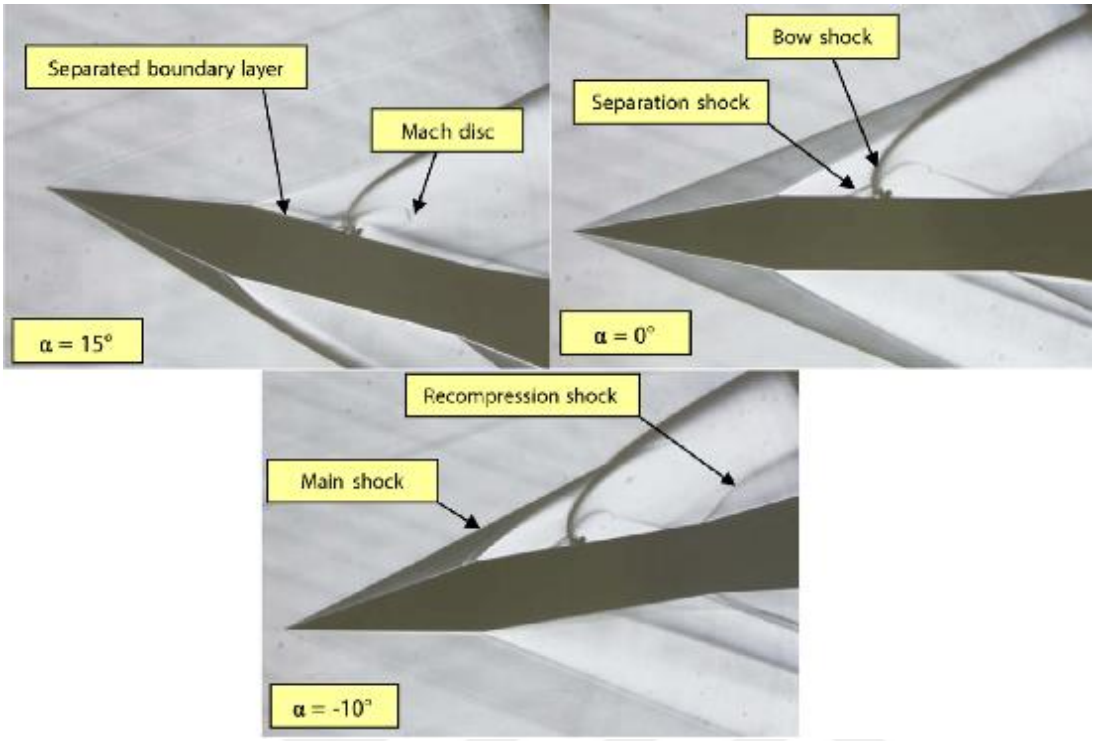

Figure 2.18. Schlieren Images of the Shock Interactions at Different Incidence Angles (B. Stahl, Esch, & Gülhan, 2008)

2.5. Effect of the Interactions on the Side Jet Performance

For a jet exhausting to the free-stream, in the region ahead of the jet the pressure is high and in the region behind of the jet is low as mentioned. High- and low-pressure regions around the jet generate a moment around jet. In the case, side jet is located at the same longitudinal axis location with the center of gravity of the missile indicating that the jet is used only for trajectory shift and moment generation should be avoided. Therefore, when the jet is located around the center of gravity of the missile, moment generation due to interaction forces should be considered. In the case when the jet is located away from the center-of-gravity, moment generation is favorable, therefore, interaction forces affect jet thrust, therefore, the moment of the missile. Since the low-pressure region decreases the moment, it is an idea to install jet at the aft of the missile

body. If the jet is installed at the aft, the low-pressure region is swept towards the end of the missile, therefore interaction forces which have negative effects diminish.

Lateral jet mounted on a missile body in a supersonic free-stream results in high- and low-pressure regions as mentioned above, and generally low-pressure region is larger relative to high pressure region. Therefore, sum of the interaction forces has a negative impact on the jet performance. When jet is mounted on a flat plate, situation is much different than the one in a body of revolution. In this case, high-pressure region is laying on a plane perpendicular to jet axis rather than being wrapped around the missile body, therefore high-pressure forces have a perpendicular effect on the flat plane. However, in practical applications, a body of revolution is being used as a missile body rather than a flat plate.

As mentioned before, jet exit shape influences the jet performance. When a slender jet exit shape being used, jet performance affected positively due to downsizing of the low-pressure region. Whereas, increasing size of the jet exit or making its shape blunt when the jet is located at the aft of the missile, increases high pressure region. As a result, jet performance increases without altering the low-pressure region on the body surface in a considerable manner.

In the lateral jet studies a ratio is being used for the performance evaluation, which is the moment/force amplification factor. This ratio indicates whether the jet and free-stream flow interactions affect the jet performance favorably or not. More detailed description on the amplification factor will be given under the 'Methodology' part of the study. Free-stream Mach number also influences the jet performance as expected. And its effect on this performance is shown in the literature using the moment amplification factor. The moment amplification factor is a value to show whether interaction forces are increasing the jet performance or not. For a supersonic missile with a lateral jet mounted at front of the center of gravity of the missile, moment amplification factor increases with increasing free-stream Mach number from 2 to 4.5 (P. Champigny, 1994).

The effect of the missile body incidence angle on the side jet performance is inspected in the literature for a tail mounted missile. For a positive incidence angle, where the jet flow is facing free-stream flow directly (windward side), force amplification factor decreases, since influence of the jet wake on the tails increases as the jet plume gets closer to missile aft body for an increasing incidence angle. Inversely, for a negative incidence angle with a jet on the leeward side, force amplification factor increases with decreasing incidence angle of missile body, since interactions are less as the jet plume is driven away from the missile aft-body. Because of the explained physical reason, for negative incidence angles, force amplification factor increases (P. Champigny, 1994).

As stated before, the wake region at the downstream of the jet influences the normal force generated by the tails unfavorably. Hence, force amplification factor decreases. Some studies are conducted in the literature for inspecting this behavior and comments are made using the calculated force amplification factors for each case. For a forward mounted jet, different control surface locations are examined for five different positions. For the most rear location of the panels, force amplification factor is decreased a little bit relative to jet-off situation. When panels move closer to the jet up to a certain location, force amplification factor decreases further since jet wake vortices become stronger for a closer location to jet exit. If panels move to a closer location to jet exit and the distance between the jet exit and panels becomes small, force amplification factor increases relative to jet off condition. Interaction of wing and jet bow shock results in high pressure on panels, therefore amplification factor increases. Mentioned locations are highly case dependent, and it can be affected by many parameters such as flow condition, panel parameters, jet strength and so on. So, one should make a study to inspect the locations for different missile configurations.

2.6. Lateral Jet Studies from Literature

Lateral thruster system draws attention for years due to its advantages over other control systems, so, a variety of studies have been conducted for lateral thruster systems in the literature. The study of Kovar & Schülein, (2006) shows the effect of multiple jet exits orientation on the jet performance. In this study, configurations of a single jet, four jets located collateral and inline are compared while keeping total jet exit area, hence, mass flow rate constant for each model in order to obtain comparable results. Different jet configurations are examined on both flat plate and cylindrical missile body using numerical and experimental methods. For numerical simulations TAU-Code which is developed in DLR is used and also measurements are made in the wind tunnel. Another study presents the comparison of jet exit shapes (Zhang et al., 2009). Circular, elliptic and drop shaped jet exits are examined while keeping the cross-sectional area, hence, the mass flow rate constant. For comparisons, numerical simulations are performed using Fluent. In both studies, comparisons are made by using surface pressure distributions and values of normal force and pitching moment coefficients. In another study (Li, Zhou, Yao, & Fan, 2017), high-pressure nitrogen exhausting through circular, elliptic and rectangular jet exits are numerically simulated using large eddy simulation turbulence model in a code based on Openfoam and flow characteristics are inspected. In a different study, various parameters using a lateral jet installed on a slender missile geometry are studied (Lee et al., 2004). Mass flow rate, spouting angle and circumferential location of the jet, incidence angle of missile body and jet flow pressure effects are investigated using AADL3D code. Another comprehensive study presents the effect of several parameters for a jet mounted on a flat plate obtained by numerical simulations (Zhen, Gao, & Lee, 2013). In this study, using the normal force and pitching moment amplifications, jet temperature, free-stream Mach number and spouting angle effects are investigated.

2.7. Schlieren Image

It is a technique that is used to observe flow in the wind tunnels and Schlieren images of experiments are used in this study for validating CFD solutions and observing the flow in detail. This visualization technique relies on the refraction of the light ray. A light ray moves in a homogenous medium uniformly. But in a non-homogenous medium light refracted due to temperature, density and molecular properties. Shock waves, boundary-layer and separations can be observed by density changes with this method. Setup of an sample Schlieren setup is presented below in Figure 2.19.

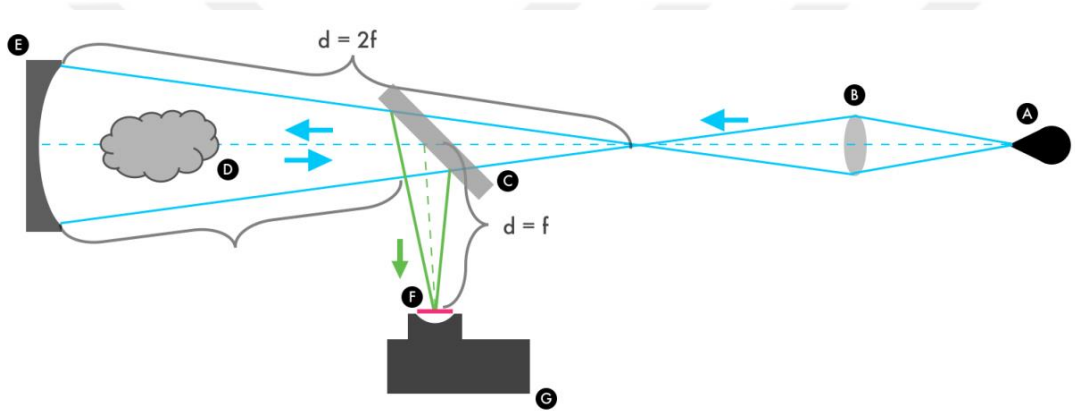

Figure 2.19. Schlieren Imaging Setup (Mazumdar, 2013)

In this figure, components are indicated by the letters. A is the point light source, B is the light condenser lens, C is the half transparent mirror, D is the experiment area, E is the curved mirror and F and G are imaging sections. Parallel light rays pass through a homogenous fluid section uniformly, however, if shock waves are present in flow field light rays are bent at these locations due to density change. Hence, uniform sections of flow-field are white and shock wave, boundary-layer or separation regions are darker due to refraction of light in the image. Furthermore, experimental model does not pass light rays, so the region of test model seems completely dark in the image (Mazumdar, 2013).

CHAPTER 3

METHODOLOGY

3.1. Governing Equations

Fluid flow can be solved analytically using Navier-Stokes equations. To reduce the computational cost of numerical simulations Reynolds Averaged Navier-Stokes (RANS) equations (simplified form of Navier-Stokes equations) are used. And three principal equations of Navier-Stokes which are conservation of mass, momentum and energy as presented below,

- Continuity

$$\frac{\partial}{\partial t}\int_{\Omega}\rho \,\mathrm{d}\Omega + \oint_{d\Omega}\rho(\vec{\vartheta}\cdot\vec{n}\,)\,\mathrm{d}S = 0 \tag{3.1}$$

- Conservation of Momentum

$$\begin{aligned}\frac{\partial}{\partial t}\int_{\Omega}\rho\vec{\vartheta}\,\mathrm{d}\Omega + \oint_{d\Omega}\rho\vec{\vartheta}(\vec{\vartheta}\cdot\vec{n}\,)\,\mathrm{d}S \\ = \int_{\Omega}\rho\overrightarrow{f_e}\,\mathrm{d}\Omega - \oint_{d\Omega}\rho\vec{n}\,\mathrm{d}S + \oint_{d\Omega}(\tau_{\mathrm{ij}}\cdot\vec{n})\,\mathrm{d}S\end{aligned} \tag{3.2}$$

- Conservation of Energy

$$\begin{aligned}\frac{\partial}{\partial t}\int_{\Omega}\rho E\,\mathrm{d}\Omega + \oint_{d\Omega}(\rho E + P)\big(\vec{\vartheta}\cdot\vec{n}\,\big)\,\mathrm{d}S \\ = \oint_{d\Omega}k(\nabla\mathrm{T}\cdot\vec{n})\,\mathrm{d}S + \int_{\Omega}\big(\rho\overrightarrow{f_e}\cdot\vec{\vartheta} + \dot{q}\big)\,\mathrm{d}\Omega \\ + \oint_{d\Omega}(\tau_{\mathrm{ij}}\cdot\vec{\vartheta})\cdot\vec{n}\,\mathrm{d}S\end{aligned} \tag{3.3}$$

In the conservation equations, Ω represents the infinitesimally small portion of the control volume and P is the pressure, E is the total energy, f_e is the body(external) force, $\dot{q}$ is the rate of heat transfer, τ_{ij} is the viscous stress tensor and can be given as,

$$\tau_{xx} = \frac{-2\mu}{3}\left(\frac{\partial u}{\partial x} + \frac{\partial v}{\partial y} + \frac{\partial w}{\partial z}\right) + 2\mu\frac{\partial u}{\partial x} \tag{3.4}$$

$$\tau_{yy} = \frac{-2\mu}{3}\left(\frac{\partial u}{\partial x} + \frac{\partial v}{\partial y} + \frac{\partial w}{\partial z}\right) + 2\mu\frac{\partial v}{\partial y} \tag{3.5}$$

$$\tau_{zz} = \frac{-2\mu}{3}\left(\frac{\partial u}{\partial x} + \frac{\partial v}{\partial y} + \frac{\partial w}{\partial z}\right) + 2\mu\frac{\partial w}{\partial z} \tag{3.6}$$

$$\tau_{xy} = \tau_{yx} = \mu\left(\frac{\partial u}{\partial y} + \frac{\partial v}{\partial x}\right) \tag{3.7}$$

$$\tau_{xz} = \tau_{zx} = \mu\left(\frac{\partial u}{\partial z} + \frac{\partial w}{\partial x}\right) \tag{3.8}$$

$$\tau_{yz} = \tau_{zy} = \mu\left(\frac{\partial v}{\partial z} + \frac{\partial w}{\partial y}\right) \tag{3.9}$$

Reynolds Averaged Navier-Stokes model in three dimensions has five equations for conservation of ρ (continuity), ρu, ρv, ρw (momentum), ρE (energy). Even though, there exist 7 unknows: ρ, u, v, w, E, P and T in the equations. Therefore, one should provide two additional equations such as, ideal gas relation and Sutherland's Law which is a relation for calculating the dynamic viscosity as temperature changes (Blazek, 2001), both are presented below respectively,

$$P = \rho RT \tag{3.10}$$

$$\mu = \frac{1.45\,T^{3/2}}{T + 110}10^{-6} \tag{3.11}$$

where T is temperature in Kelvin and μ is in kg/ms.

Furthermore, stagnation equations are required for identification of compressible flows which are used in following sections of the study for boundary condition definitions. These equations provide stagnation state of the fluid particles which are

assumed as they are brought to rest isentropically (means adiabatic and reversible). Total pressure and temperature relations are presented below,

$$\frac{P_0}{P} = \left[1 + \frac{\gamma - 1}{2} M^2\right]^{\frac{\gamma}{\gamma - 1}} \tag{3.12}$$

$$\frac{T_0}{T} = \left[1 + \frac{\gamma - 1}{2} M^2\right] \tag{3.13}$$

3.2. Turbulence Modelling

Flows are classified as laminar and turbulent flows, where flow characteristic is determined by Reynolds number. In the laminar flow regime, flow is smooth, and particles slide over each other regularly. Also, simple cases with laminar flows can be solved analytically using the continuity and Navier-Stokes equations (Schlichting & Gersten, 2017).

In many flows in engineering applications similar to the one in this study, the interaction between jet and cross-flow has turbulent behavior. Turbulent flows characteristic have a random behavior which involve time dependent fluctuations in three-dimensional velocity vector and flow properties. Direct simulation of these fluctuations results in high computational cost. Therefore, some numerical methods have been developed to capture substantial effects of turbulence so far. There are three different groups of those numerical methods,

3.2.1. Direct Numerical Simulation (DNS)

In this numerical method, mean flow and all fluctuations (eddies) are calculated in the solution process. This method results in a high computational cost, so it cannot be used widely with today's computer technology.

3.2.2. Large Eddy Simulation (LES)

This is an intermediate model between DNS and RANS, which models the effect of large eddies, respectively. This method resolves the respectively large eddies and approximate the small eddies by modelling. LES requires less mesh elements than DNS, it still requires high computation power and it is not suitable for practical engineering applications.

3.2.3. Reynolds Averaged Navier-Stokes (RANS) Equations

RANS focuses on mean flow properties. Since most engineering applications do not require to resolve turbulent fluctuations and mostly mean flow properties are sufficient for modeling flow. Also, it reduces computational cost with respect to the other two numerical methods. Due to reasons mentioned above, RANS is widely used recently and it divides flow variables into mean and fluctuating part as shown in Figure 3.1, and solves governing equations for mean part of the flow properties.

$$\vartheta_i = \bar{\vartheta}_i + \vartheta_i' \qquad P = \bar{P} + P' \tag{3.14}$$

In the Equation 3.14, mean part is denoted with an over bar sign and fluctuating part is denoted by a prime for velocity and pressure.

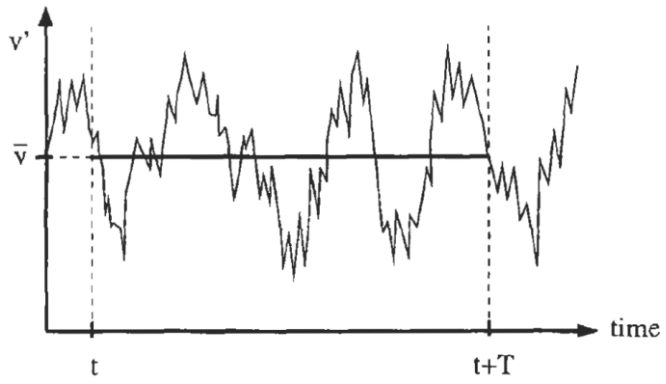

Figure 3.1. Illustration of the Velocity Fluctuations for Turbulence (Blazek, 2001)

Furthermore, flow properties change with mean variables in the conservation of mass and momentum equations and resultant equations as presented below,

$$\frac{\partial \rho}{\partial t} + \frac{\partial (\rho \bar{\vartheta}_i)}{\partial x_i} = 0 \tag{3.15}$$

$$\frac{\partial (\rho \bar{\vartheta}_i)}{\partial t} + \frac{\partial (\rho \bar{\vartheta}_i \bar{\vartheta}_j)}{\partial x_j} = -\frac{\partial \bar{P}}{\partial x_i} + \frac{\partial}{\partial x_j}\left(\mu\left(\frac{\partial \bar{\vartheta}_i}{\partial x_j} + \frac{\partial \bar{\vartheta}_j}{\partial x_i}\right)\right) - \frac{\partial}{\partial x_j}(\rho \overline{\vartheta_i{}' \vartheta_j{}'}) \tag{3.16}$$

Equations 3.15 and 3.16 are the Reynolds Averaged Navier-Stokes equations. In Equation 3.16, which is the RANS form of the momentum conservation equation, there is an additional term $\rho \overline{\vartheta_i{}' \vartheta_j{}'}$. This term is named as Reynolds stress and it stands for the momentum transfer caused due to the fluctuations. In the modeling of Reynolds stress terms, there are two different methods which are the Boussinesq and Reynolds stress models.

According to Boussinesq hypothesis, turbulent shear stress can be related to the mean rate of deformation, which is widely used in solutions and the equation for Reynolds stress term is presented below,

$$-\rho \overline{\vartheta_i{}' \vartheta_j{}'} = \mu_t \left(\frac{\partial \vartheta_i}{\partial x_j} + \frac{\partial \vartheta_j}{\partial x_i}\right) - \frac{2}{3}\delta_{ij}(\rho k + \mu_t \frac{\partial \vartheta_k}{\partial x_k}) \tag{3.17}$$

Where μ_t is turbulent viscosity which is not a characteristic property of fluid, but it is a property effected by local conditions and *k* represents turbulent kinetic energy. Boussinesq hypothesis is used in the Spalart-Allmaras, *k*-ε and *k*-ω turbulence models. In the Spalart-Allmaras model one extra transport equation, in *k*-ε and *k*-ω models two extra transport equations are solved for the calculation of turbulent viscosity. In the Reynolds stress model seven extra transport equations are solved for 3D cases. Therefore, Boussinesq approach is more effective in terms of calculation cost which is base reason for its wide usage in industrial applications.

3.2.3.1. Realizable k-ε Model

In k-ε models k is turbulence kinetic energy, and ε is its dissipation rate. Both are used in the calculation of turbulent viscosity (μ_t). Realizable model is an improvement over standard k-ε model, which provides good results in the cases of jets, channel and boundary layer flows and separated flows.

3.2.3.2. k-ω SST Model

In k-ω turbulence models, k (turbulence kinetic energy) and ω (specific dissipation rate) are being used in the calculation of turbulent viscosity (μ_t). Shear stress transport (SST) model is an improvement over standard k-ω model which is more reliable for adverse pressure gradient flows, transonic shock waves and airfoils. While k-ω models are in use, Fluent automatically switches on enhanced wall treatment or wall function approach depending on the quality of the mesh. Mesh quality is determined with respect to first mesh element height which is closest to wall. Importance of the first element height for numerical solutions will be mentioned in the following parts of this section.

In addition to turbulence models, near wall modeling has a crucial effect on the fidelity of the CFD solution. Flow behavior near the wall can be divided into three regions as in shown Figure 3.2.

The region nearest to wall named as the viscous-sublayer, where flow is laminar and thus molecular viscosity has the major effect. Another region is the fully turbulent region which is far from the wall with respect to viscous-sublayer. In this region, flow is fully turbulent therefore turbulence effects should be taken into consideration. There is a transition region between these two layers and this region is called as buffer layer. In the buffer layer, molecular viscosity and turbulence effects are both important.

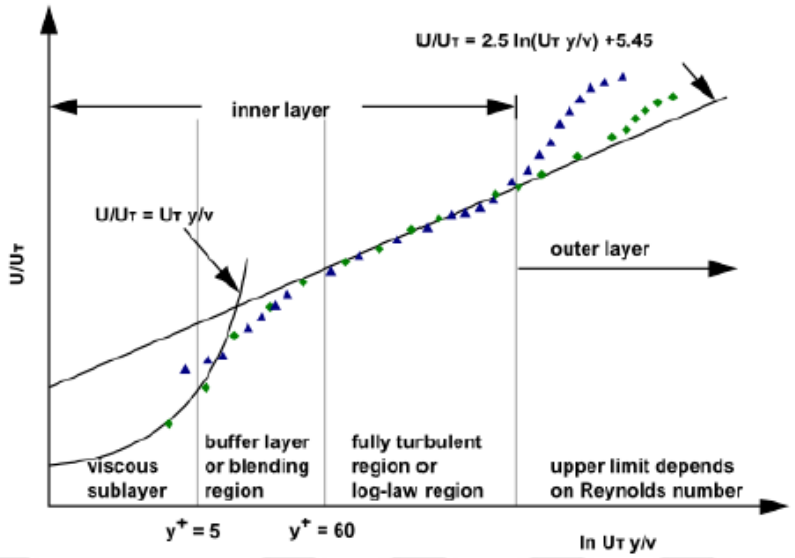

Figure 3.2. Near-wall Flow Characteristics (Ansys Inc., 2013)

In Figure 3.2, y^+ defines the distance between wall and the first grid node which is located closest to the wall. Since gradients are very high in the boundary layer, the first element distance from the wall should be kept small in order to capture these gradients. To be able to generalize this concept a parameter y^+ has been defined and calculated with the following formula,

$$y^+ = \rho u_\tau y/\mu \tag{3.18}$$

In Equation 3.18, u_τ is the friction velocity and that is calculated by the following formula involving τ_w which is wall shear stress,

$$u_\tau = \sqrt{\tau_w/\rho} \tag{3.19}$$

In general, there exist two approaches for modeling near wall behavior, which are wall function approach and enhanced wall treatment. In the wall function approach, the height of the first mesh element that is closest to wall, should be less than the height of the boundary layer. However in this approach previously mentioned viscous-

sublayer and buffer layer is not solved. For that reason, y^+ should be between 30 and 300 in order to set the first grid cell which is closest to wall in the fully turbulent region. In the enhanced wall treatment approach y^+ should be kept around 1 for solving boundary layer completely involving viscous-sublayer, buffer layer and fully turbulent layer.

3.3. Details of the Numerical Solver

Fluent which is a commercial numerical solver have been used in this study. Fluent solves the governing equations with an appropriate turbulence model for numerical solution.

In CFD solvers, there exists two numerical solution methods in general which are density and pressure-based solvers. Initially pressure-based solver has been created for low speed incompressible flows and then density-based solver have been generated for high speed compressible flows. Both solvers have been improved further for solving wide ranges of flows. Density based solver uses continuity equation for calculating the density distribution and than the equation of state to obtain pressure distribution while pressure-based solver uses pressure equation for calculation of pressure distribution which is the manipulated form of the continuity and momentum equations.

Both methods use a technique which is based on control-volume approach. In this approach, the flow domain is divided into ‘control-volumes’ using the generated grid, a discrete unknowns like pressure, velocity, temperature and some scalars are obtained for those control-volumes by integrating governing equations individually. Discretized equations are linearized and then solved for obtaining new values of these unknowns. In the study density-based algorithm have been used.

In the following, preprocessing steps of a CFD analysis presented,

- Creation of the solid model creation and surface meshing with triangular elements are carried out with GAMBIT
- Boundary Layer grid which has prism elements generated with TGrid
- Volume mesh generated with tetrahedral cells using GAMBIT
- Numerical solution setup is done after importing volume mesh into the CFD solver

At the beginning of the study, convergence problems have been experienced, and most of the runs diverged after a certain number of iterations. In a standard CFD run, initialization is done using the free-stream conditions and solution converges after some iterations. However, in side jet case, the gradients in the flow domain are very large. In order to overcome these large gradients, a better initial condition is provided. Around the jet exit three auxiliary volumes are generated, that can be observed in Figure 3.3. Here, the aim is to generate a smooth transition from jet flow to free-stream flow. First, the larger domain which wraps all three volumes and missile body is initialized using the free-stream conditions. Then, the first volume which is closest to jet exit initialized with the flow properties of the jet. Other two volumes are initialized with the flow properties which provide a step by step transition from the jet properties to the free-stream flow properties. With this method a converged solution is obtained.

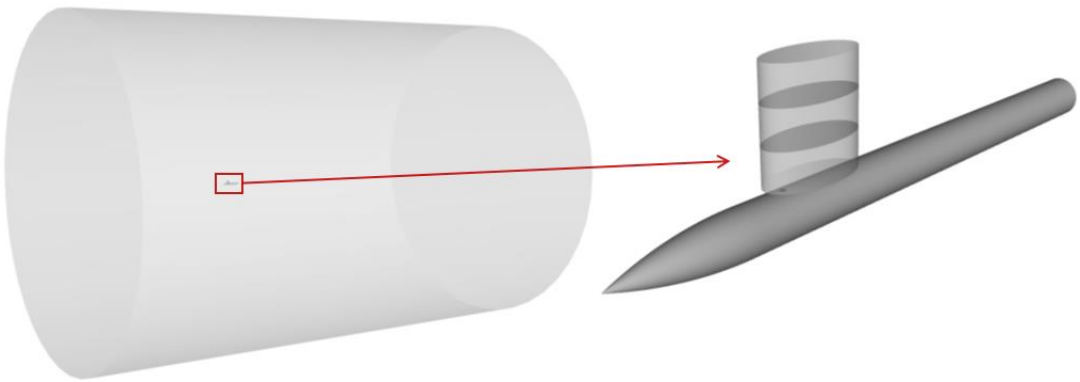

Figure 3.3. Auxiliary Volumes Method

3.4. Force and Moment Amplification Factors

In side jet studies force calculation has a crucial importance since the aim of the system is maneuverability. For force calculation a control volume analysis is carried out on the missile and a scheme of that analysis presented below,

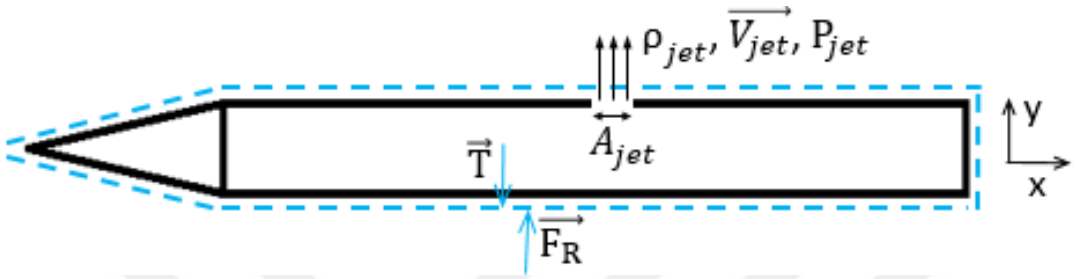

Figure 3.4. Control Volume Analysis Done on the Flow Domain of the Side Jet

$\rho_{jet}, \vec{V}_{jet}, P_{jet}$ represents density, velocity and pressure of the jet flow at exit respectively. A_{jet} is exit duct area and $\vec{T}, \vec{F}_R$ are jet thrust and reaction forces. Blue dashed lines represent the control volume. Assumptions made for control volume analysis are,

- Uniform flow at the jet exit
- Ideal gas
- $\vec{F}_R$ is equal to $\vec{T}$

For the system momentum transfer is inspected and resulted with the following formula,

$$\sum \vec{F} = \sum_{out} \dot{m}\vec{V} - \sum_{in} \dot{m}\vec{V} \tag{3.20}$$

In the above formula, second term of the right-hand side is 0, since there is no inflow or acting external force. Replacing the terms in the above formula,

$$\overrightarrow{F_R} - (P_{jet} - P_{inf})A_{jet} = \dot{m}\vec{V}_{jet} \tag{3.21}$$

$$\vec{T} = \overrightarrow{F_R} = \dot{m}\vec{V}_e + (P_{jet} - P_{inf})A_{jet} \tag{3.22}$$

Replacing $\dot{m} = \rho_e \vec{V}_e A_e$,

$$\vec{T} = \rho_{jet} A_{jet} (\vec{V}_{jet})^2 + (P_{jet} - P_{inf})A_{jet} \tag{3.23}$$

Equation 3.31 is the thrust calculation formula in this study (Gerhart et al., 2015). In the numerical simulation of side jet, numerical solver models an artificial flow for jet plume and calculates the effect of interactions between the free-stream and jet flow. The CFD solution does not contain the thrust effect occurred due to jet flow. Therefore, after obtaining the normal force and pitching moment coefficients from numerical simulation which occurred due to jet and cross-flow interactions, jet thrust calculated from Equation 3.31 should be added and resultant normal and pitching moment coefficients are obtained (Gligorijevic et al., 2013; Kostić, Stefanović, & Kostić, 2017).

Effect of side jet performance should be examined with some factors rather than direct force/moment increments. (DeSpirito, 2015)

$$K_f = \frac{F_{jet} + F_{jet-i}}{F_{jet}} \quad K_m = \frac{M_{jet} + M_{jet-i}}{M_{jet}} \tag{3.24}$$

Where F_{jet} is the jet thrust force, M_{jet} is the jet moment and calculated by $F_{jet} l_{jet}$. l_{jet} is basically the distance between the moment center and jet location. F_{jet-i} is the jet and free-stream flow interaction force and defined by,

$$F_{jet-i} = F_{total} - F_{no-jet} - F_{jet} \tag{3.25}$$

CHAPTER 4

VALIDATION STUDY

In the design process of a side jet, there are many parameters affecting the jet performance. In this study, effect of some of these parameters will be investigated to provide a reference point to future designs. The numerical method (CFD solver, grid size, turbulence models, boundary types, etc.) should be validated before the parametric studies, in order to prove that it is adequate for solving jet and free-stream flow interaction. For validation, experimental studies conducted in wind tunnel facilities will be taken as a reference. The experiment used in this study, provides pressure coefficient distribution on the missile body in the presence of a side jet. When numerically calculated pressure coefficient distribution is close to experimental results it shows that our method resolves the physics of the problem sufficiently. Experimental model is a generic missile geometry and it is presented in Figure 4.1 (Gnemmi, 2008).

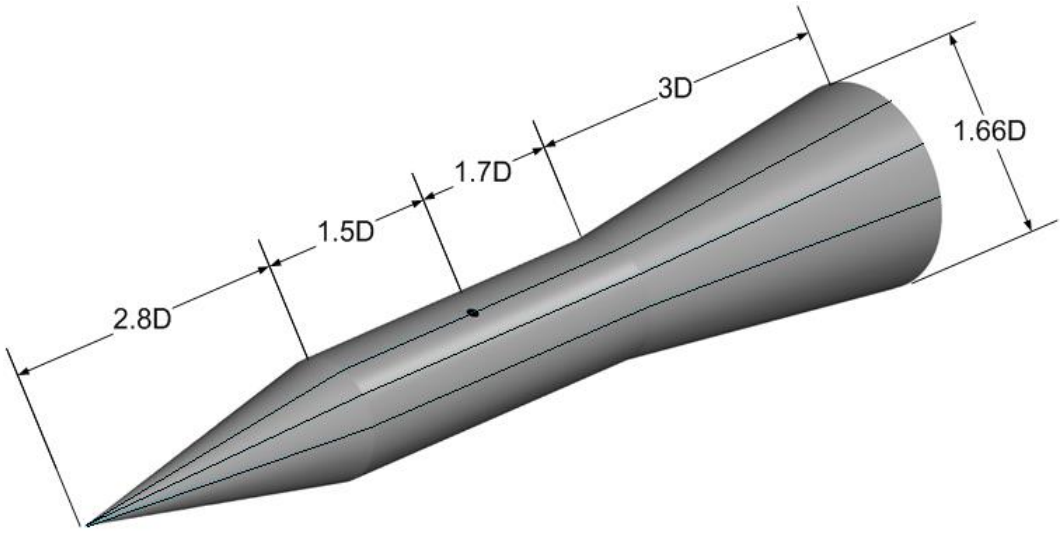

Figure 4.1. Dimensions of the Experimental Model and Pressure Orifices

Generic missile geometry has a diameter of 40 milimeters (*D*) and consists of a cylindrical body with a length of 3.2-*D*, cone shaped nose with a length of 2.8-*D* and a flare after-body with a length of 3-*D* and a base diameter 1.66-*D*. The jet is located at a distance of 4.3-*D* from the missile nose tip at the 180° roll orientation indicating the top part of the missile in the circumferential direction. Also, jet axis and missile axis are perpendicular to each other. On the surface of the experimental model, there exist pressure orifices for pressure measurements beginning at the nose and continuing through the cylindrical body and flare in the longitudinal direction. There are three sets of pressure orifices at roll orientations of 180°, 150° and 120° and they can be observed as black lines in Figure 4.1. Also, the properties of jet and free-stream flows are given in Table 4.1 (Gnemmi, 2008).

Table 4.1. *Boundary Conditions of the Validation Study*

Free-stream Flow	**Jet Flow**
$M = 2.8$	$M = 1$
P_{inf} [Pa] = 20793.2	$PR = 100$
T [K] = 108.96	

For CFD solutions, commercial CFD solver ANSYS Fluent have been used. Far-field and mass inlet boundary conditions are used for the free-stream and jet flows, respectively, to simulate the flow field as in the literature (Ağsarlıoğlu, 2011; Krishnan, Jouhari, & Balu, 2016). For pressure far-field, Fluent requires static pressure, static temperature and Mach number which are given in the Table 4.1. For mass flow inlet, Fluent requires static pressure, total temperature and mass flow rate. In the Table 4.1, PR (pressure ratio) is defined as the strength of the jet and it is calculated by dividing total pressure of the jet flow by the static pressure of the free-stream flow as given before. In the reference, jet flow temperature and the type of the fluid are not clearly emphasized (Gnemmi, 2008). Therefore, the working fluid is assumed as air and its temperature is taken to be equal to the temperature of the free-stream flow. Therefore, static pressure and the total temperature of the jet flow should

be calculated using isentropic relations which are given in the Equations 3.12 and 3.13, since both are required for full definition of mass flow inlet boundary condition. Another input required by the mass flow inlet boundary condition is mass flow rate, which is calculated by the following formula,

$$\dot{m} = \rho V A_{jet} \tag{4.1}$$

The density of the jet flow should be calculated using ideal gas relation, and the velocity of the jet is the speed of sound, formulas for calculating these parameters are given below,

$$P = \rho RT \qquad a^2 = \gamma RT \tag{4.2}$$

4.1. Grid Independency

The flow domain is meshed using unstructured grid which consists of tetrahedral and hexahedral elements by using Gambit and TGrid software packages, both are commercially available by ANSYS. Generated grid is shown in Figure 4.2 and Figure 4.3.

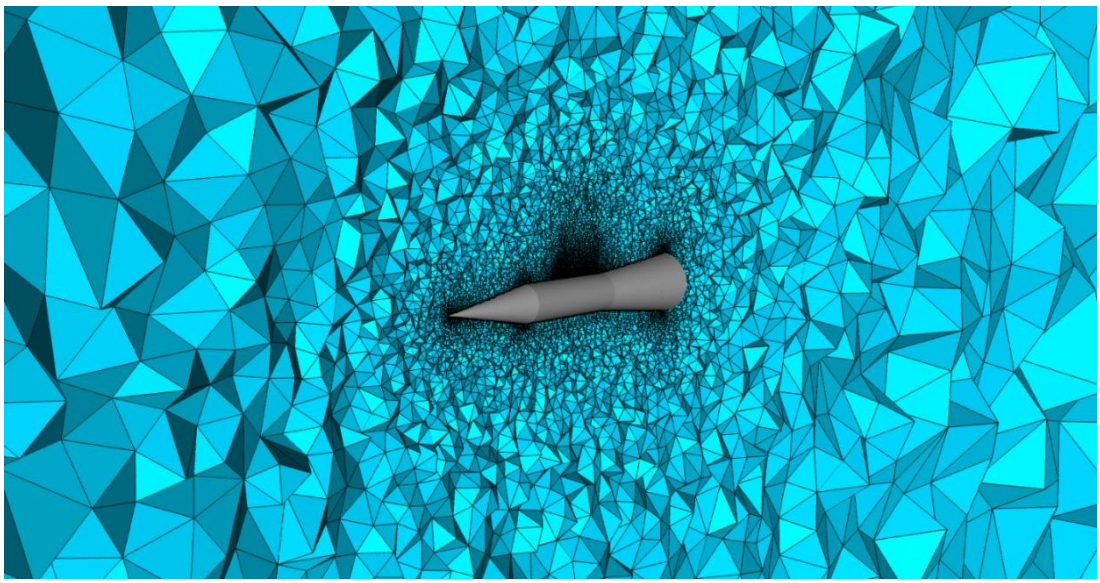

Figure 4.2. Generated Mesh for the Validation Study

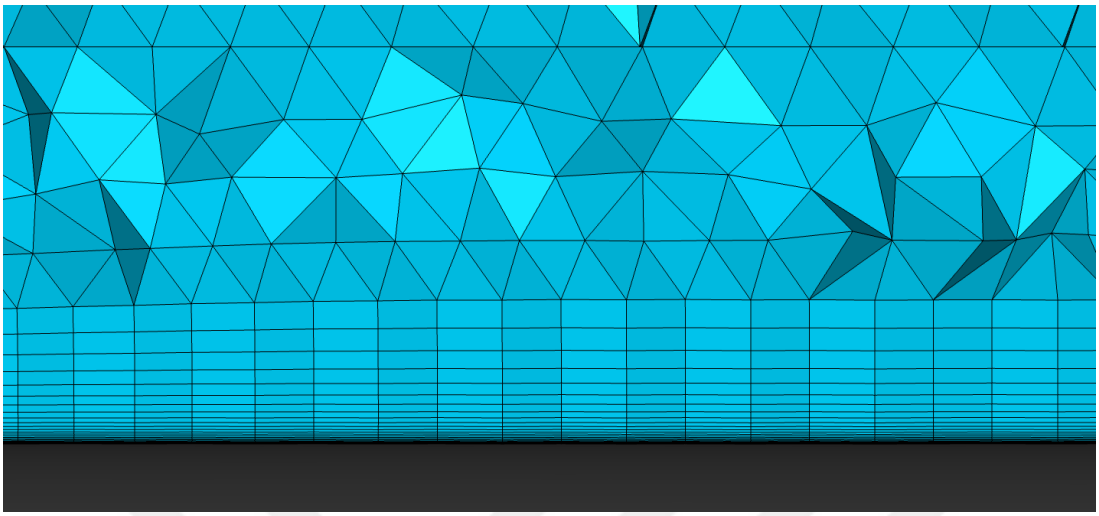

Figure 4.3. Boundary Layer Mesh for the Validation Study

In the meshing process, y^+ value is kept around 1 in order to capture strong gradients in the boundary layer. From the conducted analyses y^+ values are exported from generated meshes and presented in Figure 4.4.

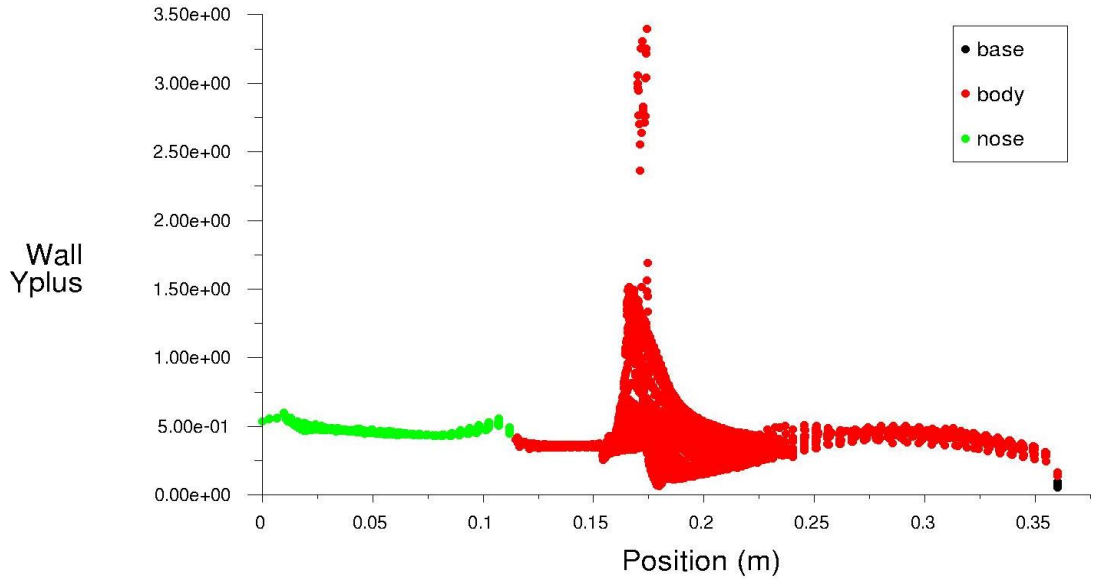

Figure 4.4. y^+ Values of the Generated Mesh

After the examination of Figure 4.4, it is seen that y^+ value is below 1 except for the jet vicinity. Due to separation and recirculation in the jet vicinity y^+ value increases at that region, which is an expected situation and commented that first grid height in the boundary layer adequate for jet in cross-flow case.

For mesh independency study, different mesh sizes have been constructed to be able to check mesh dependency and generated grids are presented in Figure 4.5.

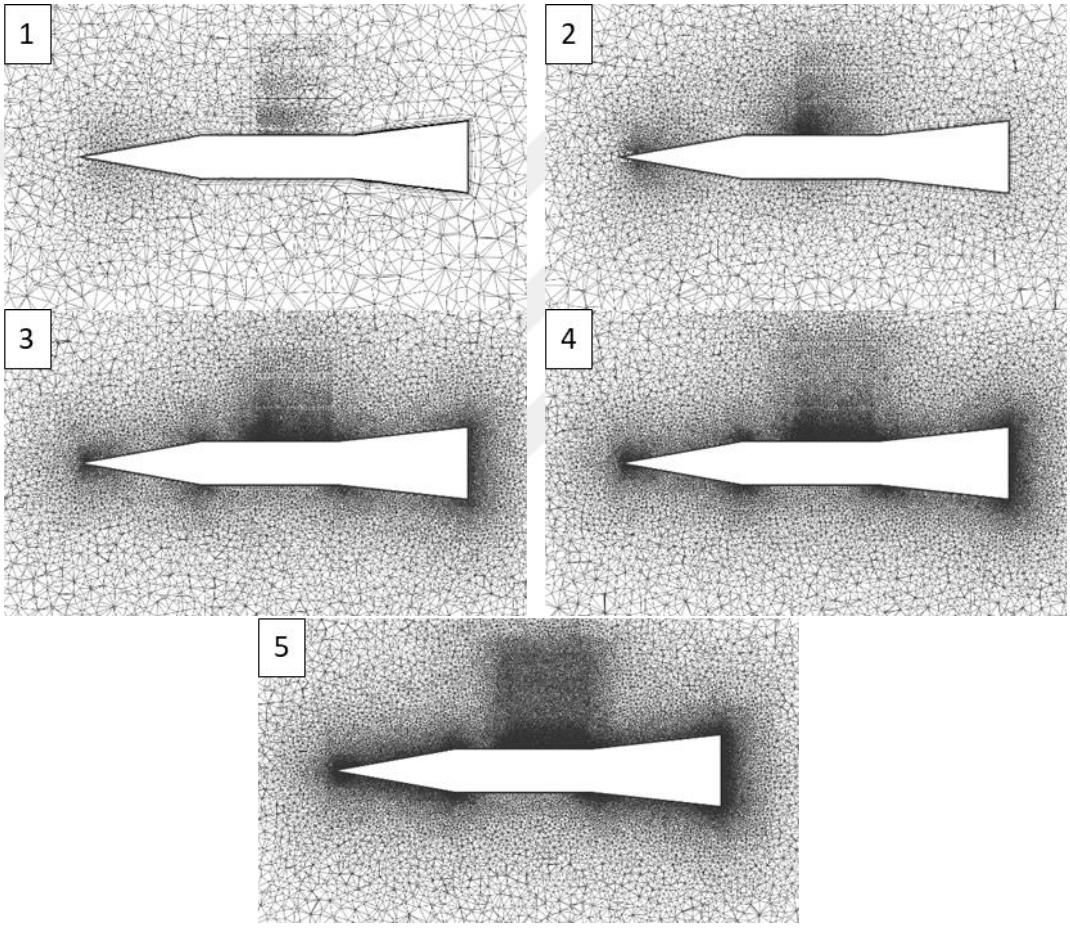

Figure 4.5. Several Grid Qualities

Variation of axial force coefficients for different mesh sizes have been compared with the result of the mesh having the largest number of cells. Results are presented in Figure 4.6 and Table 4.2.

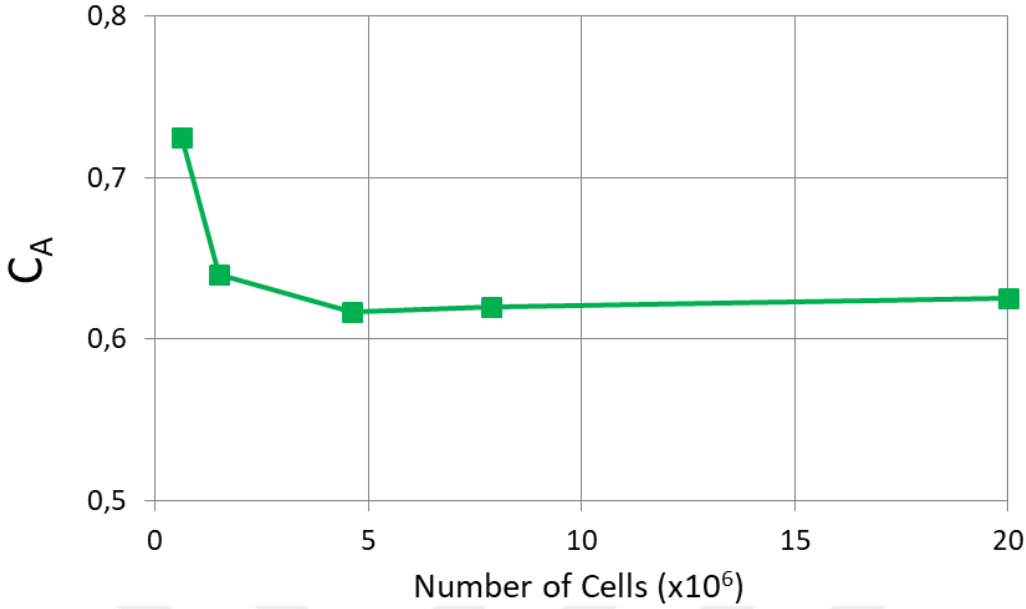

Figure 4.6. Axial Force Coefficients for Several Grid Qualities

Table 4.2. *Results of the Grid Convergence*

Mesh Number	Number of Cells (x10^6)	C_A	ΔC_A (%)
1	0.6	0.72462	15.9
2	1.5	0.64000	2.4
3	4.6	0.61675	-1.3
4	7.9	0.61988	-0.8
5	20.0	0.62496	

From Figure 4.6, results of different mesh qualities can be observed. In Table 4.2 which is the tabulated version of Figure 4.6, change of axial force coefficients for several grid qualities are calculated with respect to result of the fine grid which has around 20 million cells. From Table 4.2, one can observe that result of the third grid is satisfactory since the difference from the result of finest grid falls below 1.5%. Mesh number 3 has almost 4.6 million cells and this quality is used for the remaining parts of the study.

4.2. Turbulence Models

At this point, different turbulence models have been employed for solving the flow domain. Using the same grid, different CFD runs have been completed using *k-ε* realizable and *k-ω* SST models. Both models use two equations for turbulence modeling. Pressure coefficient results at 180° roll orientation which means a line crossing the missile surface in longitudinal direction which is also crossing the jet from the center of it are presented in Figure 4.7 together with experimental data. In the comparison of different turbulence models, the same grid has been used. In the meshing process, *y+* value has been kept around 1 except for the vicinity of the jet, in order to resolve boundary layer accurately.

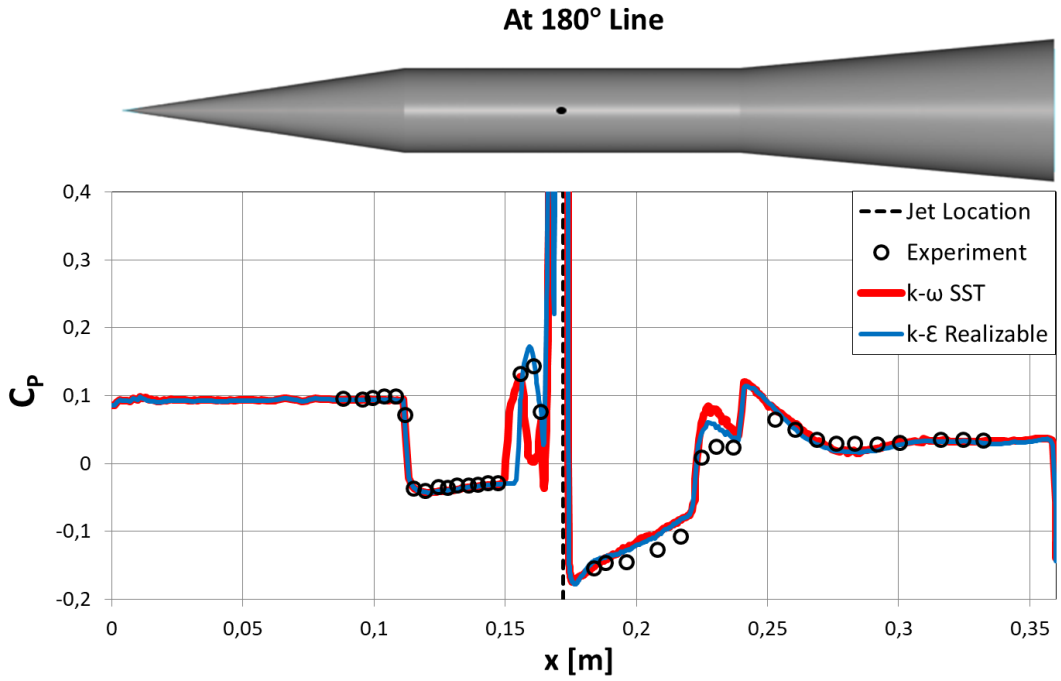

Figure 4.7. Comparison of the k-ε Realizable and *k-ω* SST Turbulence Models

From Figure 4.7, one can say that *k-ε* realizable turbulence model calculates the pressure distribution more accurate than *k-ω* SST turbulence model. The *k-ω* SST turbulence model predicts separation early while the *k-ε* realizable model is accurate

in the separation region which can be observed around 0.16 m along *x*-axis at Figure 4.7. This feature of the *k*-ω SST model is also mentioned in the Turbulence Models notes (ANSYS Inc., 2006). Moreover, both turbulence models overshoot the pressure values at the reattachment region. In the consideration of the recent comparisons between two models, it is concluded that, use of *k*-ε realizable model is appropriate in this study for turbulence modeling.

4.3. Results

In this section, numerical and postprocess results of Fluent which is a commercial CFD software, are given and examined in detail. In Figure 4.8, Figure 4.9 and Figure 4.10, pressure coefficient results are given together with experimental results for 180°, 150° and 120° roll angles for the medium fine grid which has 4.6 million cells.

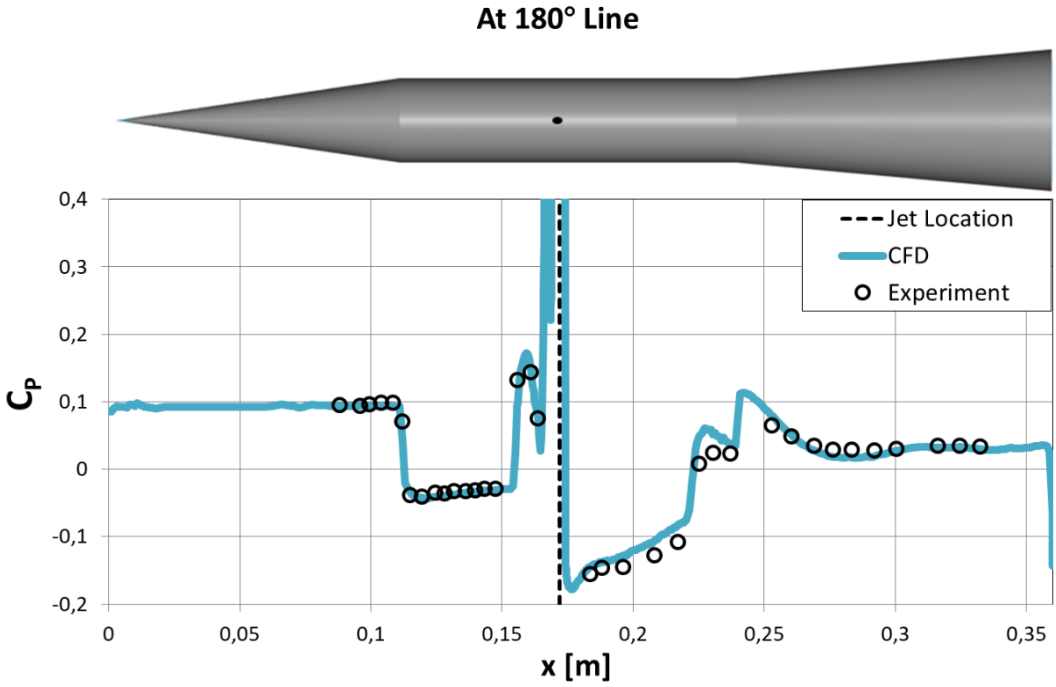

Figure 4.8. Pressure Coefficient Distribution at ϕ=180°

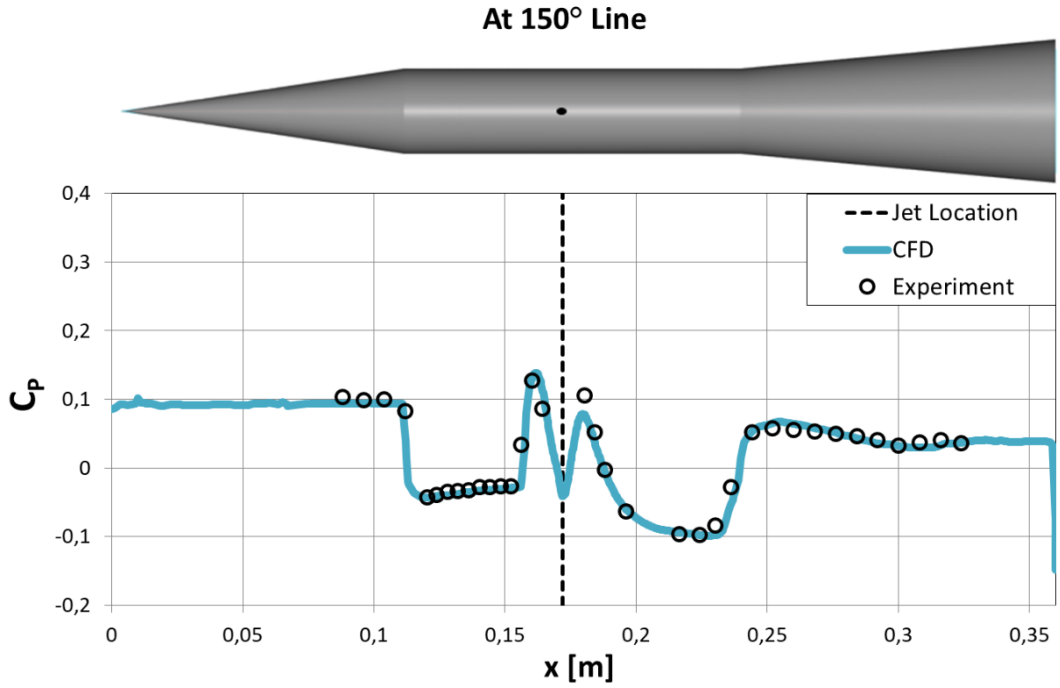

Figure 4.9. Pressure Coefficient Distribution at ϕ=150°

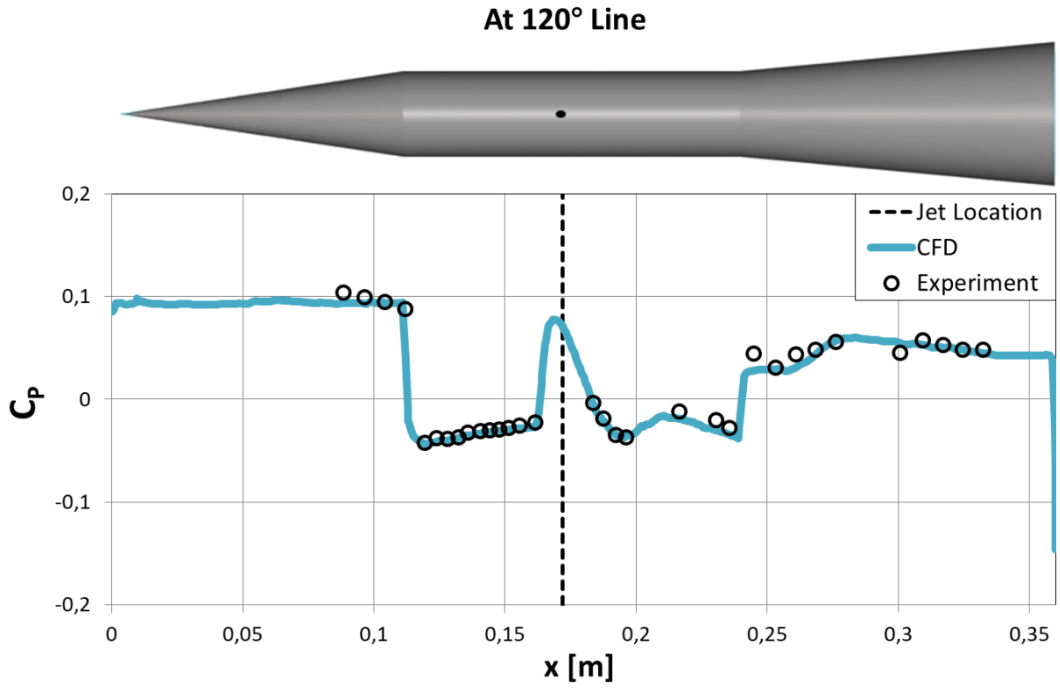

Figure 4.10. Pressure Coefficient Distribution at ϕ=120°

CFD results shows a good agreement with experimental data except for small inconsistencies. At x < 0.15 m, where jet does not expect to affect the pressure distribution, experimental and CFD data are almost identical for the three roll angles. At 0.15 m < x < 0.17 m where sudden pressure rise occurs due to jet flow, the variation of the pressure coefficient in the experiment and CFD shows a good agreement with each other for 180° and 150° roll angles. At 0.17 m < x < 0.22 m which is the wake region due to jet flow, experimental and CFD pressure distributions show similar behavior. For 0.22 m < x < 0.24 m, there are little differences between results especially for 180° roll angle where reattachment shock occurs. In general, CFD solves flow and finds pressure coefficient distribution correctly with respect to experimental results except for some differences. After making numerical comparison between experiment and CFD, contours are obtained for observing the flow in detail which are presented in Figure 4.11, Figure 4.12 and Figure 4.13.

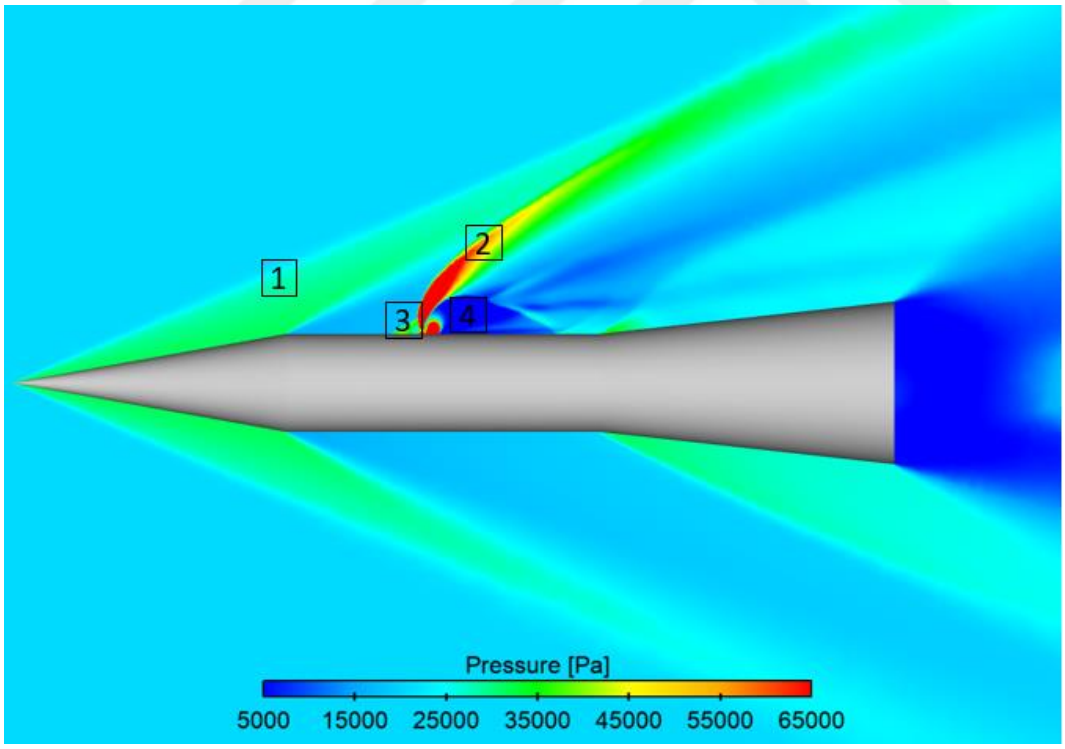

Figure 4.11. Pressure Contours at the Symmetry Plane

For the examination of the flow domain pressure and Mach contours are used and an extra fine grid having approximately 20 million cells have been generated in order to obtain more detailed contours. Pressure distribution around the model is given in Figure 4.11. In the figure, nose shock which occurs due to interaction of nose of the experimental model with the free-stream flow indicated as 1, jet bow shock which occurs due to interaction of jet and free-stream flows signed indicated by 2 and separation due to sudden pressure rise due to jet indicated by 3 and wake region which occurs after jet indicated by 4 can be observed clearly from pressure contours.

In Figure 4.12, the pressure distribution on the surface of experimental model is given. Local pressure rise due to jet flow can be observed before the jet location having a bow like shape on the surface. Also, behind the jet, the wake region is visible from the surface pressure contours.

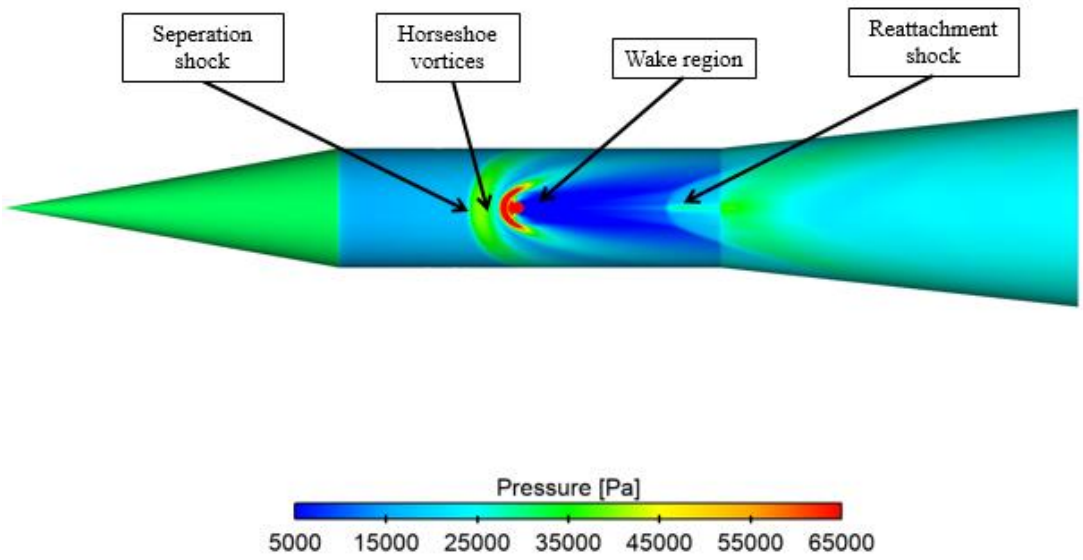

Figure 4.12. Surface Pressure Distribution on the Missile Body

In Figure 4.13, the Mach number distribution, obtained from our CFD analysis, is presented, while a photograph of an another side jet experiment which is taken by the Schlieren Image Technique (Bernhard Stahl, Emunds, & Gülhan, 2009) is given in

Figure 4.14, however, the name of one of the shocks in the figure is changed as ‘Reflected shock’ in order to keep consistency in the text. The aim is to observe flow phenomena around side jet and determine whether CFD models the flow accurately or not. It can be observed from Figure 4.13 and Figure 4.14, experimental and numerical results show a very good agreement with each other. Therefore, it can be concluded that CFD solves flow domain very well. Separation region which is visible in both figures are caused by the high adverse jet pressure. Jet bow shock can be easily noticed in the flow domain since the flow is at Mach 2.8 before the shock which is the free-stream Mach number. At the downstream of the jet bow shock, flow velocity drops drastically, which is, in general, a characteristic behavior of shocks. Jet plume becomes ‘an obstacle’ to the free-stream flow and a jet bow shock occurs. Barrel shock occurs due to under-expansion of high-pressure jet plume and this region terminates with the formation of the Mach disk.

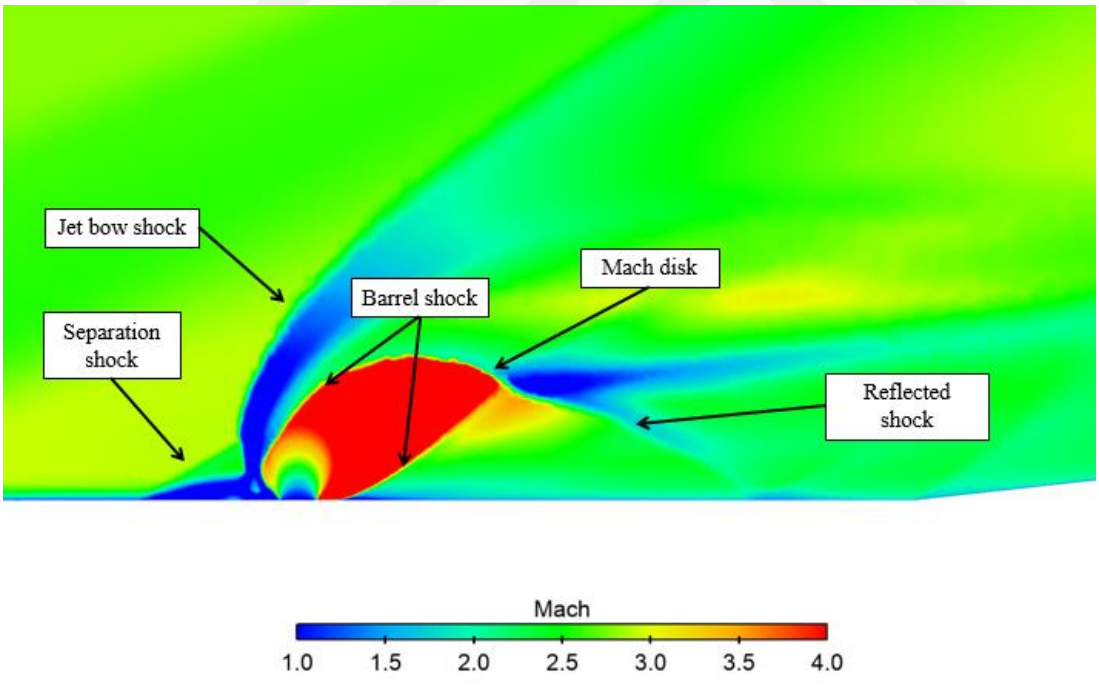

Figure 4.13. Mach Number Contours at the Symmetry Plane

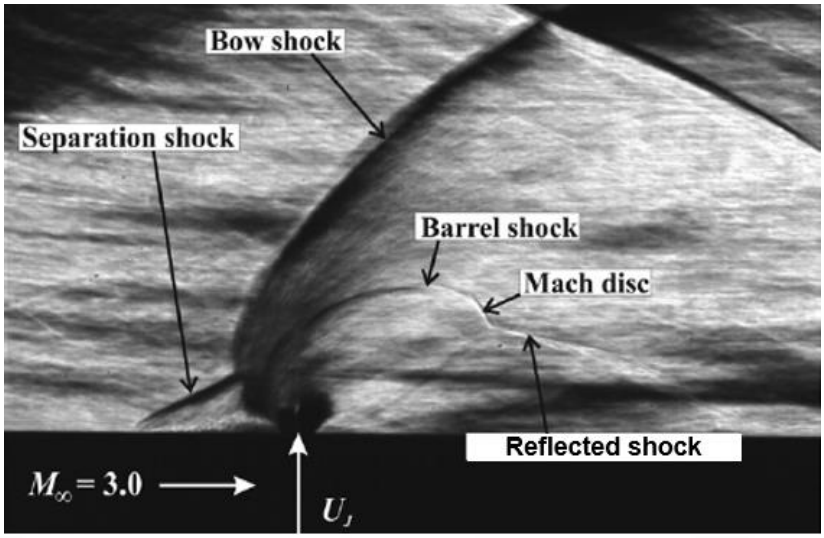

Figure 4.14. Schlieren Image of the Jet Domain

So far in this section, we did some numerical and visual comparisons between the CFD and experimental results and concluded that CFD provides a similar solution to the experimental results. Moreover, for the following parts of the study validated mesh density, boundary condition definition, initial condition provision are used.

CHAPTER 5

PARAMETRIC STUDIES

After validating the numerical solution method, several parameters affecting the flow characteristics and jet performance are examined. A generic missile model is selected from literature. In the parametric study of Min, Lee, & Byun, (2006), a similar missile body have been used. A similar geometry have been chosen for parametric studies which is shown in Figure 5.1 including the dimensions. Tangent ogive nose is used with an ogive radius of 9.25-*D* as in the Min et al.'s study, however length of the missile changed to 15-*D*. Two cases have been considered mainly in the study, jet is mounted on the front and aft of the missile which are both 5-*D* away from the center of gravity of the missile in order to obtain comparable results. Diameter of the missile is 50 mm's and jet diameter selected as 0.14-*D* which is a consistent value with the cases presented in the Min et al.'s and the validation case. Also, the side thruster is being used in the cruise phase of the flight where high maneuverability is an asset in order to hit the target. In the cruise phase main engine is not operating, hence the main engine plume has no influence on the side thruster performance. Additionally, a spouting angle definition is employed which is measured from the downstream of the jet for both jet location cases.

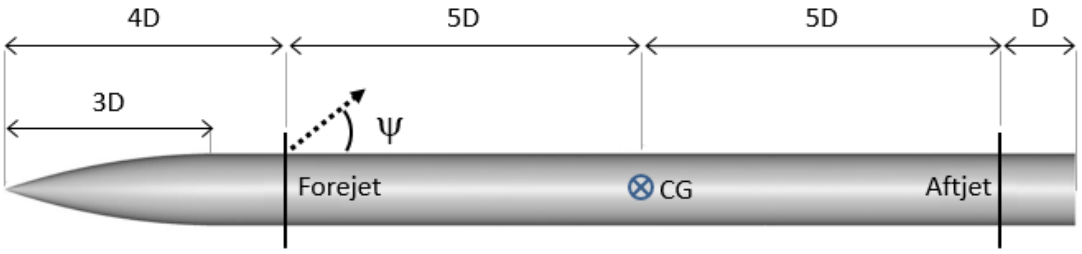

Figure 5.1. Slender Missile Geometry

The geometry presented in Figure 5.1 meshed in a similar manner as in the validation study. Effect of body incidence angle and jet are examined in the aspect of resultant forces and moments. In order to clarify the combined effect of body incidence angle and jet thrust, a phrase is used as explained in Figure 5.2 and Figure 5.3.

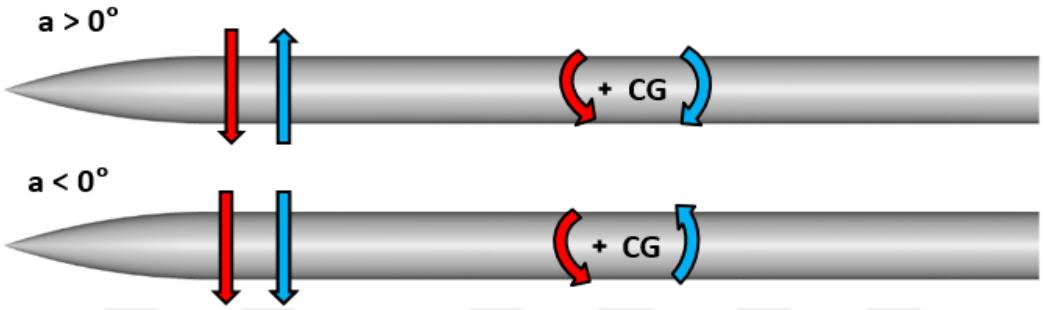

Figure 5.2. Forces and Moments for the Forejet

First, for a jet off case, which is a slender missile geometry in the study, it is seen that center of pressure is ahead of center of gravity for all ranges of examined Mach numbers. In this case, missile is statically unstable when the jet is not operating; however, stability is out of scope of the study. As explained in the aim part, rather than a final missile design, it is aimed to inspect lateral thruster behavior under several flight and jet conditions. Additionally, a supplementary control mechanism might be mounted on the missile such as a thrust vector control mechanism as in THAAD missile, therefore unstableness issue which occurs when the jet is not operating can be resolved. (P. Champigny, 1994)

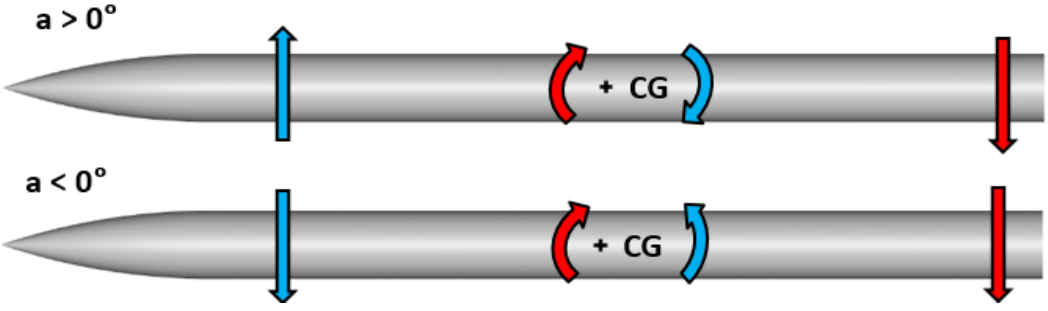

Figure 5.3. Forces and Moments for the Aftjet

While the jet is operating, and body is not aligned with the free-stream direction, the moment calculation can be complicated, therefore Figure 5.2 and Figure 5.3, are presented to make clear explanations. In these figures, blue arrows show the forces and moments caused by the free-stream flow which occurs due to angle of attack of the missile body, and red lines shows the forces and moments caused by the jet thrust. When the resultant of normal forces are considered; at positive angles of attack, free-stream flow and jet have opposite contributions, and for negative angle of attack, they both have the same sense.

Next, resultant pitching moments are explained which is the focus of this study due to the reasons explained in the 'Literature Survey' section. Figure 5.2 shows the forejet case, for both negative and positive incidence angles. For positive incidence angles, the contribution of the jet and free-stream flows to the resultant moment are in opposite directions. However for negative incidence angles, their effects are in the same direction. The aftjet case is shown in Figure 5.3. For positive incidence angles and aftjet case, free-stream flow and jet create moments in the same direction. However, at the same jet location for negative incidence angles, the generated moments act in opposite directions. In this study, effects that occur due to aerodynamics will be named as body force/moment and effects that occurs due to jet flow will be named as jet in the following. Therefore, 'Jet - Body' phrase will be used for positive incidence and forejet location, also negative incidence and aftjet location. And 'Jet + Body' phrase will be used for the negative incidence and forejet location, also positive incidence and aftjet location. For moment inspections, 'Jet – Body' and 'Jet + Body' cases will be compared individually for two distinct jet locations.

Next, the operating altitude of the missile has been selected as 10.4 km, hence, free stream pressure and temperature is found as 25 kPa and 220.7 K using the standard atmospheric table (Anderson, 2017). Furthermore, it is assumed that the jet exit temperature is equal to the free-stream temperature in order to exclude the effect of heat transfer. Missile velocity and jet flow velocity at the jet exit have a Mach number of 2, as an initial design point. And jet strength is decided as 200 which is the $P_{jet,0}/P_{inf}$,

hence, $P_{jet,0}$ is 5 MPa and P_{jet} is approximately 639 kPa . Using Equation 4.1 mass flow rate is found as 0.2312 kg/s. So far, flow conditions have been defined as an initial design point and it is summarized in the following sub-section.

In order to characterize the inspected flows Reynolds number is calculated. In the parametric studies, free-stream flow is inspected in the Mach range from 1.5 to 4.5, which point out a Re_L between $9e^6$ and $27e^6$. Also, Reynolds number of the jet flow is calculated and found as $Re_D=2.8e^6$. Calculated Reynolds numbers show that, both flows are in study is turbulent.

5.1. Effect of the Jet Spouting Angle

First, the coupled effects of jet spouting angle, free-stream Mach number and body incidence are examined, and flow conditions for inspected variables are presented in Table 5.1.

Table 5.1. *Inspection of the Jet Spouting Angle*

Flow Conditions	
Location	Forejet, Aftjet
M_{inf}	1.5, 2, 3, 4
α(°)	-5, 0, 5
ψ (°)	between 67.5°, 112.5°

Jet performance are affected considerably when it interacts with the free-stream flow. As explained so far, high pressure occurs at the upstream of the jet, while low pressure occurs at the downstream of the jet. High pressure region increases the jet performance, while low pressure region decreases it. Hence, spouting angle may increase jet performance at some critical degree. On the contrary, deflecting the jet will decrease the normal jet thrust, hence pitching moment. Therefore, the jet is deflected at relatively small angles which is 22.5° at maximum. In this section of the study, 120 runs have been performed and the symbols used in the resultant plots are presented in Figure 5.4. Obtained results at zero incidence angle for both jet locations are presented in the following figures.

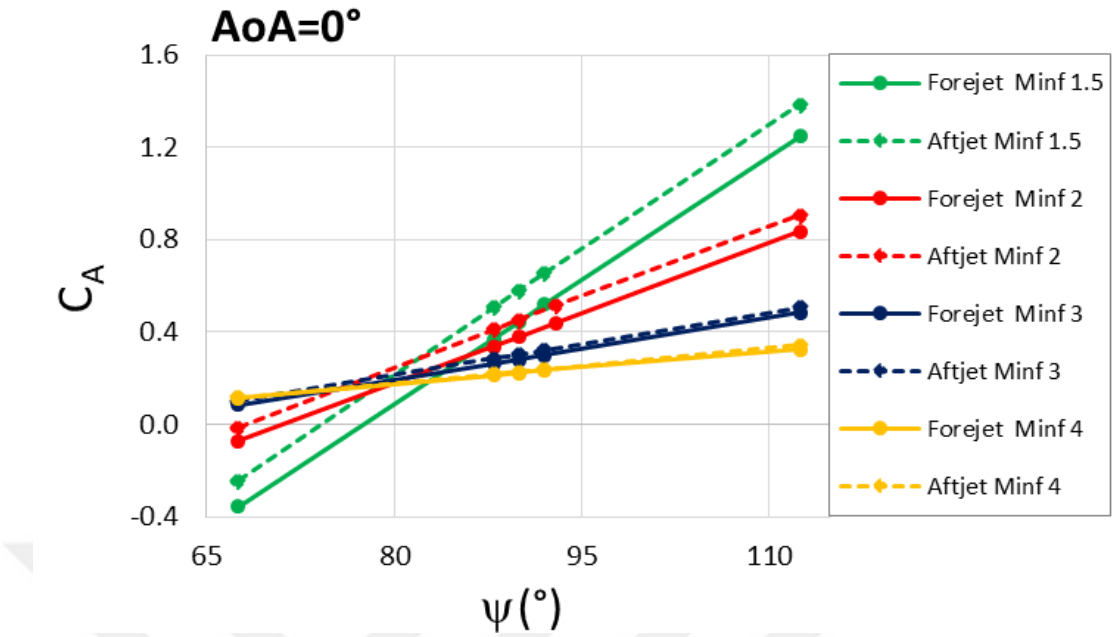

Figure 5.4. Change of C_A with the Spouting Angle at Zero Incidence

The effect of the spouting angle is examined by considering the axial force coefficient, and results are presented in Figure 5.4. For this case, the jet is injecting gases to the free-stream in normal direction and the axial force coefficient decreases with the increasing Mach number which is a characteristic behavior of the bodies flying at supersonic speeds. When jet is deflected towards upstream, C_A increases, and if jet is deflected towards downstream C_A decreases as expected. This feature of the jet can be used for increasing the missile range. Also, slope of the axial force coefficient decreases with increasing Mach number, however, jet thrust in the axial direction will remain same for constant spouting angle and different free-stream flow velocities, and it is expected to interaction forces have a minor effect in the axial direction. Therefore, change in the axial force coefficient slope is due to the change in the dynamic pressure. Additionally, when jet is located at the aft of the missile, axial force coefficient is larger than the missile with the forejet. Increase in the axial force coefficient may be related to the base drag, however detailed examinations should be made using contours obtained from particular flow conditions and those are presented in the following parts of the study.

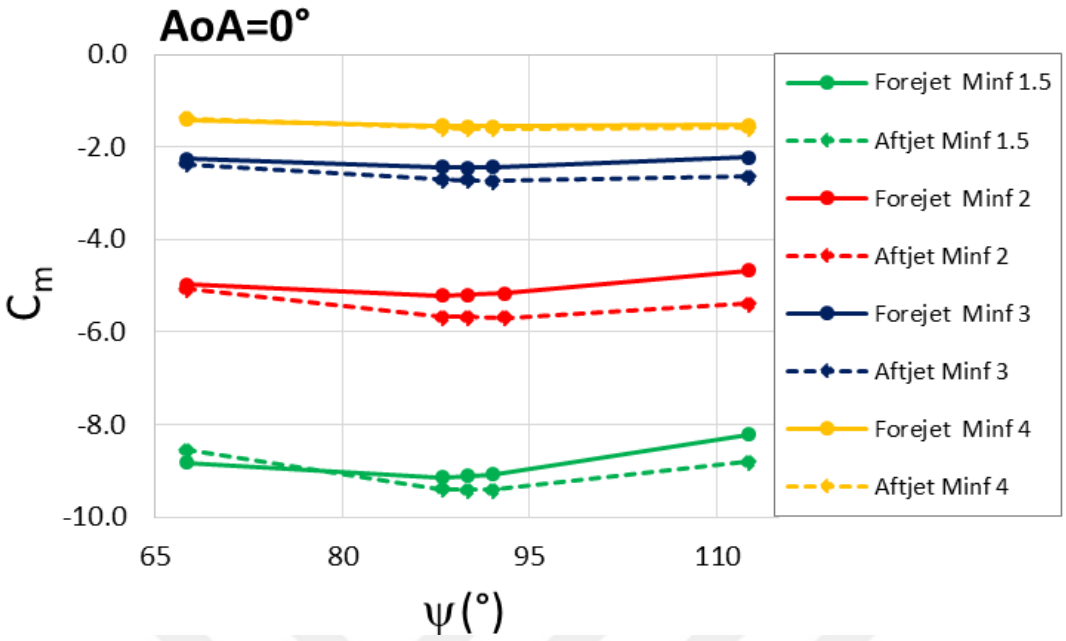

Figure 5.5. Change of C_m with the Spouting Angle at Zero Incidence

The effect of spouting angle is also examined by considering the results of the pitching moment coefficient, which is the focus of the study since it shows the maneuverability of the missile. As shown in Figure 2.1 before, negative values of the pitching moment coefficient show the pitch up movement. Hence, in the original results, forejet creates negative pitching coefficients and aftjet creates positive pitching moments. In the graphs, pitching moment coefficients of the aftjet are multiplied with -1, in order to obtain comparable graphs for the two locations of jet.

For the aftjet case, a larger axial force acts on the missile than the forejet case which can be observed from Figure 5.4. Also, as seen from Figure 5.5, for 90° spouting angle and for all examined Mach numbers, more pitching moment occurs when the jet is on the aft-location. These two results are examined with pressure contours and pressure coefficient distributions which are presented in Figure 5.6, Figure 5.7 and Figure 5.8 and those are obtained from numerical simulations of the free-stream flow at a Mach number 2, normal jet spouting angle, zero incidence angle and the jet flow at a Mach number 2.

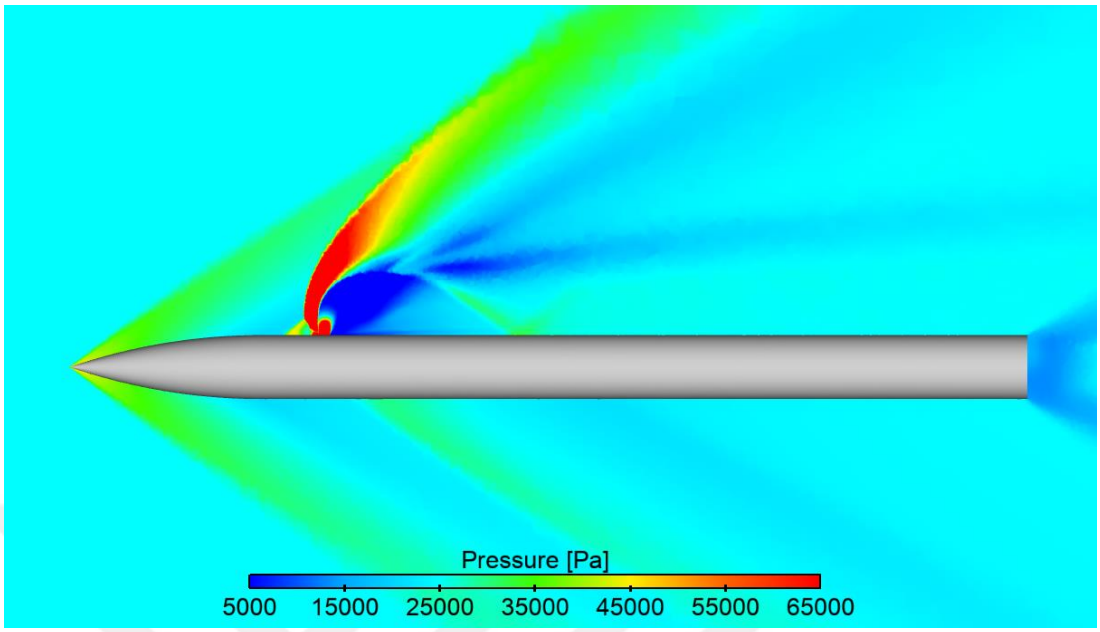

Figure 5.6. Pressure Contours for the Forejet and M_{jet}=2, ψ=90° and M_{inf}=2

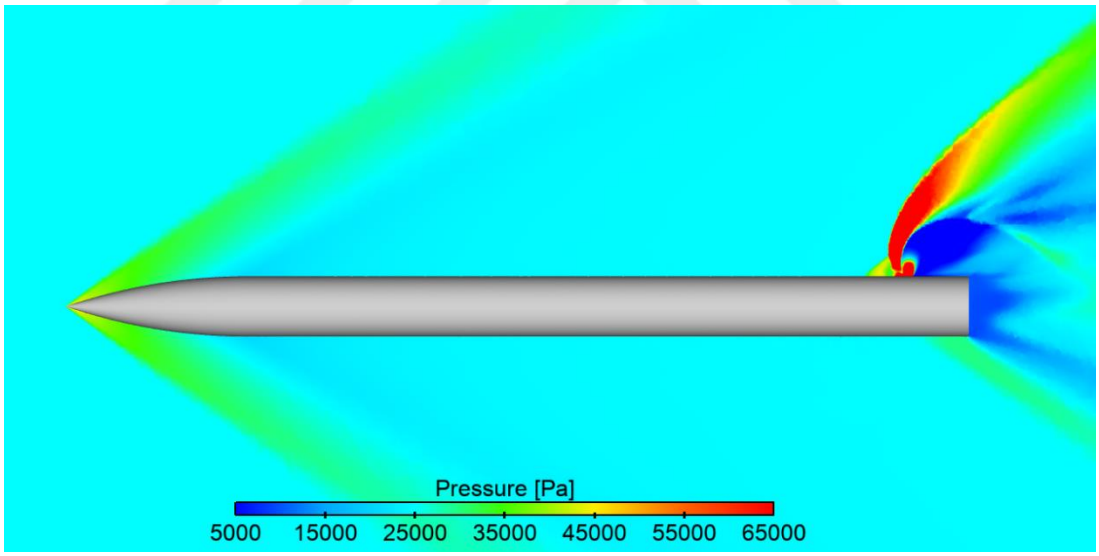

Figure 5.7. Pressure Contours for the Aftjet and M_{jet}=2, ψ=90° and M_{inf}=2

First comparison is made for axial force coefficient which is related to missile velocity or range. For the aftjet location, jet plume obstruction moves closer to the base in comparison when it is at the forejet location, hence, lower pressure values can be

observed at the base of the missile, which leads to an increase in axial force coefficient around 19 percent for free-stream flow at a Mach number 2. When pressure and skin friction drag are examined, it is concluded that the pressure drag increases for the aftjet case with respect to the forejet case, while skin friction drag changes negligibly as can be observed from the pressure contours.

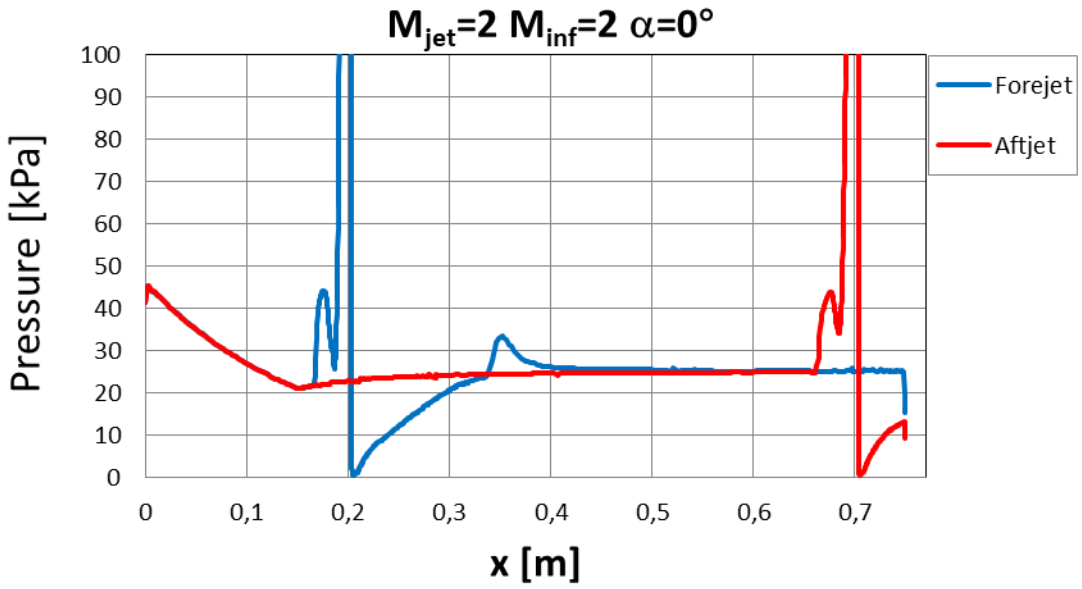

Figure 5.8. Pressure Coefficient Distribution at 180° Line for M_{jet}=2 and M_{inf}=2

Also, pressure contours and pressure coefficient distributions are examined to interpret the pitching moment results. As explained before, at the upstream of the jet exit high pressure region occurs and this region increases the pitching moment and, therefore jet performance. Also at the downstream of the jet, low pressure develops, which is at the wake of jet plume as can be observed in Figure 5.6, Figure 5.7 and Figure 5.8. This low-pressure region leads to a local lift generation which explains why the wake of the jet decreases the jet performance.

For normal spouting angle, free-stream flow at a Mach number 2, zero incidence angle and the forejet case, length of the low-pressure region in axial direction is around 2.68-D. For the same flow conditions and the aftjet case, low-pressure region is 0.93-D in length. Due to shift of low-pressure region towards outside of the missile, pitching moment coefficient of the aftjet location increases around 9,2% with respect to forejet location for free-stream flow at a Mach number 2 and zero incidence angle case.

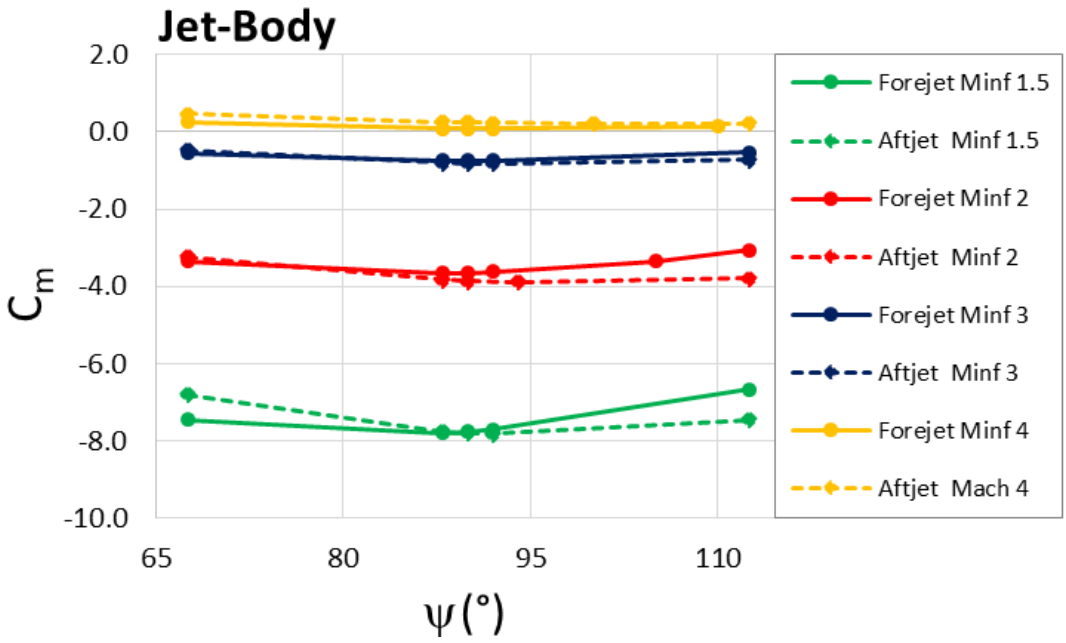

Figure 5.9. Change of C_m with the Spouting Angle for the 'Jet – Body' Case

Next, spouting angle is inspected together with incidence angle for the same range of the free-stream flow velocity. In the examination of incidence angle together with jet spouting angle effect, the case for 'Jet - Body' is inspected, where the body at non-zero incidence angle and the jet creating moments in reverse direction. The results are presented in Figure 5.9. The case for 'Jet + Body' where both creates moment in the same direction is presented in Figure 5.10.

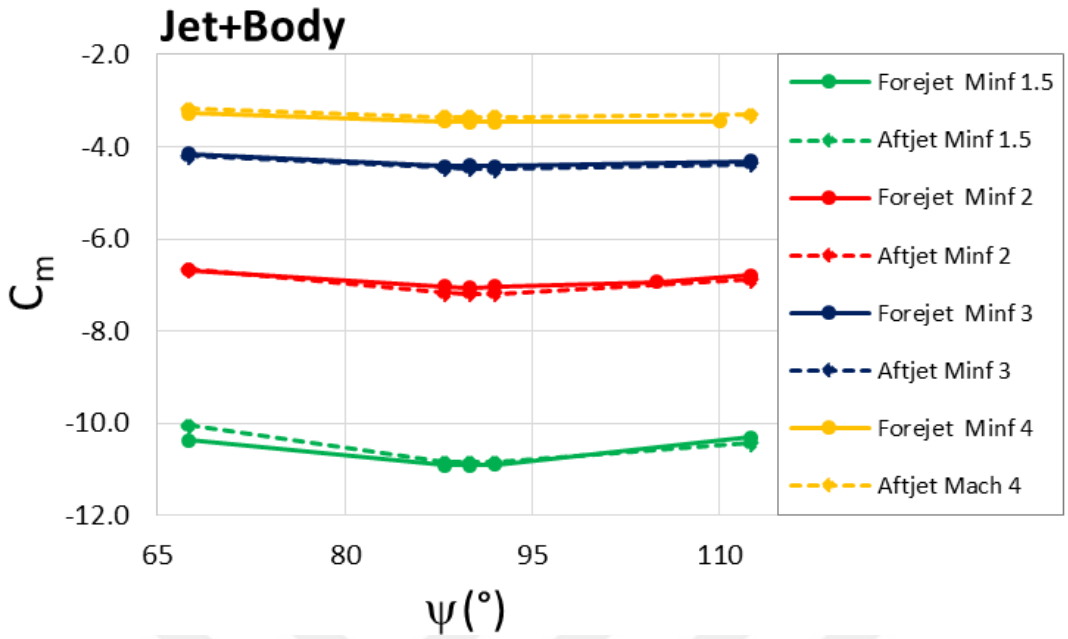

Figure 5.10. Change of C_m with the Spouting Angle for the 'Jet + Body' Case

One property of the results should be pointed out. Moments are not symmetrical with respect to ψ=90° line. This asymmetry occurs due to axial component of jet thrust when the jet is deflected away from normal spouting angle. In general, with increasing Mach number, resultant moment coefficients decrease due to increase in dynamic pressure, as in the case of axial force coefficient. One can also conclude that the resultant pitching moment decreases for 'Jet - Body' case and increases for 'Jet + Body' case with respect to the 'Zero Incidence Angle' case, as expected.

When Figure 5.4, Figure 5.5, Figure 5.9, and Figure 5.10 are examined, one can see that there are some missing results which is due to the convergence problems. At some flow conditions, numerical simulations are not converged or even diverged, therefore it is decided to give a close point when convergence cannot be achieved. For example, in Figure 5.10, for the forejet location and a free-stream Mach number 4, convergence cannot be obtained for a spouting angle of 112.5°. Hence an additional numerical simulation is conducted for a spouting angle of 110° which is close to the missing point and presented in the graphs.

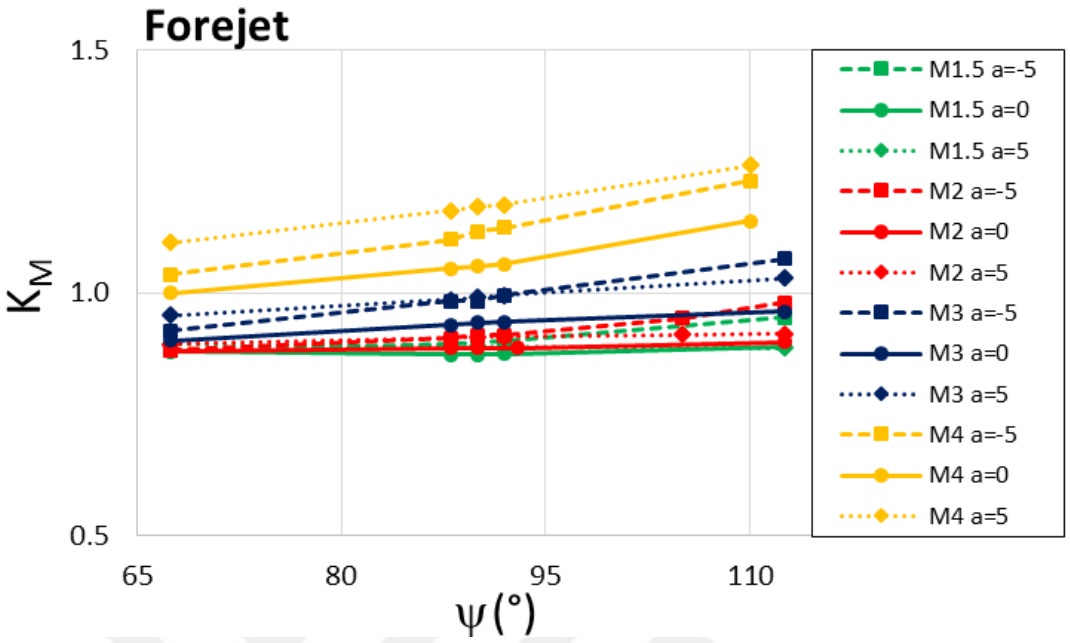

Figure 5.11. K_m Graphs for the Forejet Location at Several Mach and Incidence Angles

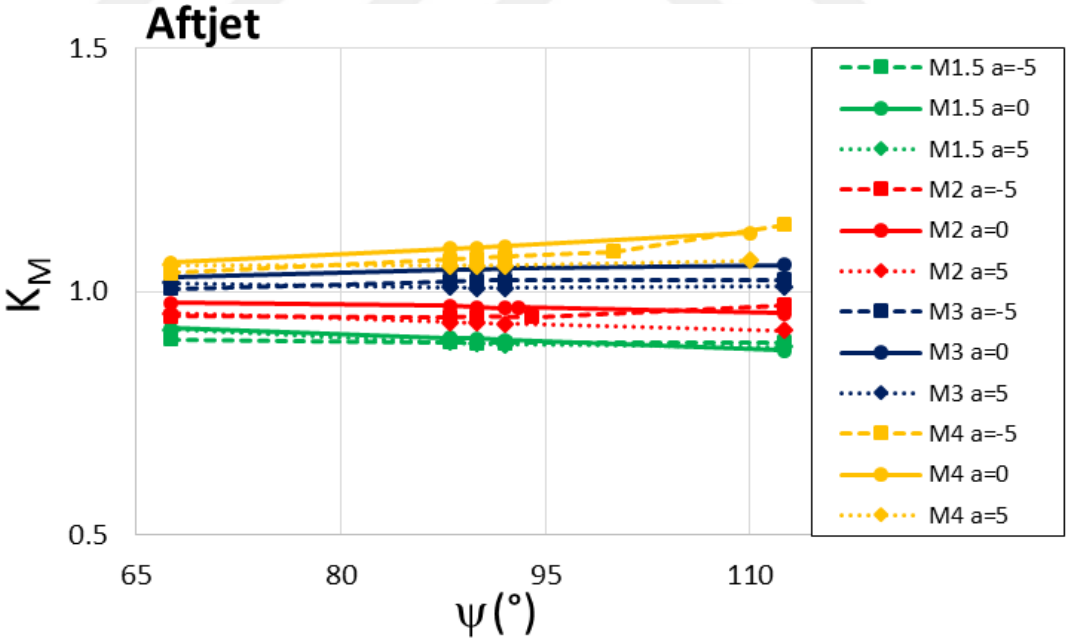

Figure 5.12. K_m Graphs for the Aftjet Location at Several Mach and Incidence Angles

Furthermore, effect of spouting angle is inspected for different free-stream Mach numbers with moment amplification factors, which shows the effect of jet and free-stream flow interactions numerically and results are presented in Figure 5.11 and Figure 5.12. One can conclude that, changing spouting angle can improve jet and free-stream flow interactions.

So far in this section, spouting angle effect is examined for different free-stream Mach numbers, angles of attack and two distinct jet locations. At the beginning of the study, jet spouting angle is expected to be critical for the jet performance. Hence, a better jet performance than normal jet spouting, might be obtained by changing spouting angle. However, from Figure 5.5, Figure 5.9 and Figure 5.10, one can see that, when the jet is deflected away from 90° moment decreases which is different than what is expected. For a deeper analysis, moment amplification factors are calculated and plotted in Figure 5.11 and Figure 5.12, to understand whether the jet and free-stream flow interactions increase the jet performance or not. From the figures, one can see that when the jet is deflected from the normal spouting angle, K_m increases generally. This can be noticed from higher free-stream velocities quite easily. Therefore, it is concluded that deflecting jet flow may result in interactions to support jet performance. Though, pitching moment coefficients show that maximum maneuver capability is obtained when the jet is spouting normally. As a conclusion, the jet spouting angle may positively affect the interaction forces, but it decreases the jet thrust and the total maneuverability of missile decreases. So, normal component of the jet thrust is dominant for different spouting angles in the aspect of maneuverability of the missile.

It has been decided to use a normal jet spouting in this section, so far. Next, the effect of free-stream flow velocity is inspected for both locations of jet which are spouting fluid in normal direction.

5.2. Effect of the Free-stream Flow Velocity

In this part of the study, effect of free-stream flow velocity is examined together with incidence angle, for a missile operating at 10,4 km, while the jet is injecting gas at a mass flow rate of 0.2312 kg/s and an exit pressure of 639 kPa, as before.

Table 5.2. *Inspection of the Free-stream Flow Velocity*

Flow Conditions	
Location	Forejet, Aftjet
M_{inf}	1.5, 2, 3, 3.5, 4, 4.5
α(°)	-5, 0, 5
ψ (°)	90

Free-stream flow velocity is inspected for two different jet locations, incidence angles of -5°, 0°, 5° and normal jet spouting angle. In this part, result of 36 runs are presented. Normal force and pitching moment results of these runs are plotted in Figure 5.13 and Figure 5.15. In these figures, solid lines represent the forejet location and dashed lines represent the aftjet location. Other details of the graphs are presented in the legends of the figures.

First, results are examined in the aspect of normal force using the coefficients and amplification factors in Figure 5.13 and Figure 5.14.

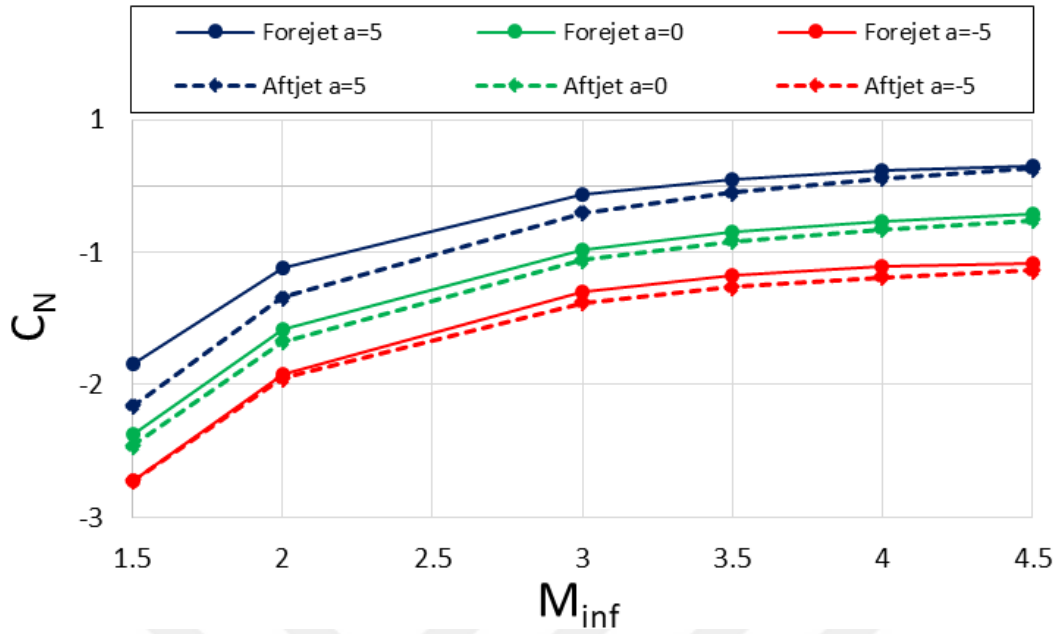

Figure 5.13. C_N Results at Several Free-stream Velocities and Incidence Angles

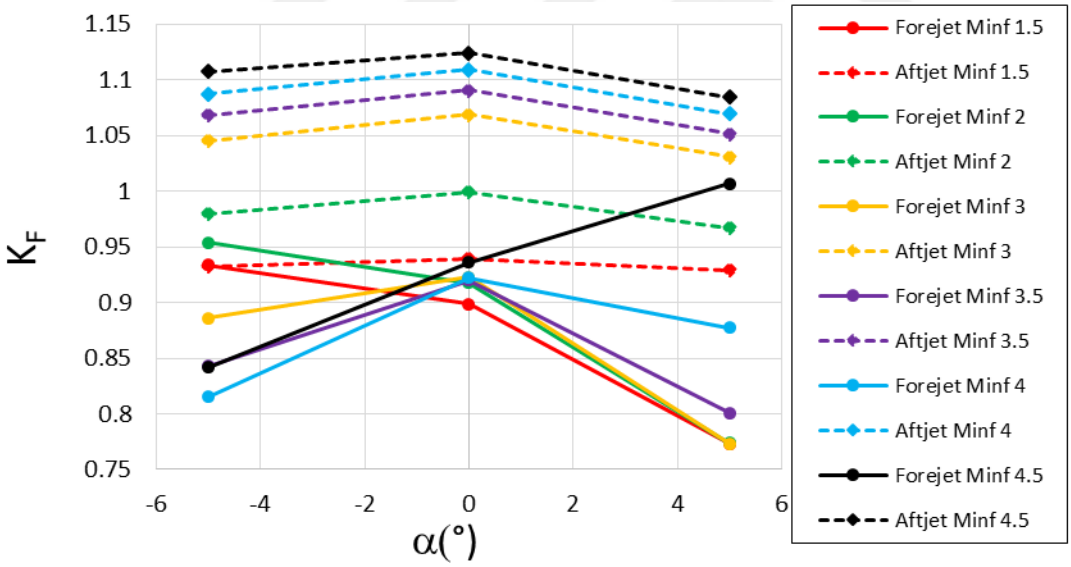

Figure 5.14. K_F Values at Several Free-stream Velocities and Incidence Angles

One can say that, larger normal forces and force amplification factors are obtained when the jet is located at the aft-location which is closer to the base of the missile from Figure 5.13 and Figure 5.14, which is due to low-pressure region shifting towards

outside of the missile as explained so far. For the forejet location, K_F trends change considerably while trend of the aftjet location results are consistent with each other for different free-stream velocities. It is concluded that the effect of the nose shock and reattachment shock have effect on the performance is more significant at the forejet than the aftjet. Effect of shocks on jet performance for the two jet locations will be shown with pressure contours in the following parts of this section. Pitching moment results of two jet locations at different free-stream flow velocities and incidence angles are plotted in Figure 5.15.

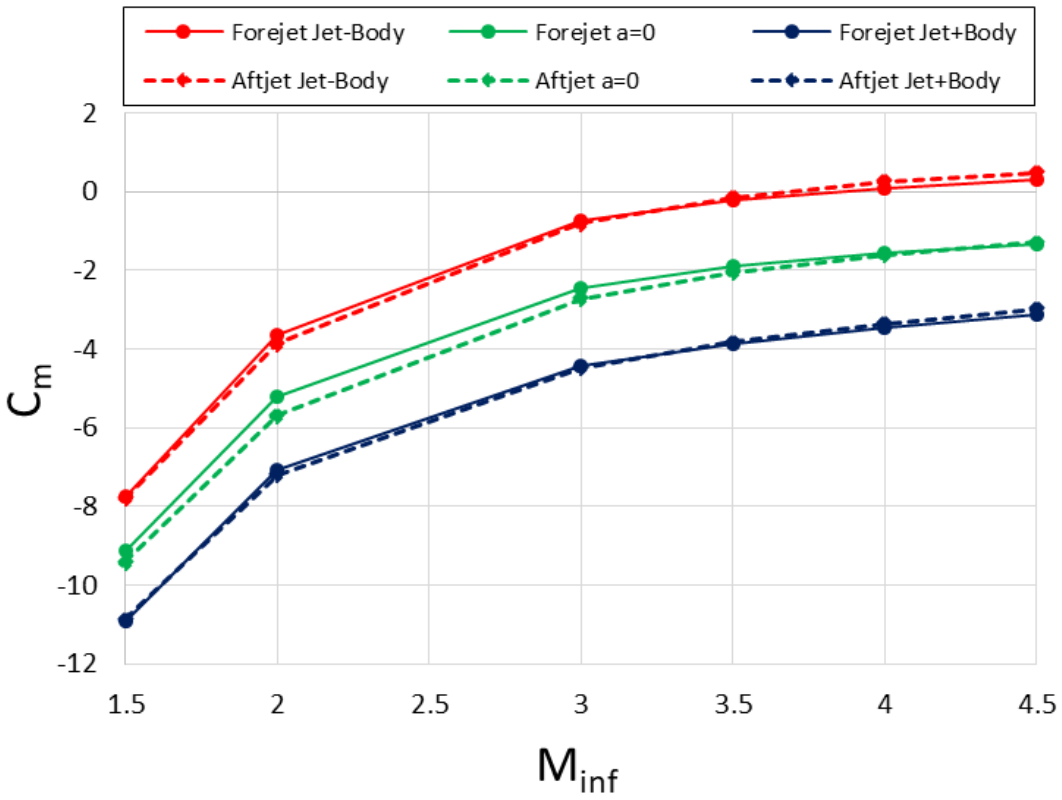

Figure 5.15. C_m Results at Several Free-stream Velocities and Incidence Angles

In the 'Jet - Body' case, if free-stream velocity increases to a point where the Mach number is greater than 3.5, moment due to the free-stream flow dominates the jet moment. The same tendency can be observed from the difference between the two

cases ‘Jet + Body’ and ‘Jet - Body’. Moment difference between two cases increases from low free-stream velocity to high, which shows the change of the body moment due to free-stream velocity.

Additionally, two locations of the jet cannot be compared clearly using Figure 5.15. In order to make a comparison between two jet locations, moment amplification factors are calculated and compared with each other in Figure 5.16, Figure 5.17 and Figure 5.18 and several comments are made from these graphs.

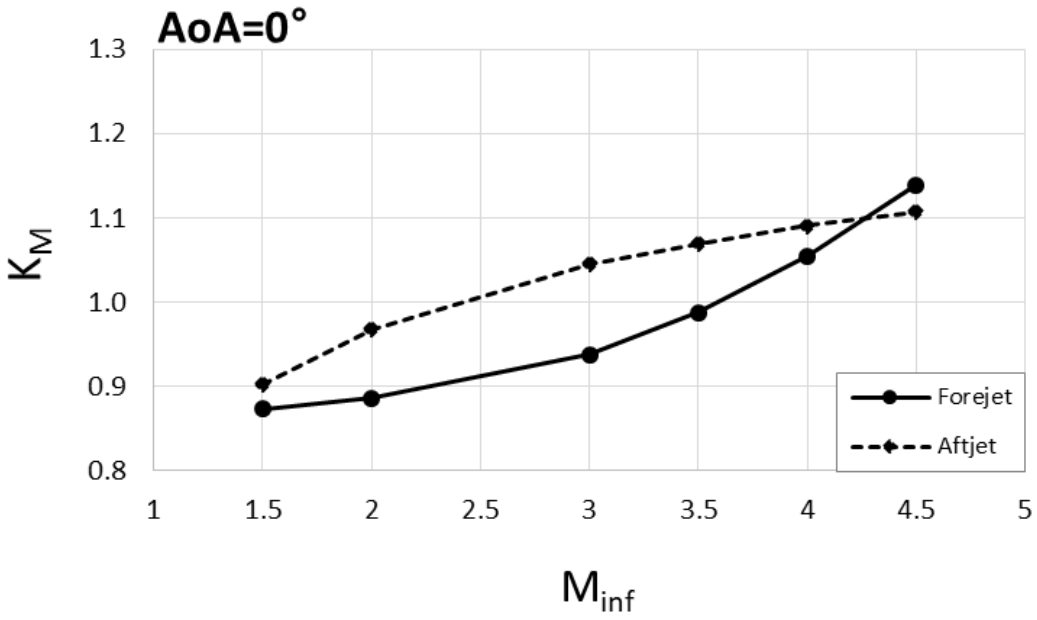

Figure 5.16. K_m Values for Several Free-stream Velocities and Zero Incidence Angle

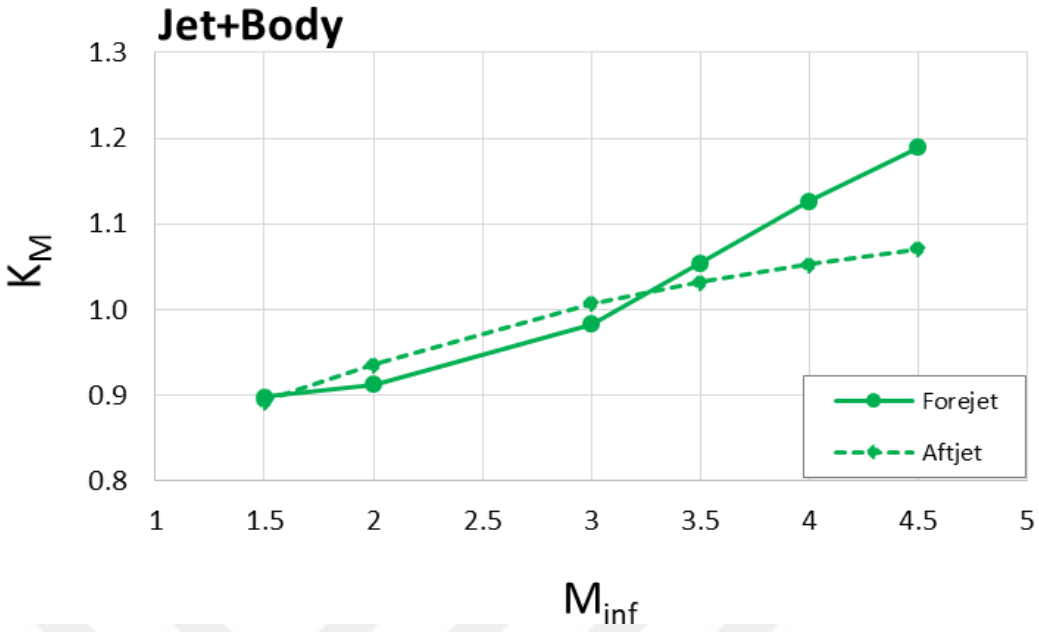

Figure 5.17. K_m Values for Several Free-stream Velocities and 'Jet + Body' Case

Moment amplification graphs are plotted on individual graphs for the cases of zero incidence angle, 'Jet + Body' and 'Jet - Body' for neatness, otherwise graphs may not be seen clearly. From these graphs, for both locations of the jet and three different body incidence angles, jet performance increases with increasing free-stream flow velocity which is due to interactions of the jet and free-stream flow. For higher free-stream flow velocities separation shock becomes stronger since flow shows more resistance to the separation at higher free-stream velocities (Hamed & Kumar, 1994). Stronger separation shocks can be observed by comparing Figure 5.6, Figure 5.7, Figure 5.19 and Figure 5.20. Additionally, for all examined incidence angles, the aftjet shows better performance at relatively low free-stream flow velocities which is explained by shifting low-pressure region that occurs at the downstream of the jet, towards the outside of the missile. This phenomenon is proved with the contours and pressure distributions presented in Figure 5.6, Figure 5.7 and Figure 5.8 which are the results of free-stream flow having a Mach number of 2 for two different jet locations.

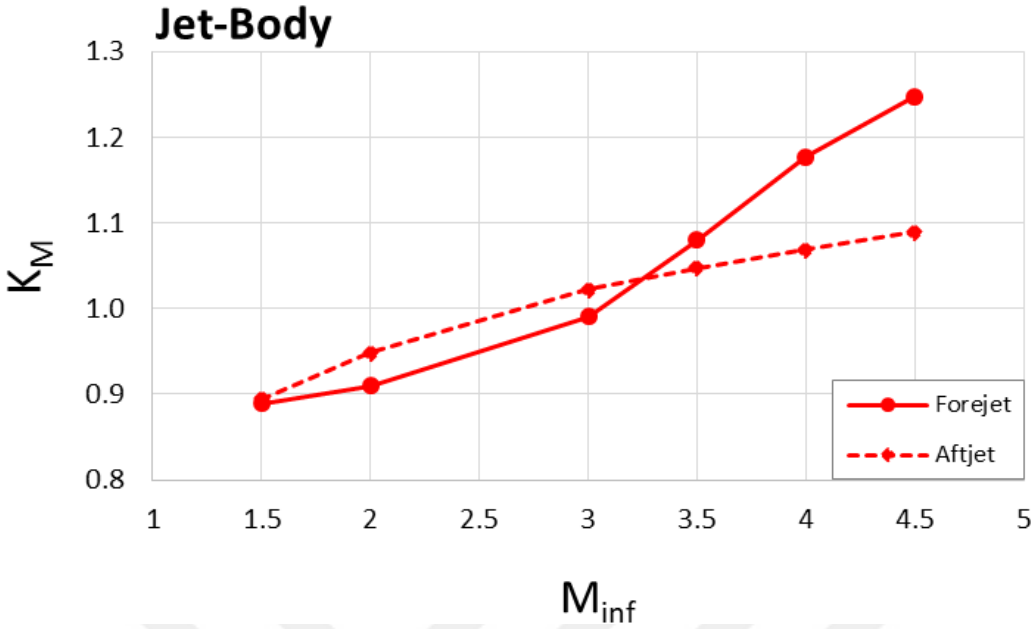

Figure 5.18. K_m Values for Several Free-stream Velocities and 'Jet - Body' Case

At higher free-stream flow velocities, the forejet location shows better performance for the inspected incidence angles. At higher free-stream flow velocities, the jet plume becomes smaller, so as the recirculation region. Hence, the advantage of aftjet location diminishes at the higher flow velocities which is observed from the pressure contours and distributions of the two jet locations that operate at a free-stream Mach number of 4.5, as presented in Figure 5.19, Figure 5.20 and Figure 5.21. From Figure 5.21 which is the result of free-stream flow velocity of Mach 4.5 and zero incidence angle, forejet causes a low-pressure region that has a length of 1.26-D in axial direction. And aftjet at same flow conditions has a low-pressure region 0.93-D in length. That observation proves that the shift of the low-pressure region has a minor effect on the jet performance for relatively higher free-stream flow velocities.

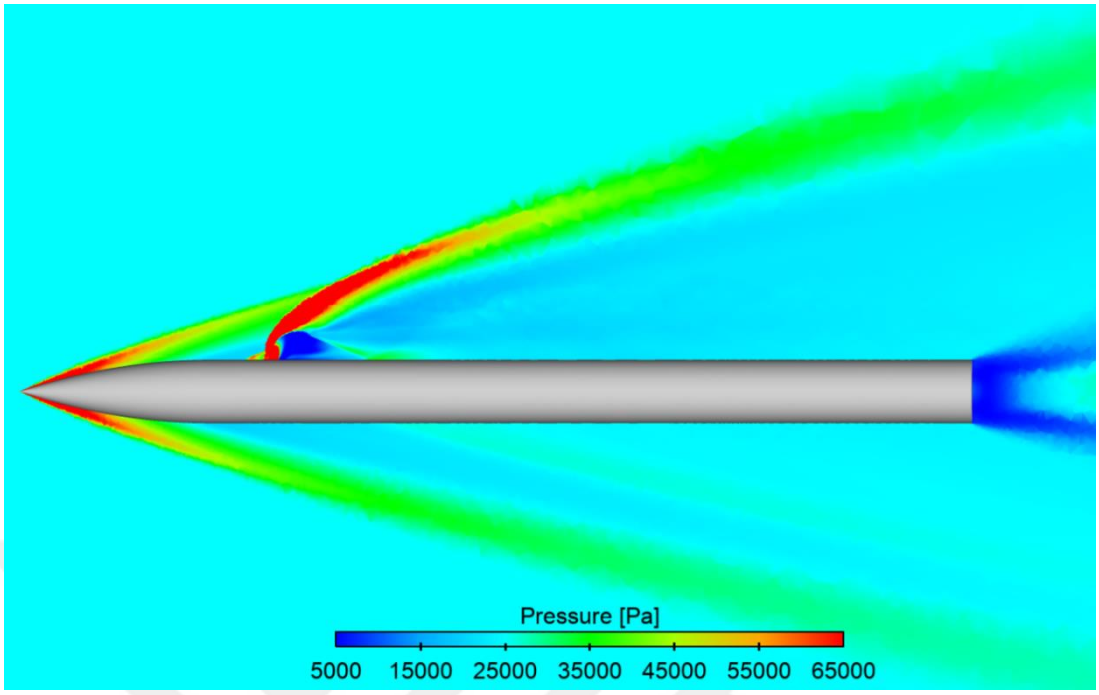

Figure 5.19. Pressure Contours for the Forejet Operating at M_{jet}=2 and M_{inf}=4.5

Higher performance of the forejet location of the jet is examined in the aspect of the back pressure and reattachment shock. First, reattachment shock is inspected, and it is observed that the reattachment shock occurs at the downstream of the forejet and increases the jet performance as can be seen from Figure 5.19 and Figure 5.21 around x=0.28 m. Additionally, at the aftjet location, the reattachment shock does not occur on the missile body, therefore it has no effect on the jet performance. Observed reattachment shock at the downstream of the forejet, increases pitching moment coefficient of forejet around 2.8% with respect to the one of the aftjet.

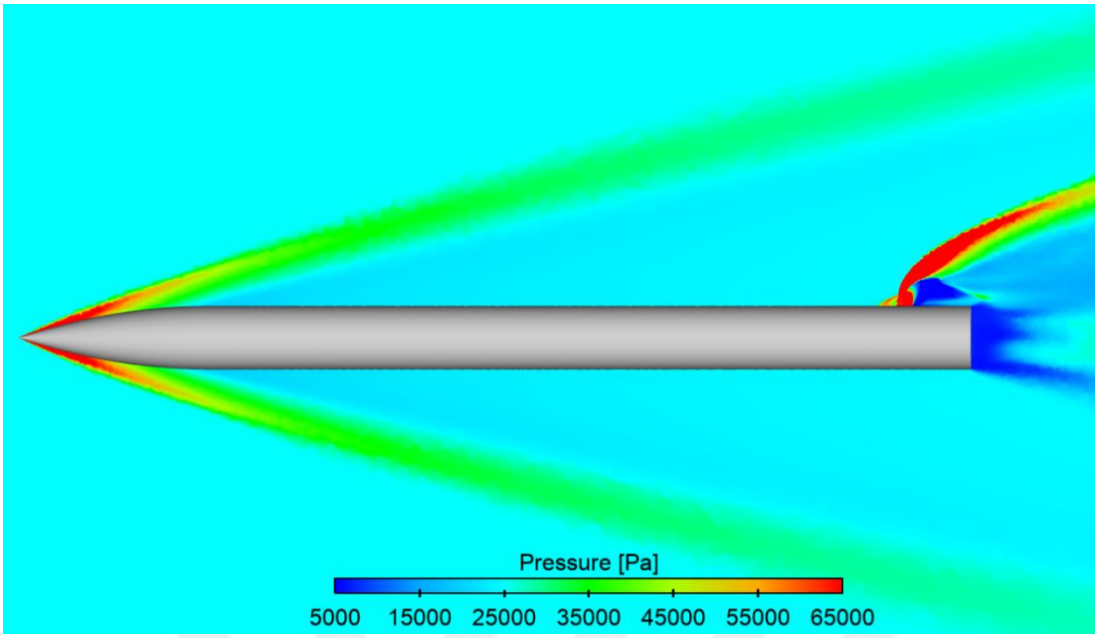

Figure 5.20. Pressure Contours for the Aftjet Operating at M_{jet}=2 and M_{inf}=4.5

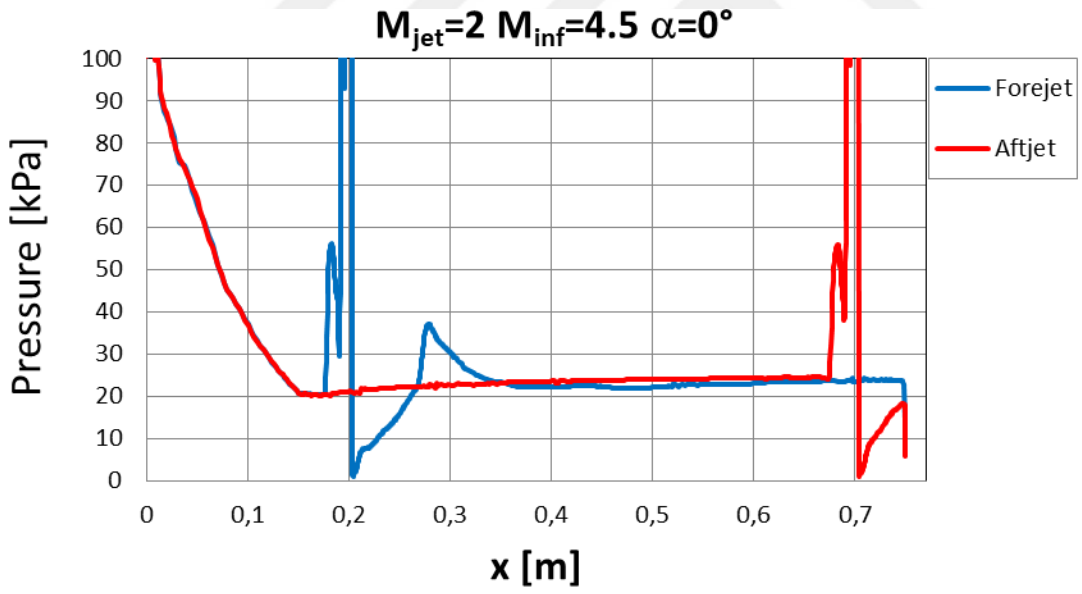

Figure 5.21. Pressure Coefficient Distribution at 180° Line for M_{jet}=2 and M_{inf}=4.5

Next, the effect of back pressure is examined using Figure 5.22 and Figure 5.23 which are the pressure contours of free-stream Mach numbers of 2 and 4.5 for jet-off

condition. In these figures, a rectangle is plotted over the pressure distribution for representation of the jet locations. Two short edges of the rectangle indicate the fore- and aftjet locations while the line between them indicates the center of gravity of the missile.

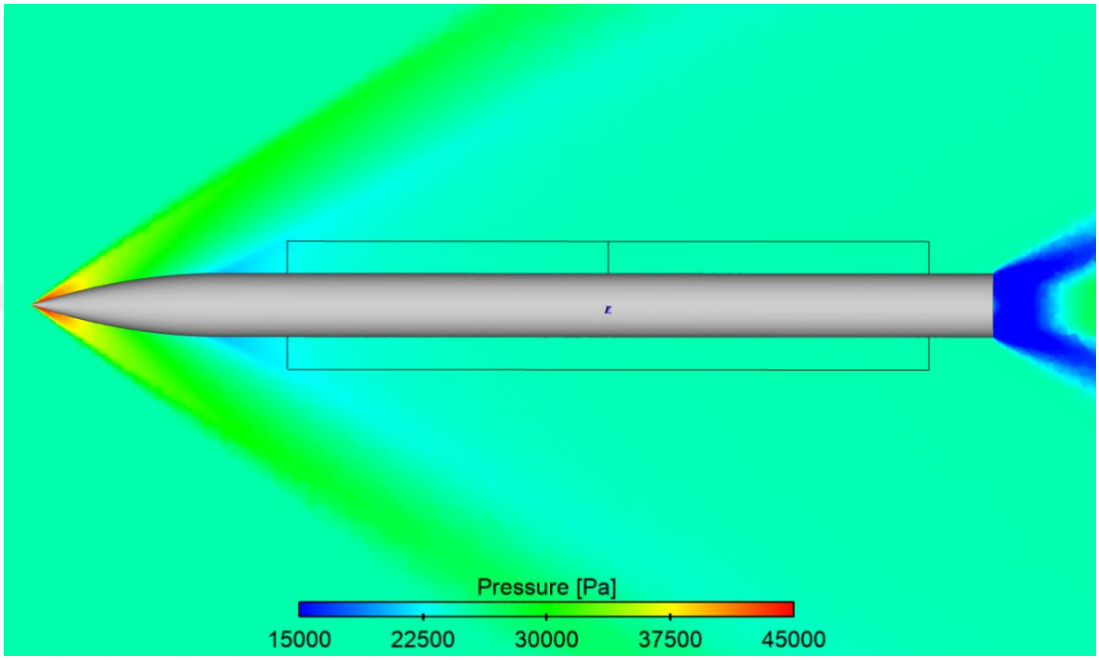

Figure 5.22. Pressure Contours for Jet off Case and M_{inf}=2

For relatively low free-stream flow velocities, shifting low pressure region of the jet plays a major role in the determination of the jet performance as explained before. However, at higher free-stream velocities jet plume and recirculation region become smaller, hence the advantage of the aftjet diminishes. At higher free-stream velocities, back pressure might be one of factors that affect the jet performance. First, it is examined with pressure contours in Figure 5.22 and Figure 5.23 and it is observed that aftjet faces almost same free-stream pressure which can be named as back pressure. Furthermore, the back pressure at the vicinity of the forejet location decreases slightly for higher free-stream velocities. The lower surface pressure at the vicinity of the forejet location occurs due to increase in the flow velocity at the downstream of the nose shock.

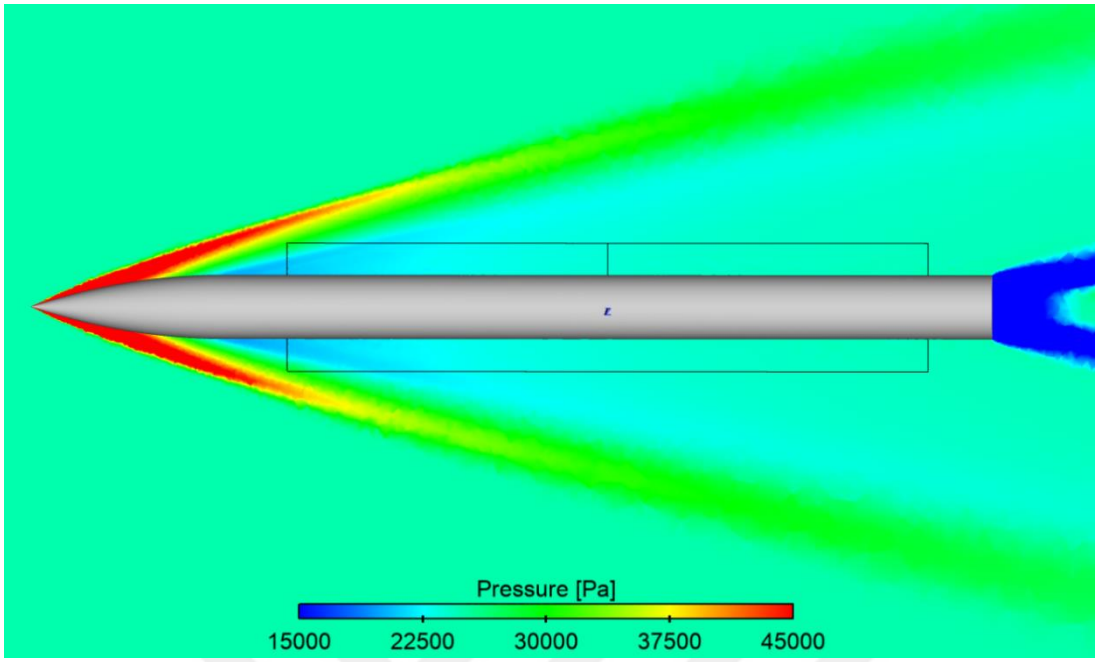

Figure 5.23. Pressure Contours for Jet off Case and M_{inf}=4.5

For a clear representation, surface pressure distribution at different free-stream velocities for jet-off condition is presented in Figure 5.24, and back pressure at the location of the forejet drops around 1.7 kPa as the Mach number is increased from 2 to 4.5 and showing a consistent trend at intermediate flow velocities, while the change in the back pressure at the location of the aftjet is even less. The decrease in the back pressure at higher free-stream velocities is negligible with respect to a much higher jet pressure of 639 kPa. As a summary, for higher free-stream flow velocities, reattachment shock determines the jet performance rather than low-pressure region shift.

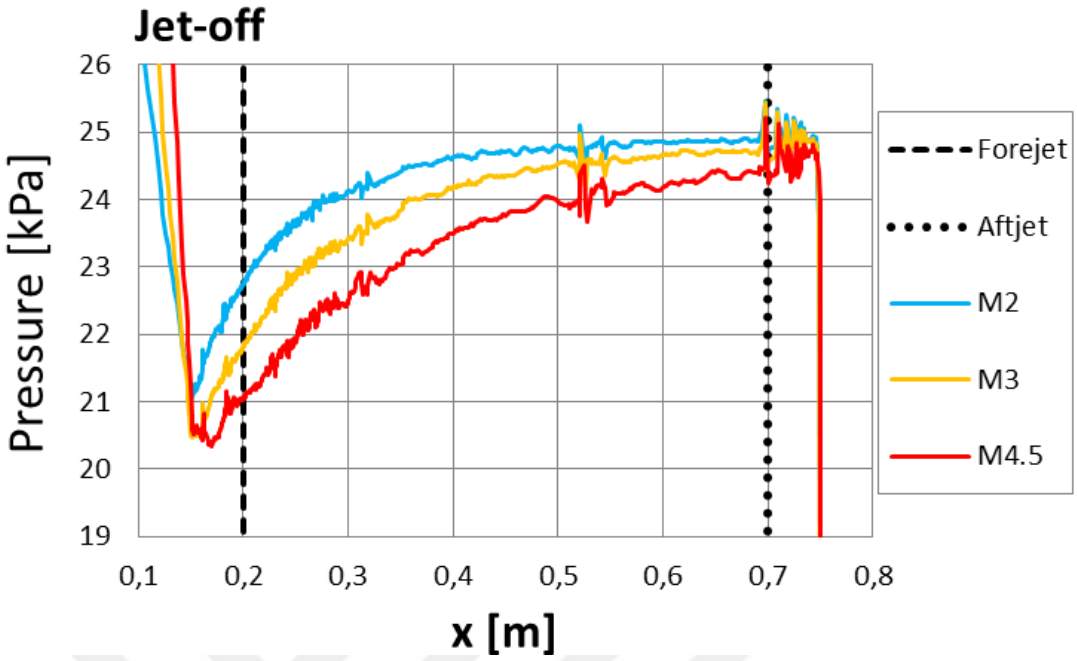

Figure 5.24. Surface Pressure Distribution for Jet off Case and Several Free-stream Flow Velocities

5.3. Effect of the Jet Exit Mach Number at Different Incidence Angles

In this section, effect of Mach at the jet exit is inspected at several incidence angles for free-stream flow velocity Mach 2. Missile is operating at an altitude of 10,4 km and jet properties change with jet exit Mach number and calculations are presented in the Appendix. First operating point of the jet is selected with a jet exit Mach number of 2, a pressure of 639 kPa, a temperature of 220.7 K and a mass flow rate of 0.2312 kg/s, which are the used properties in the study, till now. Flow conditions for conducted numerical simulations in this section are presented in the Table 5.3 and jet flow properties for different jet exit Mach numbers are presented in the Table 0.1. In this section, results of conducted 48 runs are presented.

First, normal force and pitching moment results are presented in Figure 5.25 and Figure 5.26, respectively.

Table 5.3. *Inspection of the Jet Exit Mach Number at Several Incidence Angles*

Flow Conditions	
Location	Forejet, Aftjet
M_{inf}	2.0
α(°)	-5, 0, 5
M_{jet}	0.7, 0.8, 0.9, 1, 1.5, 2, 2.5, 3

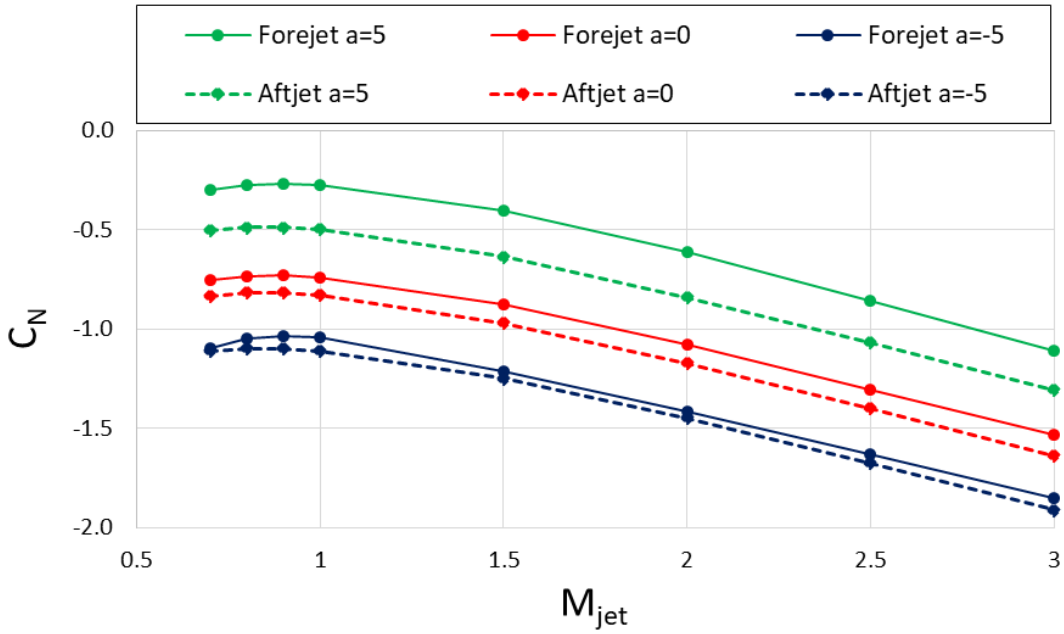

Figure 5.25. C_N Results at Several Jet Flow Velocities and Incidence Angles

In Figure 5.25 and Figure 5.26, similar colors have been used for consistency, however colors represent different cases in two figures, e.g., green lines in Figure 5.25 show the results at 5° incidence angle for both locations and in Figure 5.26, they represent 'Jet-Body' case for both locations. In Figure 5.26, moment results of aftjet is multiplied by '-1' as before, in order to obtain a graph that contain comparable values. When normal force and pitching moment results are examined, one can see that, with increasing jet exit Mach number, jet performance increases as it is expected. Also, for sonic and subsonic jet exit Mach numbers, jet performance drops.

From Figure 5.25 and Figure 5.26, the aftjet shows greater performance for supersonic jet exit velocities. Also, for subsonic jet exit velocities and non-zero incidence angles both locations created moments that are close to each other. For a detailed comparison, moment amplifications are calculated and presented.

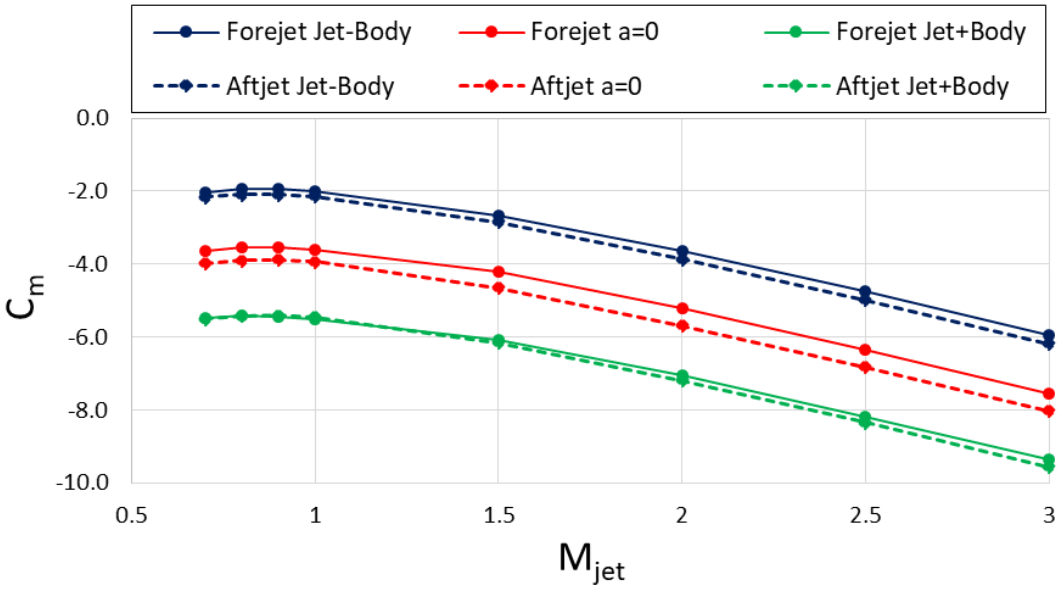

Figure 5.26. C_m Results at Several Jet Flow Velocities and Incidence Angles

Subsonic jet exit velocities can be examined for jet and free-stream flow interactions using Figure 5.27, Figure 5.28 and Figure 5.29. However, one should take into consideration that, moment amplification factors are calculated by dividing the sum of moments due to jet thrust and jet, free-stream flow interactions, by the moment due to jet thrust alone. Since the thrust and moment of the jet with subsonic flow velocities are smaller than the one for higher velocities, the difference between moment amplification factors of two locations ground on little differences. Therefore, it is complicated to make physical comments by examining the flow domains.

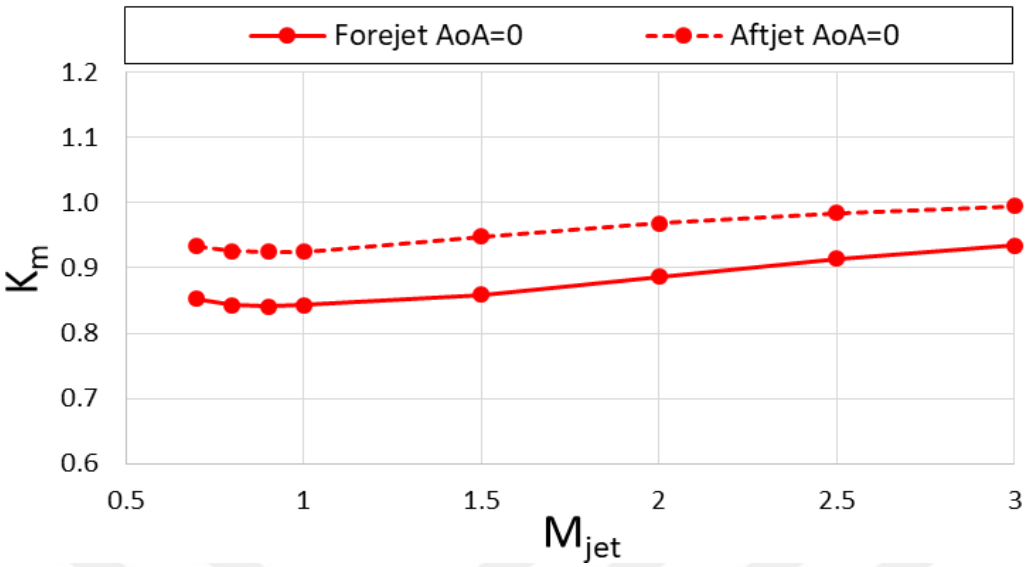

Figure 5.27. K_m Values at Several Jet Exit Velocities and Zero Incidence Angle

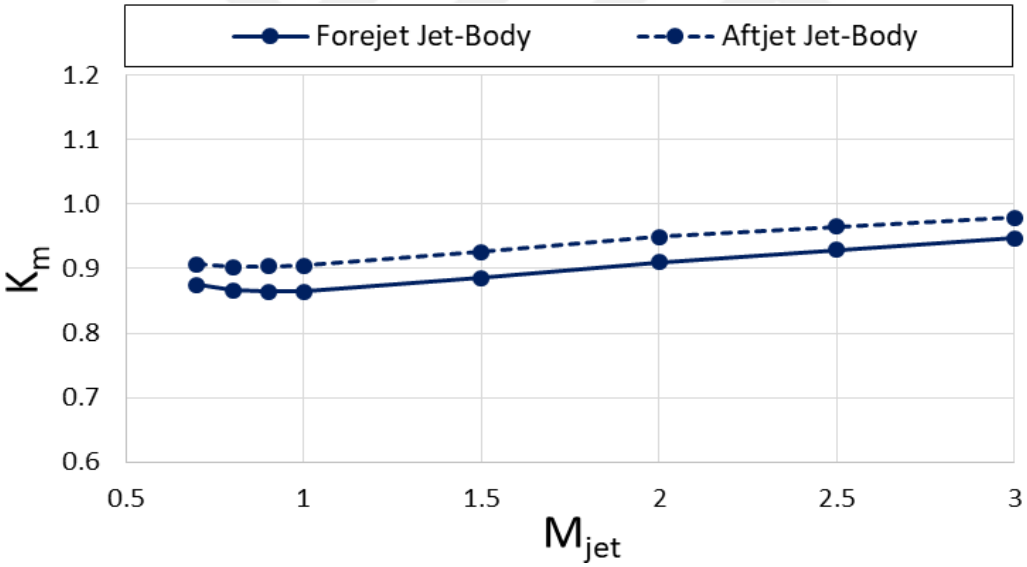

Figure 5.28. K_m Values at Several Jet Exit Velocities and 'Jet-Body' Case

One can see from Figure 5.27, Figure 5.28 and Figure 5.29 that, both locations result in similar performances at subsonic jet flow velocities for 'Jet + Body' case. Furthermore, the aftjet location results in better performance for zero incidence angle and 'Jet – Body' cases at subsonic jet exit velocities. For the examination of the recent

results, pressure contours and distributions of free-stream at a Mach number of 2, jet exit Mach number of 0.8 and zero incidence angle are presented in Figure 5.30, Figure 5.31 and Figure 5.32.

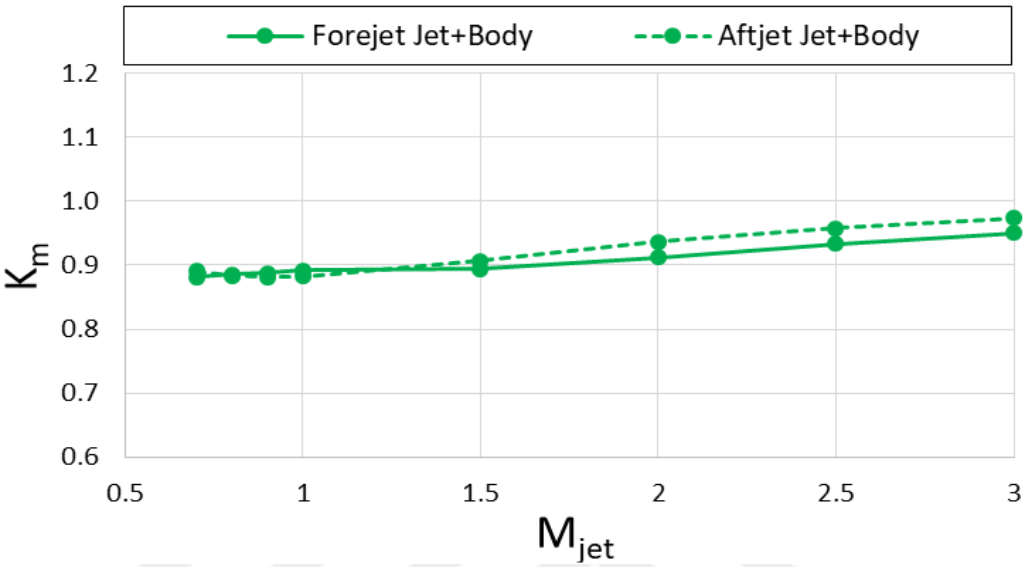

Figure 5.29. K_m Values at Several Jet Exit Velocities and 'Jet+Body' Case

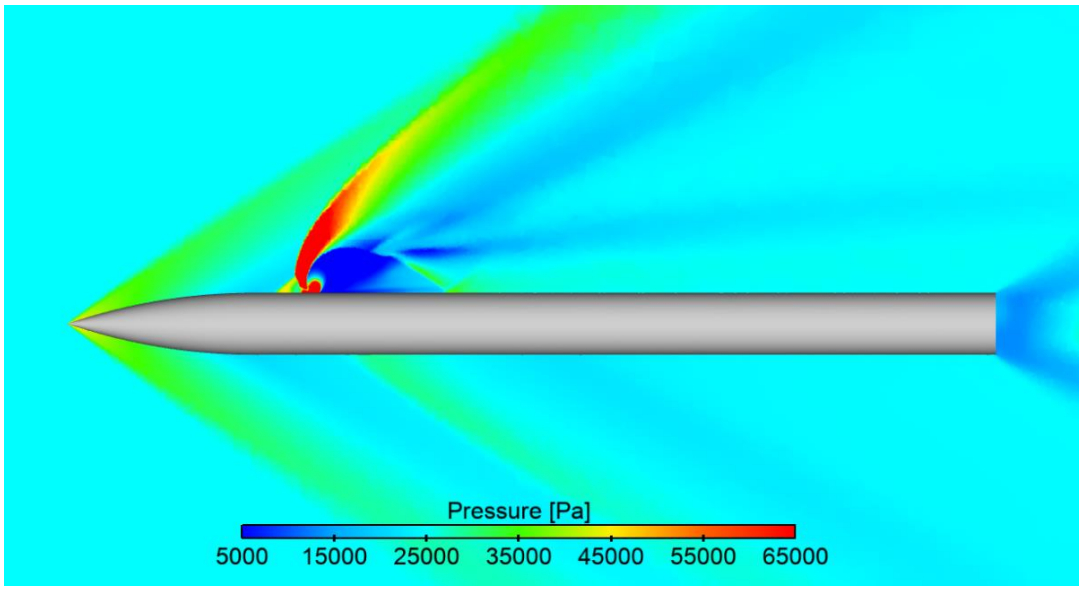

Figure 5.30. Pressure Contours for the Forejet Operating at M_{jet}=0.8, M_{inf}=2 and Zero Incidence Angle

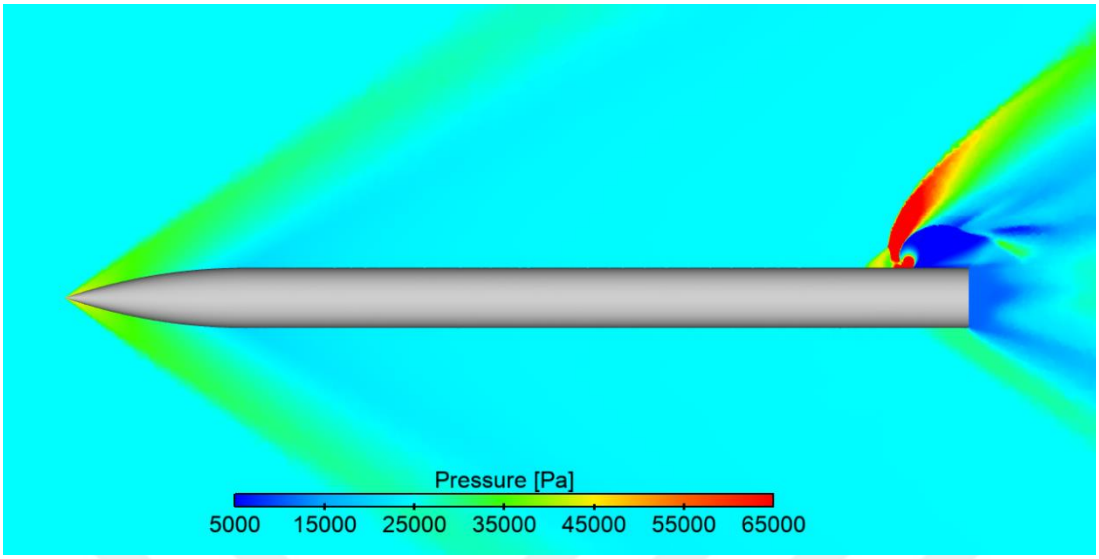

Figure 5.31. Pressure Contours for the Aftjet Operating at M_{jet}=0.8, M_{inf}=2 and Zero Incidence Angle

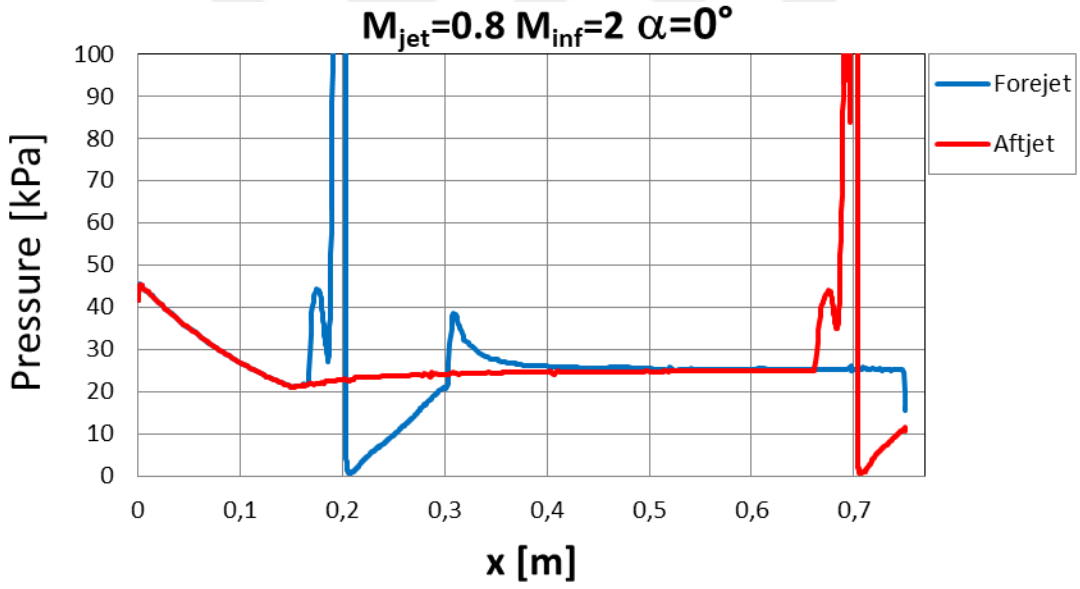

Figure 5.32. Pressure Coefficient Distribution for M_{jet}=0.8, M_{inf}=2 and Zero Incidence Angle

After the examination of Figure 5.32 it is observed that, low-pressure region is 2.16-D in length for the forejet case and 0.93-D for the aftjet case which are examined for the flow conditions zero incidence angle and free-stream, jet flows at a Mach number

of 2 and 0.8, respectively. Hence, pitching moment coefficient of the aftjet is greater around 9.9% with respect to the one of the forejet.

Next, ‘Jet - Body’ case for both locations of the jet, the same jet and free-stream flow conditions are presented in Figure 5.33, Figure 5.34 and Figure 5.35.

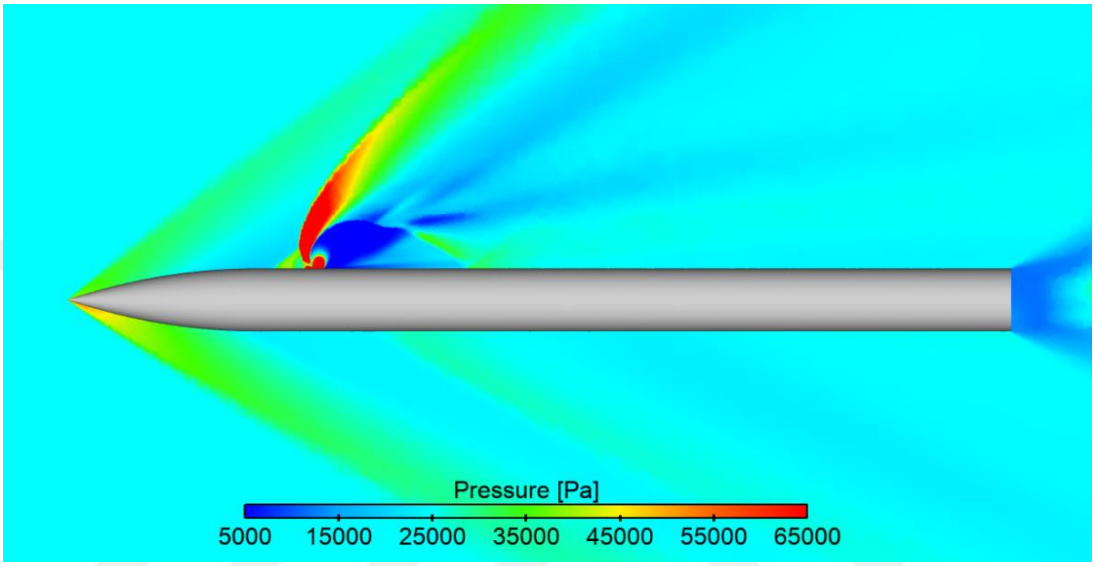

Figure 5.33. Pressure Contours for the Forejet Operating at M_{jet}=0.8 and M_{inf}=2 (‘Jet-Body’ Case)

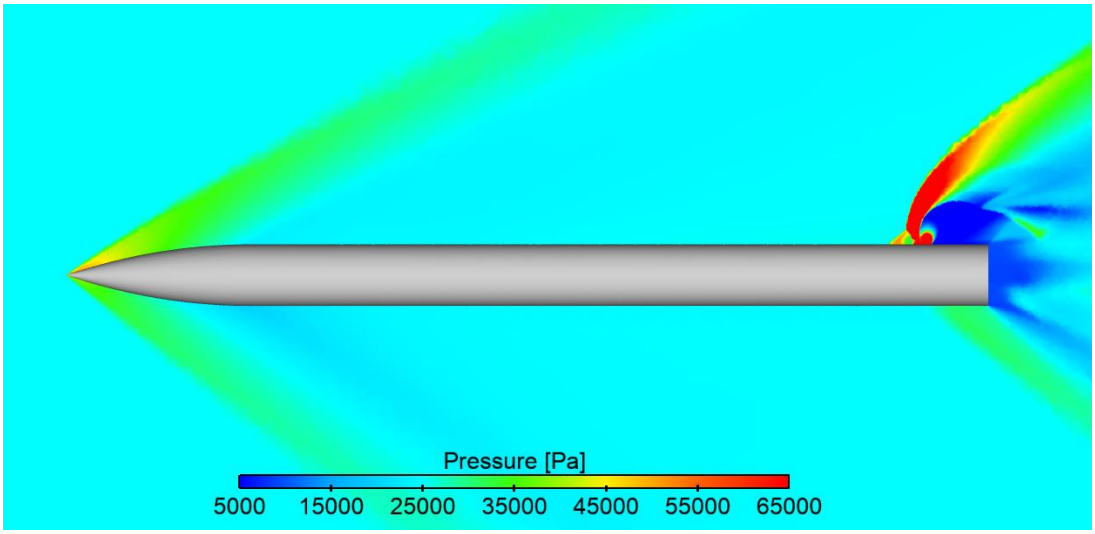

Figure 5.34. Pressure Contours for the Aftjet Operating at M_{jet}=0.8 and M_{inf}=2 (‘Jet-Body’ Case)

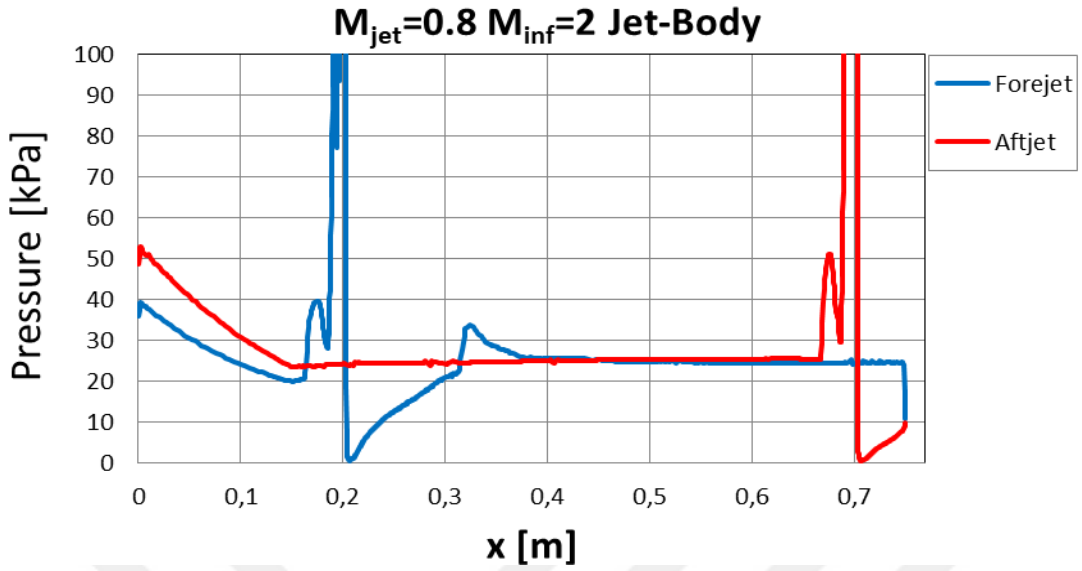

Figure 5.35. Pressure Coefficient Distribution for M_{jet}=0.8 and M_{inf}=2 ('Jet-Body' Case)

After the examination of Figure 5.35 it is observed that, low-pressure region is 2.24-D in length for the forejet and 0.93-D for the aftjet which are examined for the flow conditions 'Jet - Body' case and free-stream, jet flows at a Mach number of 2 and 0.8, respectively. Hence, pitching moment coefficient of the aftjet is greater around 7.0% with respect to the one of the forejet due to low-pressure region shift.

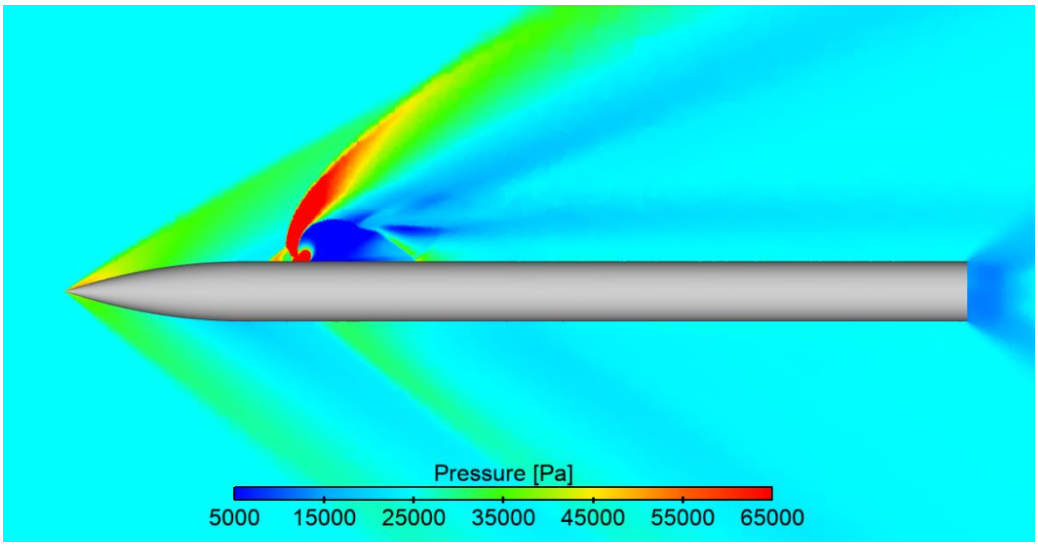

Figure 5.36. Pressure Contours for the Forejet Operating at M_{jet}=0.8 and M_{inf}=2 ('Jet+Body' Case)

Finally, ‘Jet + Body’ case at the same flow conditions is presented for further examination of subsonic jet exit at several angles of attack and pressure contours and distributions of this case is presented in Figure 5.36, Figure 5.37 and Figure 5.38.

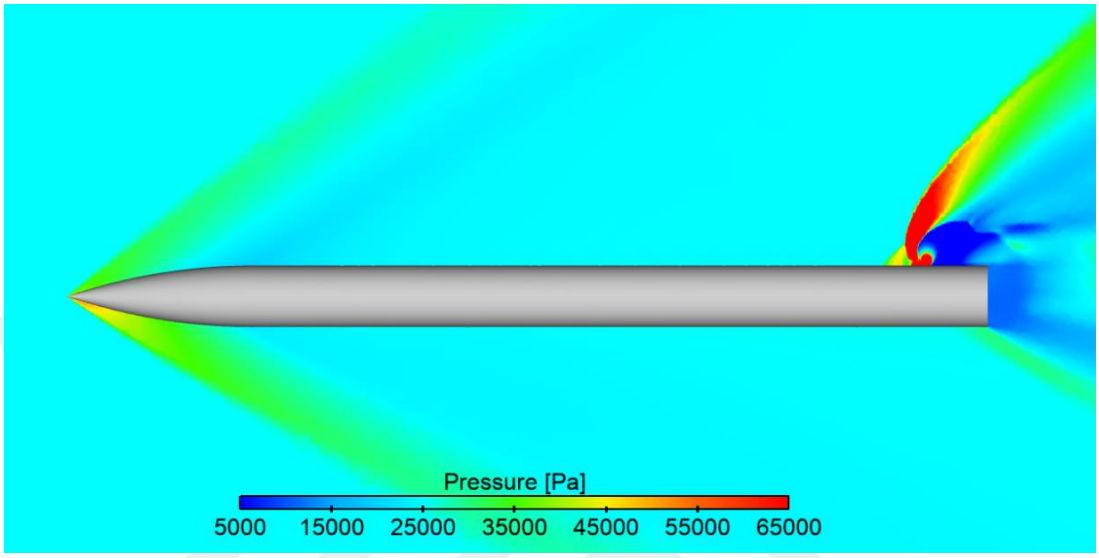

Figure 5.37. Pressure Contours for the Aftjet Operating at M_{jet}=0.8 and M_{inf}=2 (‘Jet+Body’ Case)

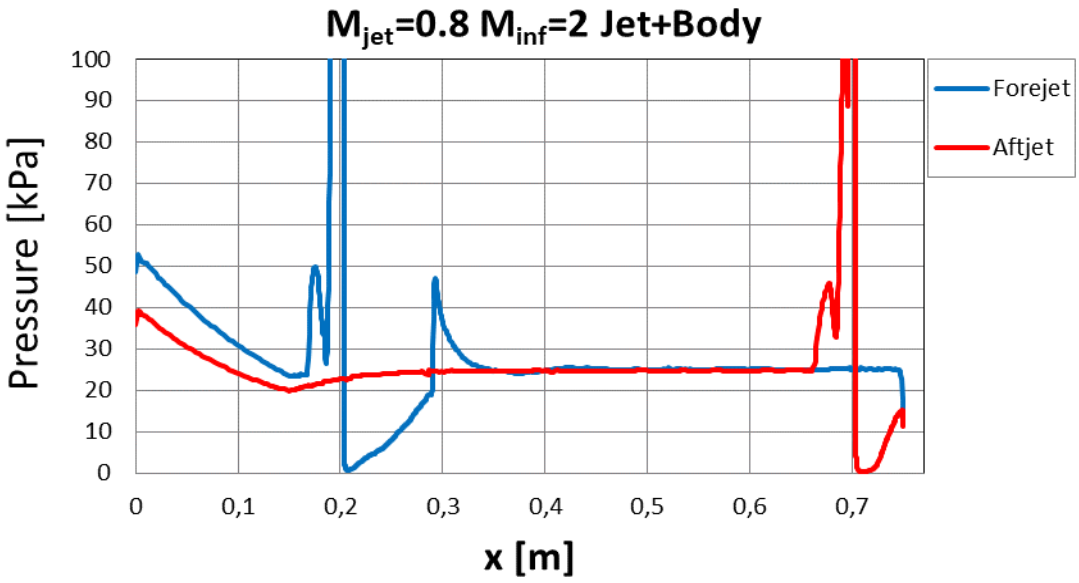

Figure 5.38. Pressure Coefficient Distribution for M_{jet}=0.8 and M_{inf}=2 (‘Jet+Body’ Case)

From Figure 5.38, low-pressure region is 1.78-D in length for the forejet and 0.93-D for the aftjet which are examined for the flow conditions ‘Jet + Body’ case and free-stream, jet flows at a Mach number of 2 and 0.8, respectively. Moreover, pitching moment coefficients of the aftjet and forejet almost identical.

The pressure contours and distributions for a jet exit Mach number of 0.8 and a free-stream flow at a Mach number of 2 at different incidence angles are presented from Figure 5.30 to Figure 5.38. Also, from the amplification factor graphs, it is expected to observe that flow domains of both locations result in similar performance for ‘Jet + Body’ case, while for other incidence angles it is expected to observe reasons for better performance of the aftjet. First, ‘Jet - Body’ and zero incidence angle cases are examined and explained. Figure 5.30, Figure 5.31, Figure 5.33 and Figure 5.34 present the pressure contours and Figure 5.32 and Figure 5.35 present the pressure distributions of these cases. From the figures one can conclude that, better performance of the aftjet is due to shift of the wake region. Next, ‘Jet + Body’ case is examined. For this case and similar jet performances obtained from two jet locations as presented in Figure 5.29. Examinations for this case are presented in Figure 5.36, Figure 5.37 and Figure 5.38. It is concluded that, the shift of wake region to the outside of the missile increases the performance of the aftjet. However, it was not able to observe an effect that balances the performance of the forejet to the one for aftjet. A further study should be conducted for the subsonic jet flow velocities in order to make additional comments for this case.

Next, supersonic jet exit velocities at different incidence angles are inspected using the presented pressure contours and distributions at the 180° line. One can see from Figure 5.27, Figure 5.28 and Figure 5.29 that the aftjet results in a better performance at supersonic jet exit velocities which was explained for zero incidence angle by the shift of wake region as presented in Figure 5.6, Figure 5.7 and Figure 5.8. Furthermore, non-zero incidence angles are examined using the pressure contours and distributions.

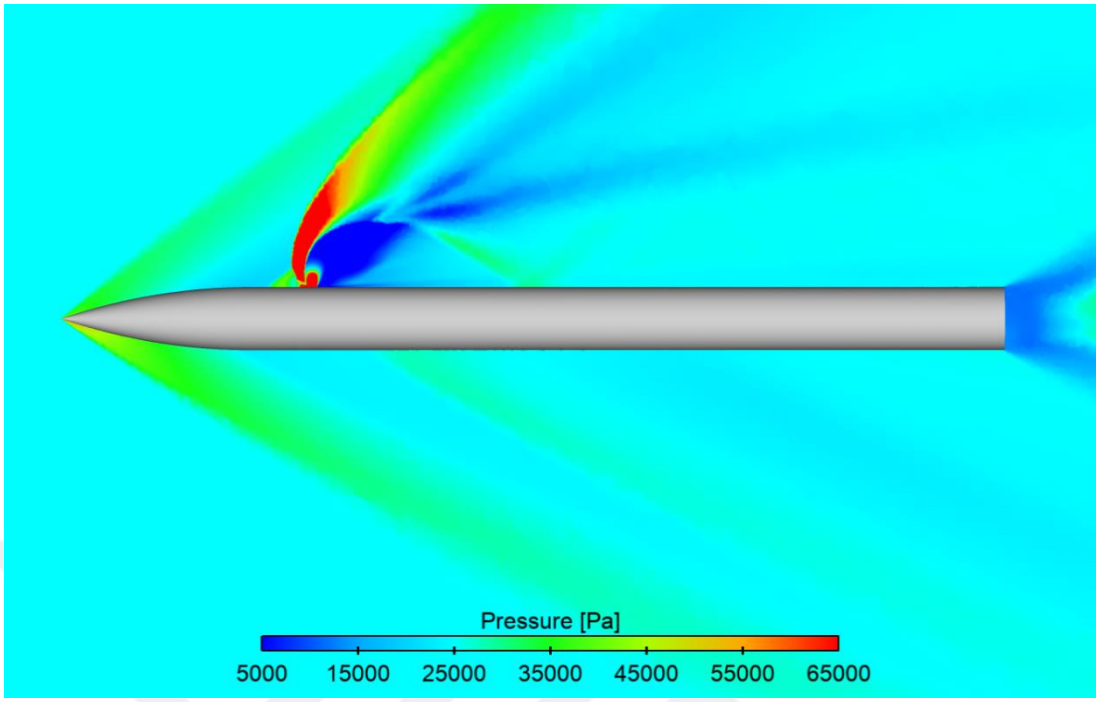

Figure 5.39. Pressure Contours for the Forejet Operating at M_{jet}=2 and M_{inf}=2 ('Jet-Body' Case)

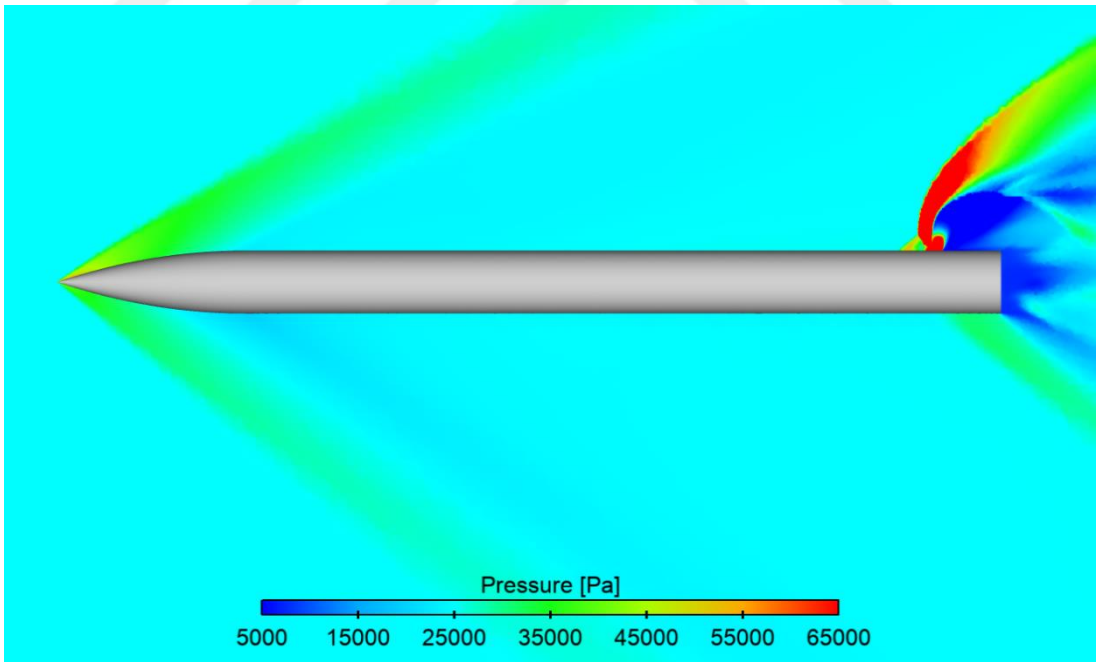

Figure 5.40. Pressure Contours for the Aftjet Operating at M_{jet}=2 and M_{inf}=2 ('Jet-Body' Case)

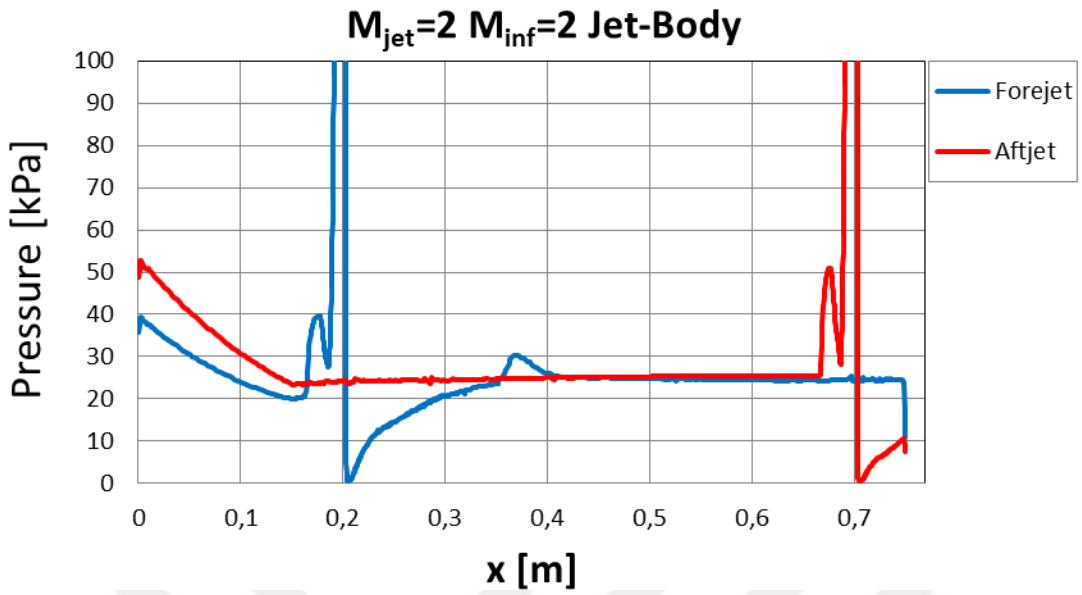

Figure 5.41. Pressure Coefficient Distribution for M_{jet}=2 and M_{inf}=2 ('Jet-Body' Case)

Comparisons for 'Jet - Body' case for both locations of the jet when the jet exit and free-stream are both at a Mach number of 2, are presented in Figure 5.39, Figure 5.40 and Figure 5.41. Hence it is observed that, low pressure region lengths are 3.02-D for forejet case and 0.93-D for aftjet case. As a result of this shift, pitching moment coefficient of the aftjet is greater around 5.8% with respect to the one of forejet.

Next, pressure contours and distributions of the 'Jet + Body' case for jet and free-stream flow are both at a Mach number of 2 are presented in Figure 5.49, Figure 5.50 and Figure 5.51.

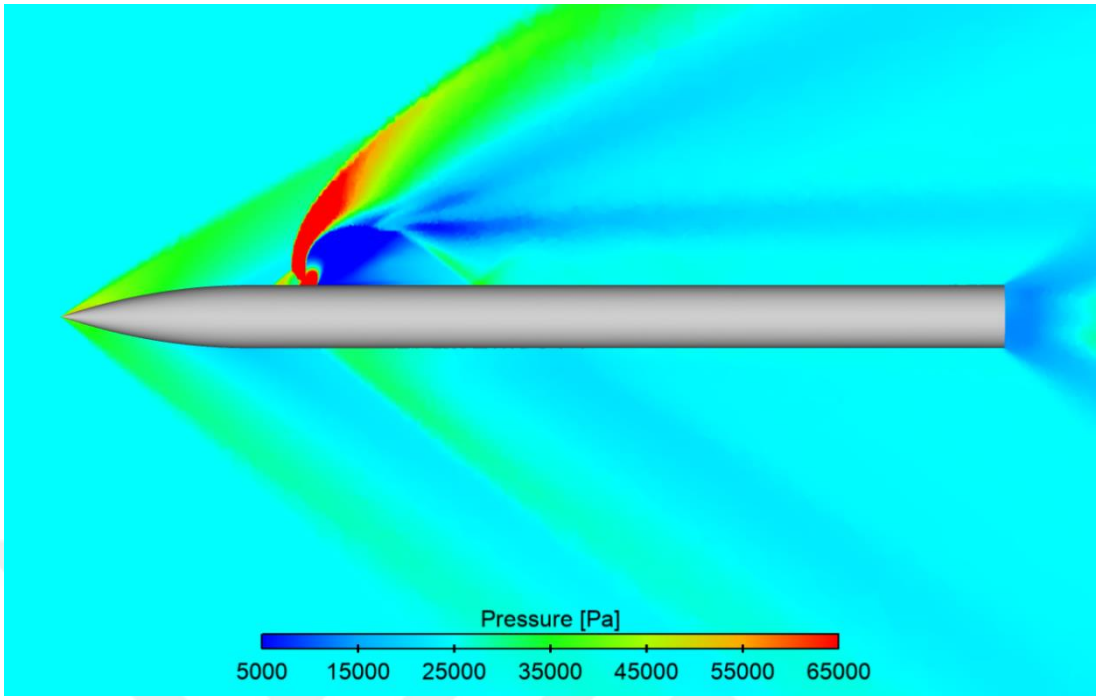

Figure 5.42. Pressure Contours for the Forejet Operating at M_{jet}=2 and M_{inf}=2 ('Jet+Body' Case)

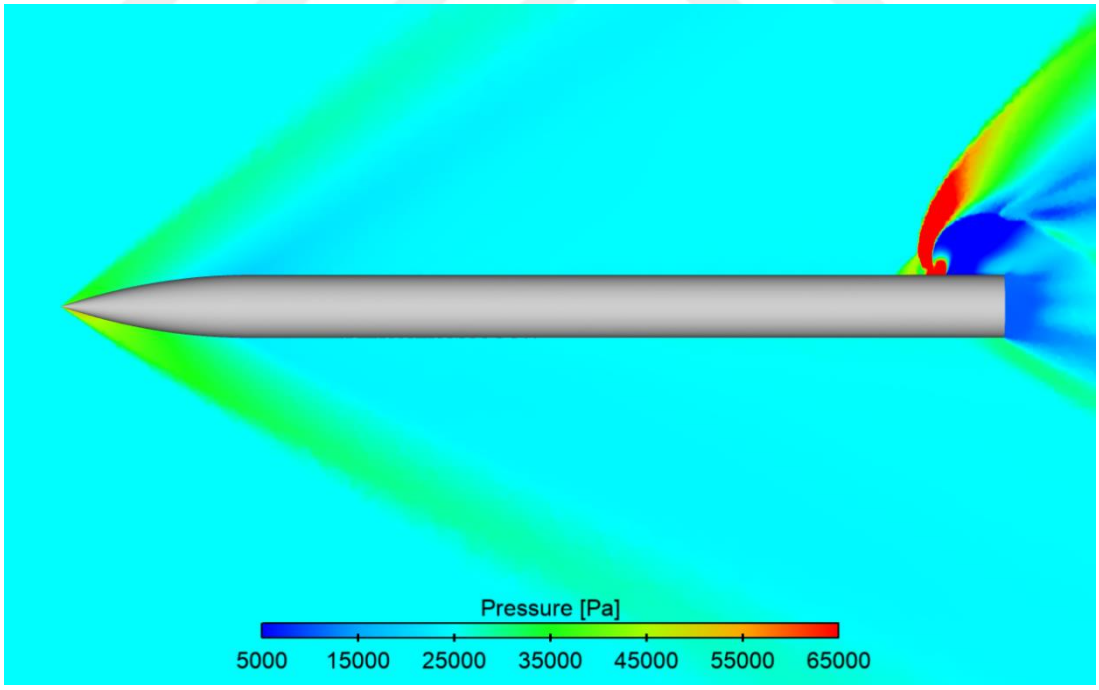

Figure 5.43. Pressure Contours for the Aftjet Operating at M_{jet}=2 and M_{inf}=2 ('Jet+Body' Case)

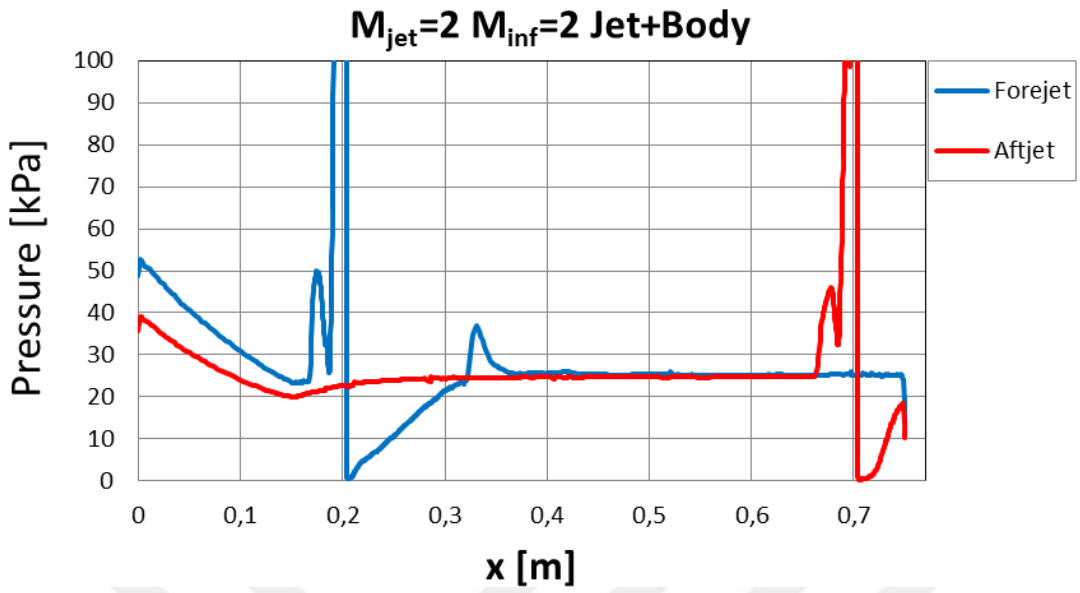

Figure 5.44. Pressure Coefficient Distribution for M_{jet}=2 and M_{inf}=2 ('Jet+Body' Case)

The same flow phenomenon are observed for the 'Jet + Body' case as presented in Figure 5.42, Figure 5.43 and Figure 5.51. Displacement of low-pressure region to the outside of the missile body explains the better performance for the aftjet. From Figure 5.51 it is seen that, length of the wake region in the axial direction is 2.46-D for the forejet case and 0.93-D for the aftjet case. Therefore, pitching moment coefficient of the aftjet case is greater around 1.9% than the one of forejet case.

So far in this section, the effect of jet exit velocity is examined at a free-stream Mach number of 2 and several incidence angles, and several comments are made on the jet performance. It is observed that, the aftjet location shows a better performance for all inspected incidence angles for supersonic jet exit velocities. At subsonic jet exit velocities, for zero incidence angle and 'Jet - Body' cases aftjet location results in greater performance, and for the 'Jet + Body' case both jet locations result in similar performances.

5.4. Effect of the Jet Exit Mach Number at Different Free-Stream Velocities

In this section, the effect of the Mach number at the jet exit is inspected at different free-stream flow velocities. Missile is operating at 10.4 km altitude and jet properties change with jet exit Mach as explained. Flow conditions for conducted numerical simulations in this section are presented in the Table 5.4. At different jet exit Mach numbers, the jet flow properties are presented in the Table 0.1, as explained in the 'Section 5.3'. In this section, result of conducted 48 runs are presented.

Table 5.4. *Inspection of the Jet Exit Mach Number at Several Free-Stream Flow Velocities*

Flow Conditions	
Location	Forejet, Aftjet
M_{inf}	1.5, 2, 3
AoA(°)	0
M_{jet}	0.7, 0.8, 0.9, 1, 1.5, 2, 2.5, 3

First, the jet flow velocity is examined by considering the axial force coefficient and comments are made using axial force coefficient graphs and pressure contours.

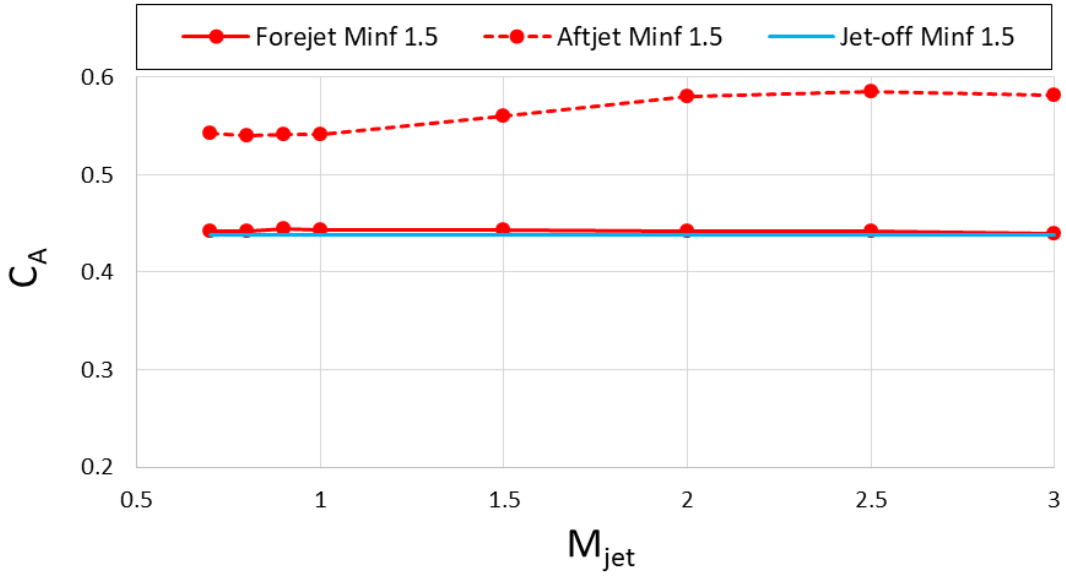

Figure 5.45. C_A Results at Several Jet Exit Velocities and M_{inf}=1.5

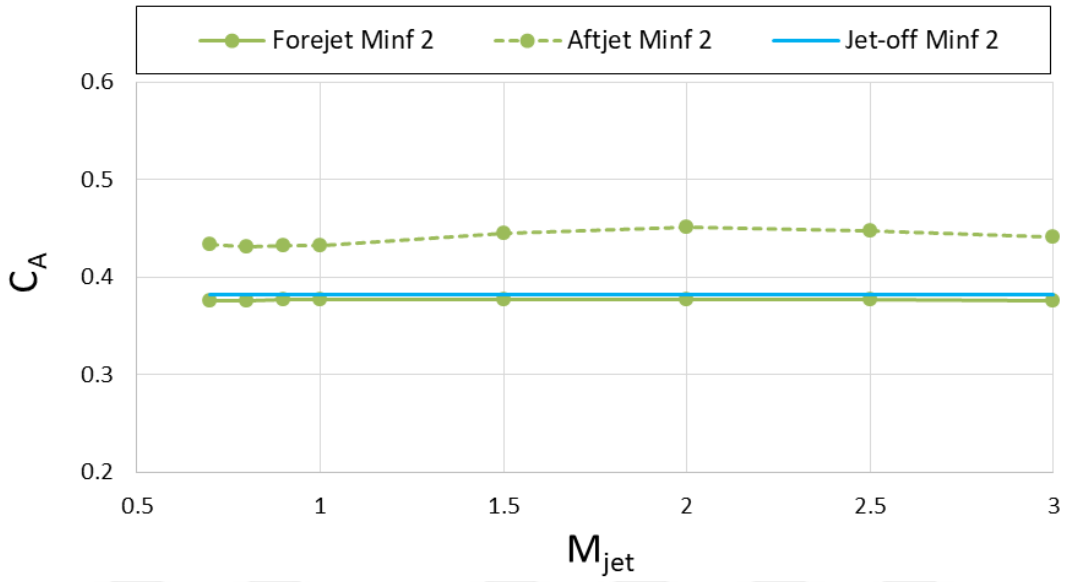

Figure 5.46. C_A Results at Several Jet Exit Velocities and M_{inf}=2

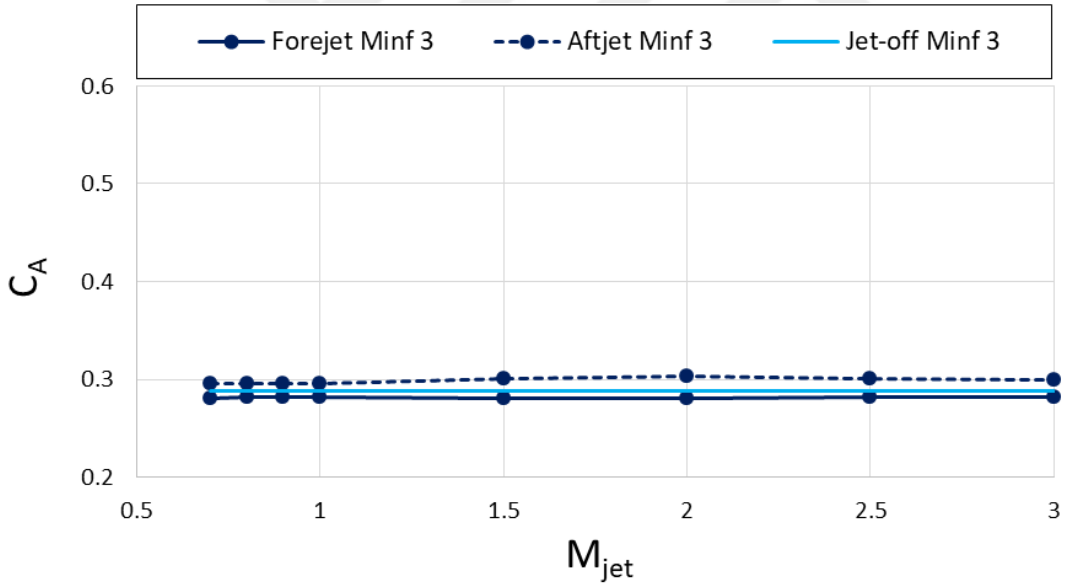

Figure 5.47. C_A Results at Several Jet Exit Velocities and M_{inf}=3

With increasing Mach number, the axial force coefficient decreases which is a characteristic behavior of supersonic flow regimes as explained during the inspection of spouting angle. For all examined free-stream and jet flow velocities, it can be

observed that, the forejet changes the axial force coefficient negligibly as expected. However, when the jet is at the aft-location, axial force coefficient increases considerably due to increase in the base drag as it is proven in the previous sections.

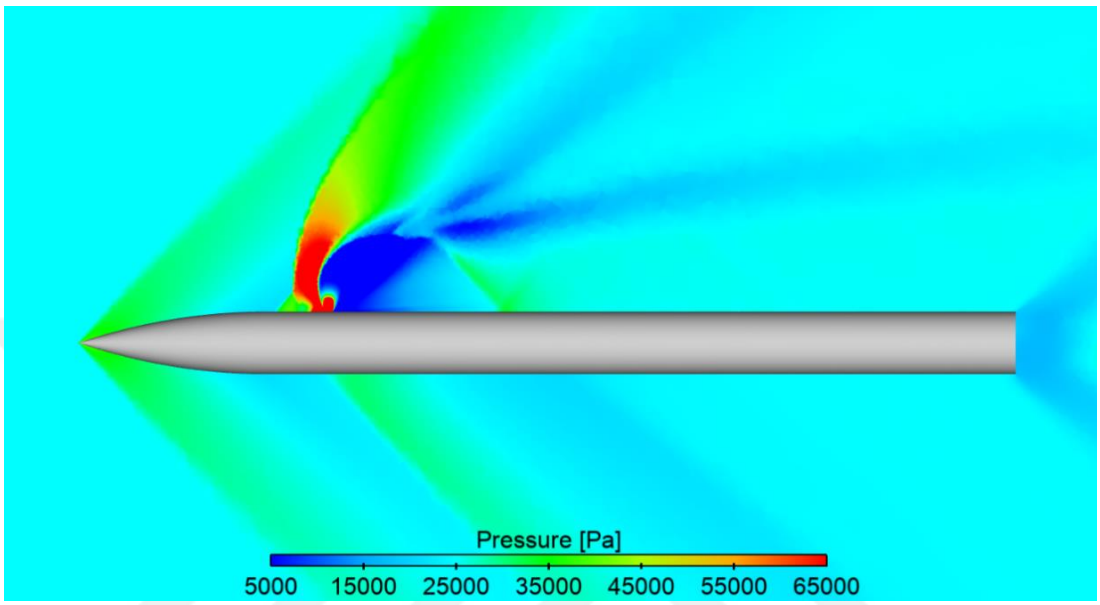

Figure 5.48. Pressure Contours for the Forejet Operating at M_{jet}=2 and M_{inf}=1.5

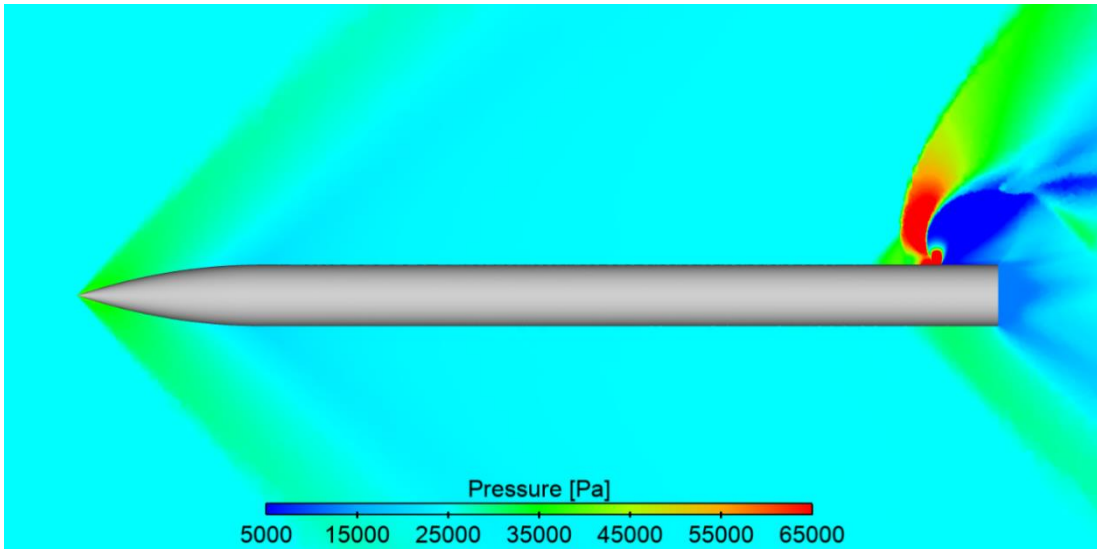

Figure 5.49. Pressure Contours for the Aftjet Operating at M_{jet}=2 and M_{inf}=1.5

The difference between the axial force coefficients of the two jet locations, decreases for higher free-stream velocities, which can be observed from Figure 5.45, Figure 5.46, and Figure 5.47. For jet flow at a Mach number of 2 and the aftjet case, axial force coefficient increases with respect to jet-off condition 32.3% for M_{inf}=1.5, 17.9% for M_{inf}=2.0, 5.3% for M_{inf}=3.0. To be able to comment further on this result, pressure contours are inspected. Pressure contours for a free-stream Mach number of 1.5 in Figure 5.48 and Figure 5.49, for a Mach number of 2 in Figure 5.6 and Figure 5.7 and for Mach 3 in Figure 5.50 and Figure 5.51 are presented. For lower Mach numbers, i.e. for Mach 1.5, jet plume becomes a bigger obstruction to free-stream flow since jet flow travels in a path that is closer to the normal of the jet exit plane. For higher free-stream Mach numbers, jet plume becomes a smaller obstruction to free-stream flow and increases axial force coefficient less with respect to lower free-stream flow velocities. Two reasons for the jet plume being a smaller obstacle are the bending of the jet plume towards downstream and creating a smaller plume in a greater total pressure, which can be observed from presented pressure contours.

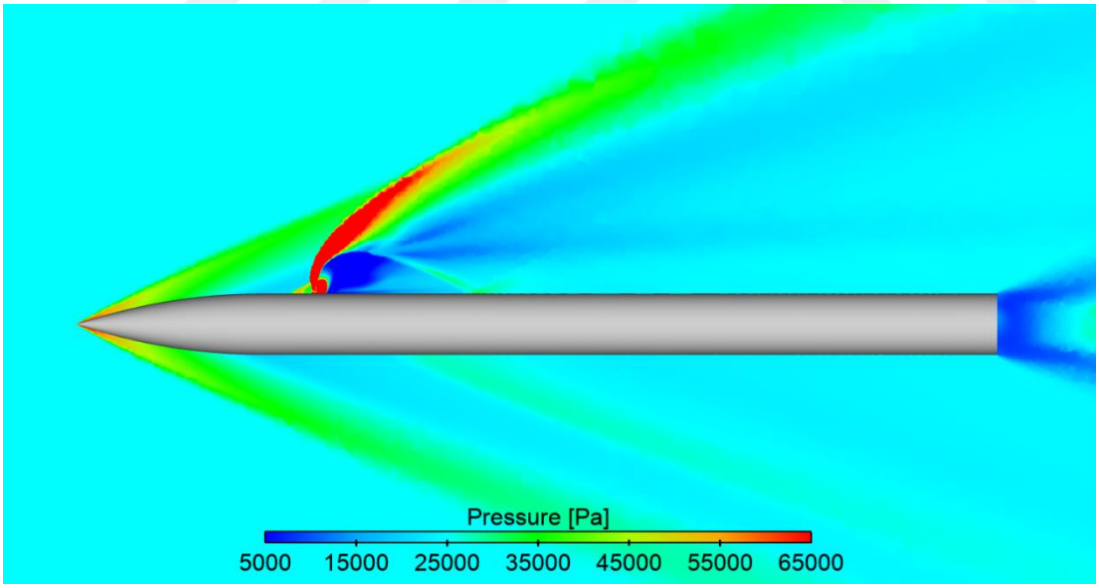

Figure 5.50. Pressure Contours for the Forejet Operating at M_{jet}=2 and M_{inf}=3

Furthermore, for lower jet exit velocities axial force coefficient increases by an amount which is smaller than the increase in supersonic jet exit speeds. The reason for this is, the jet plume becomes smaller at subsonic jet flows as shown in Figure 5.57, Figure 5.58, Figure 5.60, Figure 5.61, Figure 5.64 and, Figure 5.65.

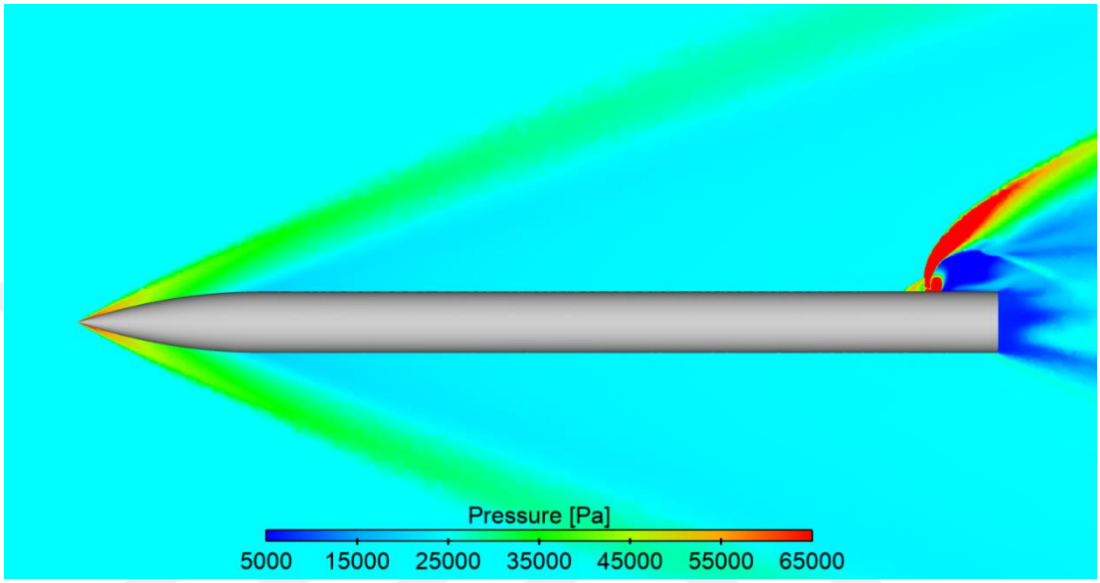

Figure 5.51. Pressure Contours for the Aftjet Operating at M_{jet}=2 and M_{inf}=3

Next, the effect of jet flow velocity is examined by considering the missile maneuverability using the normal force and pitching moment coefficients and moment amplification factors. First, normal force and pitching moment coefficients are presented in Figure 5.52 and Figure 5.53, respectively.

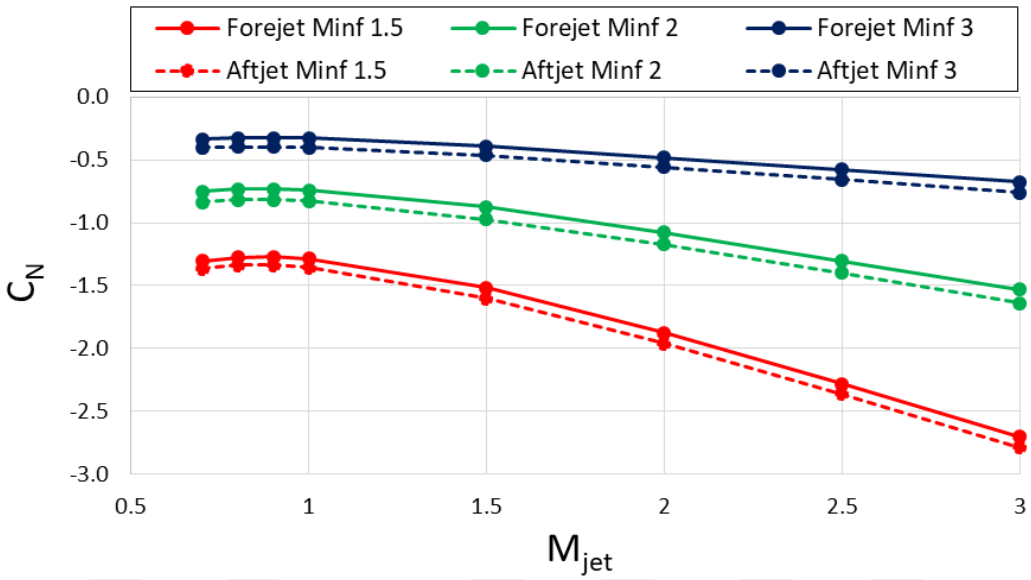

Figure 5.52. C_N Results at Several Jet and Free-Stream Flow Mach Numbers

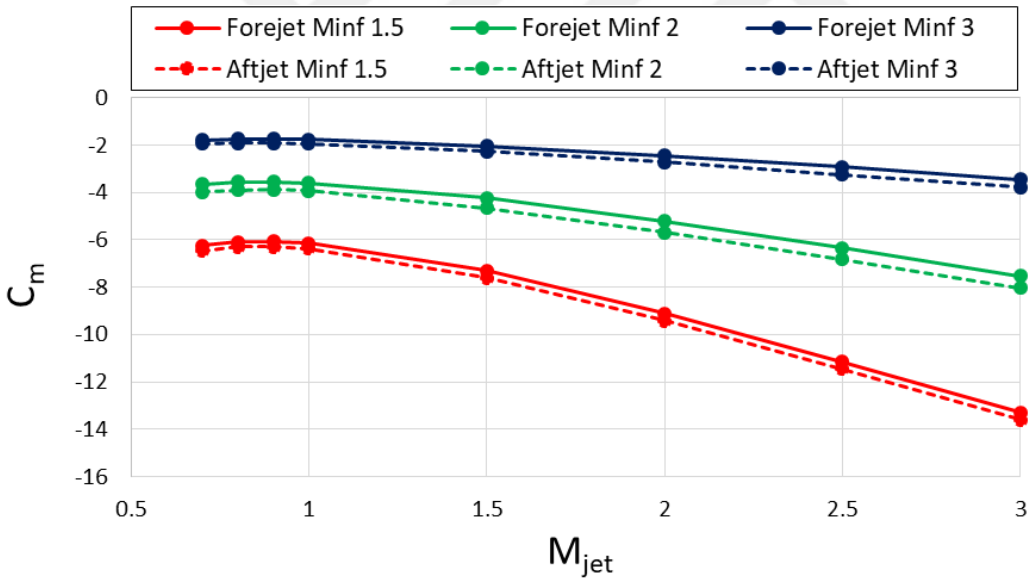

Figure 5.53. C_m Results at Several Jet and Free-Stream Flow Mach Numbers

In Figure 5.53, pitching moment results of the aftjet is multiplied with '-1' again, in order to obtain comparable results with the forjet as explained previously. From Figure 5.52 and Figure 5.53, it can be seen that force and moment coefficients show a consistent trend with each other. Also, jet performance increases with increasing jet exit velocity for examined free-stream flow velocities, as expected. Also, the aftjet of jet shows a better performance again, for sonic and supersonic jet exit velocities, which is explained as the shifting low-pressure jet wake region beyond the missile body and shown by the pressure contours presented in Figure 5.6, Figure 5.7, Figure 5.48, Figure 5.49, Figure 5.50 and Figure 5.51. Moreover, for detailed examinations of the maneuverability results surface pressure distributions are presented in Figure 5.54 for Minf=1.5, Figure 5.8 for Minf=2 and Figure 5.55 for Minf=3. From Figure 5.54, it is seen that length of the wake region is 2.32-D for forejet and 0.93-D for the aftjet. As a result of this shift, pitching moment coefficient of the aftjet increases around 3.3% with respect to the one of the forejet for M_{jet}=2, M_{inf}=1.5 and zero incidence angle.

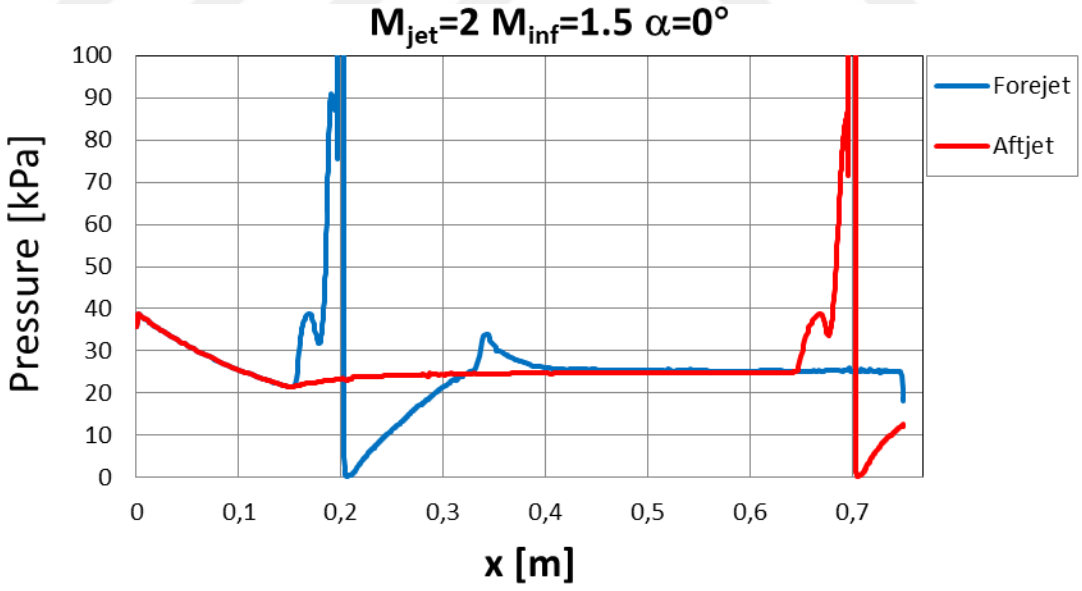

Figure 5.54. Pressure Coefficient Distribution for M_{jet}=2 and M_{inf}=1.5

From Figure 5.55, it is seen that length of the wake region is 2.28-D for forejet and 0.93-D for the aftjet. As a result of this shift, pitching moment coefficient of the aftjet increases around 11.5% with respect to the one of the forejet for M_{jet}=2, M_{inf}=3 and zero incidence angle.

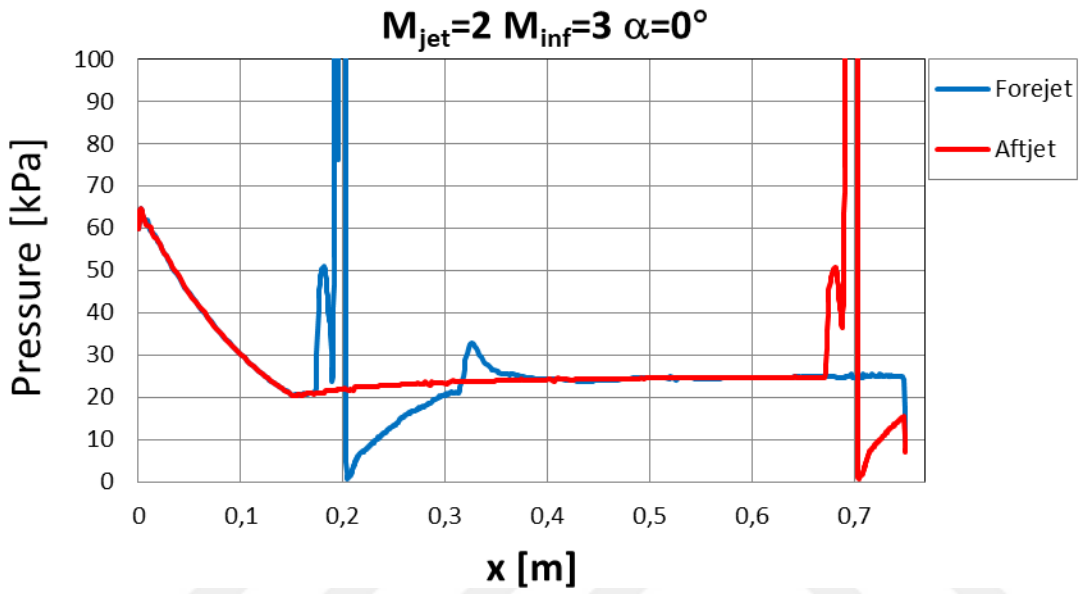

Figure 5.55. Pressure Coefficient Distribution for M_{jet}=2 and M_{inf}=3

Additionally, at sonic and subsonic jet exit velocities, jet performance drops, as it is observed from Figure 5.52 and Figure 5.53. Further examination of the jet exit Mach number at different freestream velocities is carried out by using the moment amplification factors.

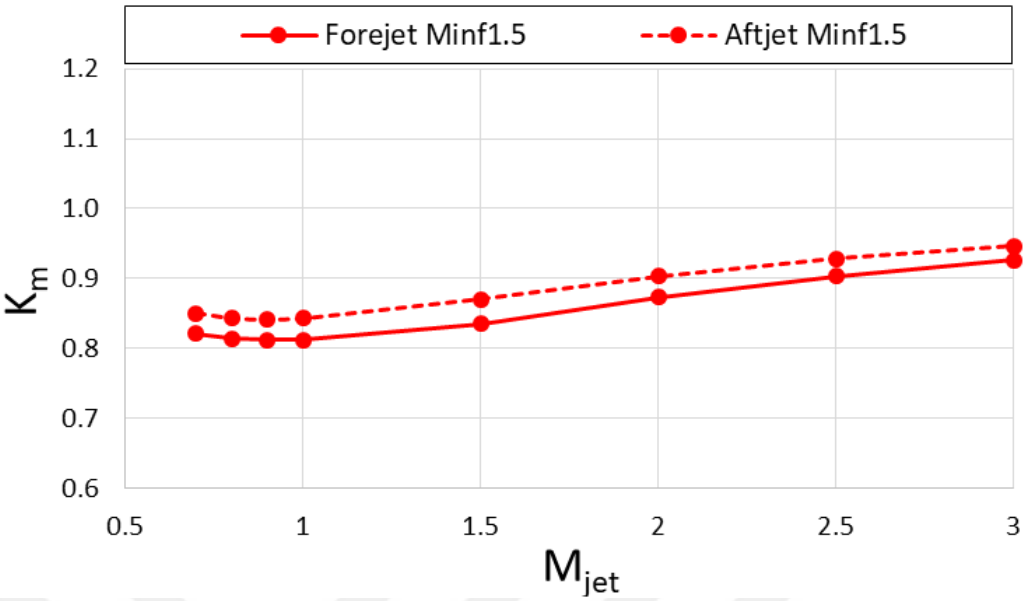

Figure 5.56. K_m Values at Several Jet Exit Velocities and M_{inf}=1.5

First, the moment amplification factor graph is plotted for a free-stream Mach number of 1.5 in Figure 5.56. From this figure, it can be observed that the aftjet results in a better performance for all examined jet exit velocities according to moment amplification factors similar to the moment coefficient results in Figure 5.53. Pressure contours and distributions for a jet exit Mach number of 0.7 and a free-stream flow Mach number of 1.5 for both jet locations are generated in order to examine the subsonic jet exit flows in detail and they are presented in Figure 5.57, Figure 5.58 and Figure 5.60.

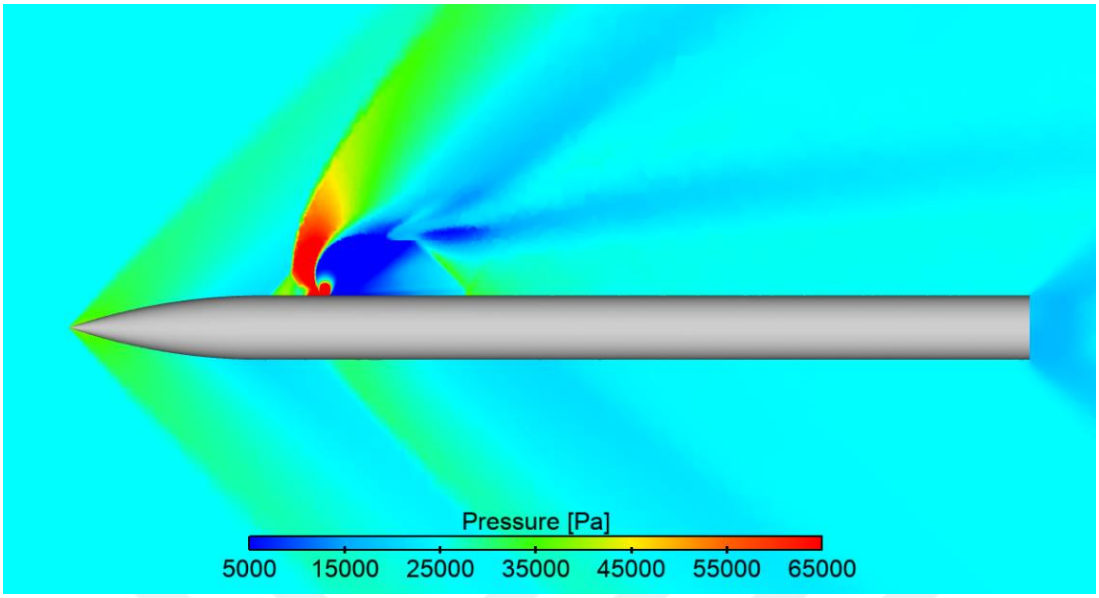

Figure 5.57. Pressure Contours for the Forejet Operating at M_{jet}=0.7, M_{inf}=1.5

From Figure 5.59 it is observed that the length of the wake region is 2.06-D for forejet case and 0.93-D for the aftjet case. As a result of this shift, pitching moment coefficient of the aftjet increases around 3.5% with respect to the one of the forejet for M_{jet}=0.7, M_{inf}=3 and zero incidence angle. Hence, for subsonic jet flows, the wake region gets smaller with respect to supersonic jet exit velocities which can be observed from the presented pressure contours and examination of the surface pressure distributions, even so the shift of low-pressure region to the outside of the missile increases the performance of the aftjet.

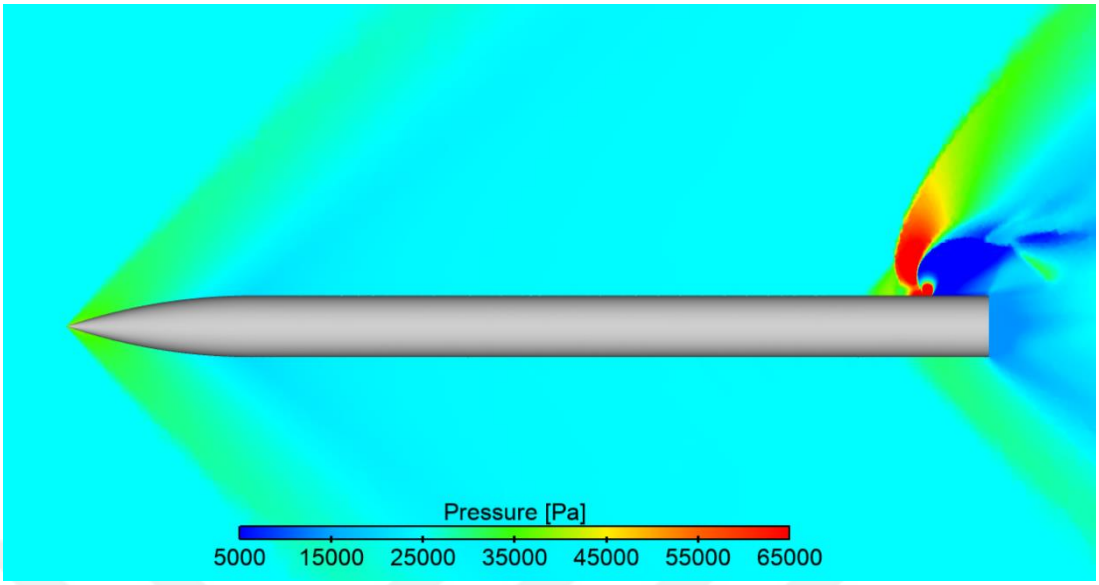

Figure 5.58. Pressure Contours for the Aftjet Operating at M_{jet}=0.7, M_{inf}=1.5

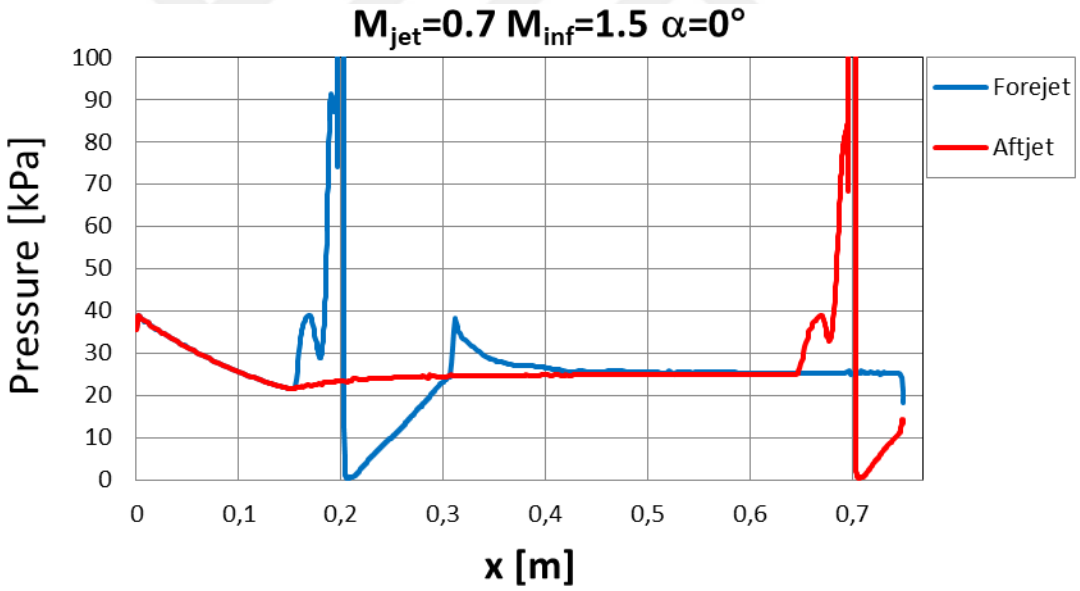

Figure 5.59. Pressure Coefficient Distribution for M_{jet}=0.7 and M_{inf}=1.5

Next, the free-stream flow at a Mach number of 2 is examined using the moment amplification factors which are already presented in Figure 5.27 since the results of free-stream velocity at a Mach number of 2 and zero incidence angle is common for

subsections 5.3 and 5.4. Also it is possible to observe, from Figure 5.27, that the aftjet is better for the all range of examined jet exit velocities, as before.

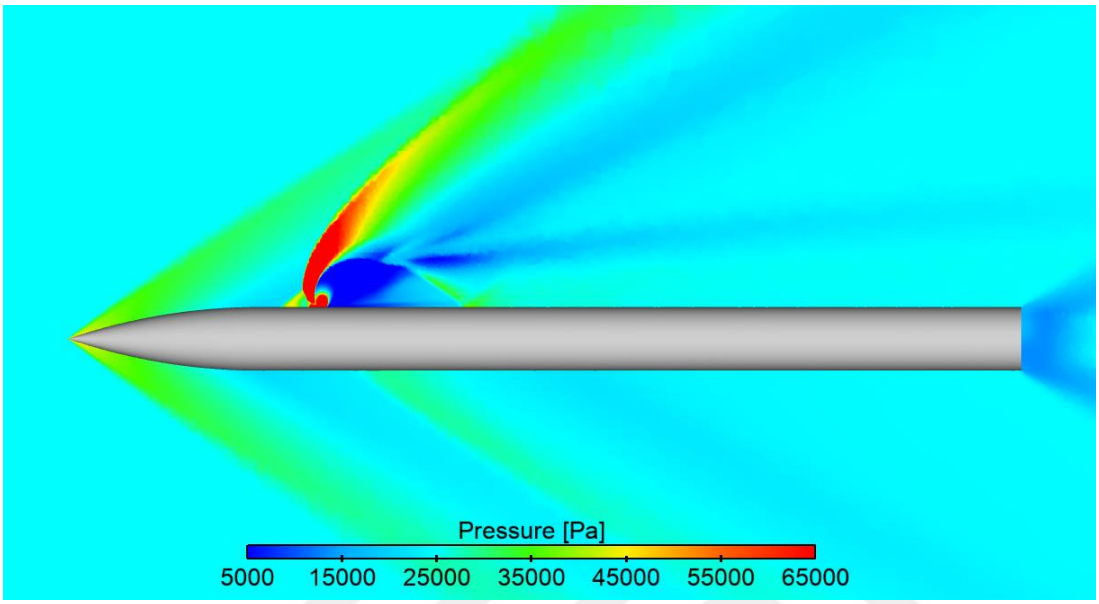

Figure 5.60. Pressure Contours for the Forejet Operating at M_{jet}=0.7, M_{inf}=2

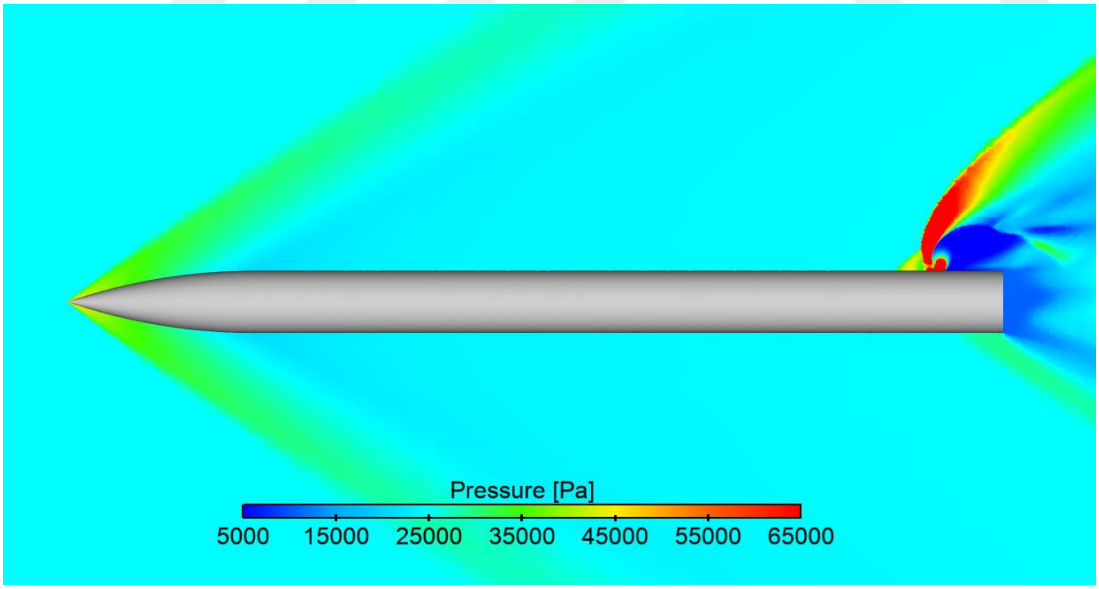

Figure 5.61. Pressure Contours for the Aftjet Operating at M_{jet}=0.7, M_{inf}=2

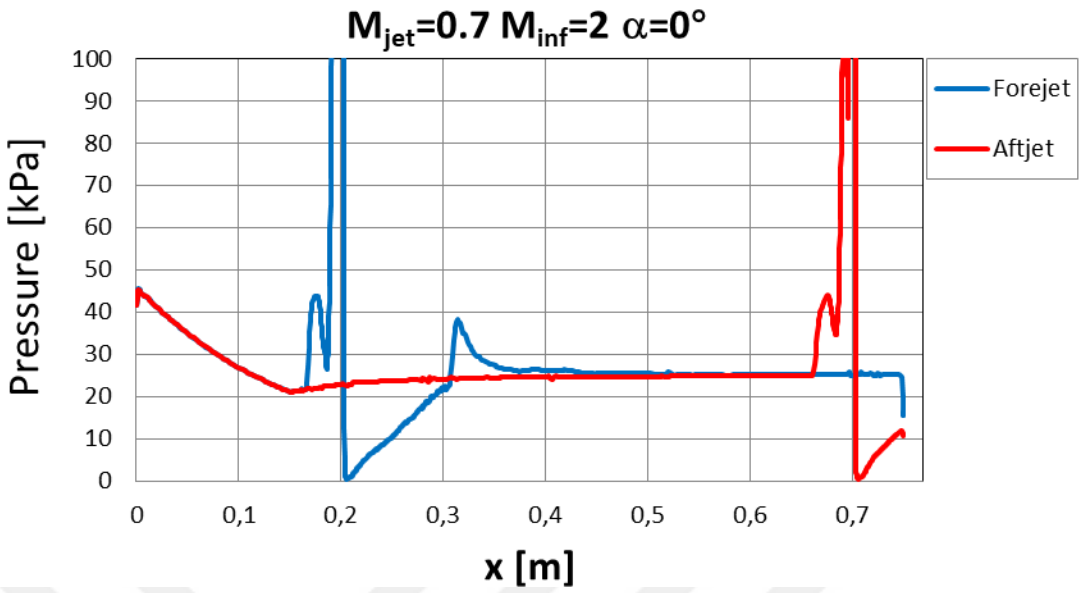

Figure 5.62. Pressure Coefficient Distribution for M_{jet}=0.7 and M_{inf}=2

For jet exit Mach number of 0.7 and a free-stream flow at a Mach number of 2, length of the low-pressure region is 2.12-D for the forejet case and 0.93-D for the aftjet case. The observed shift of the low-pressure region increases the pitching moment coefficient of the aftjet around 9.5% with respect to the one of the forejet. These two flow observations are similar to the ones obtained from Figure 5.32, as it is expected.

Lastly, free-stream flow at a Mach number of 3 for different jet exit speeds is examined with moment amplification factors and the respective graph presented in Figure 5.63, and the aftjet location is better for all range of examined jet exit velocities than the forejet location.

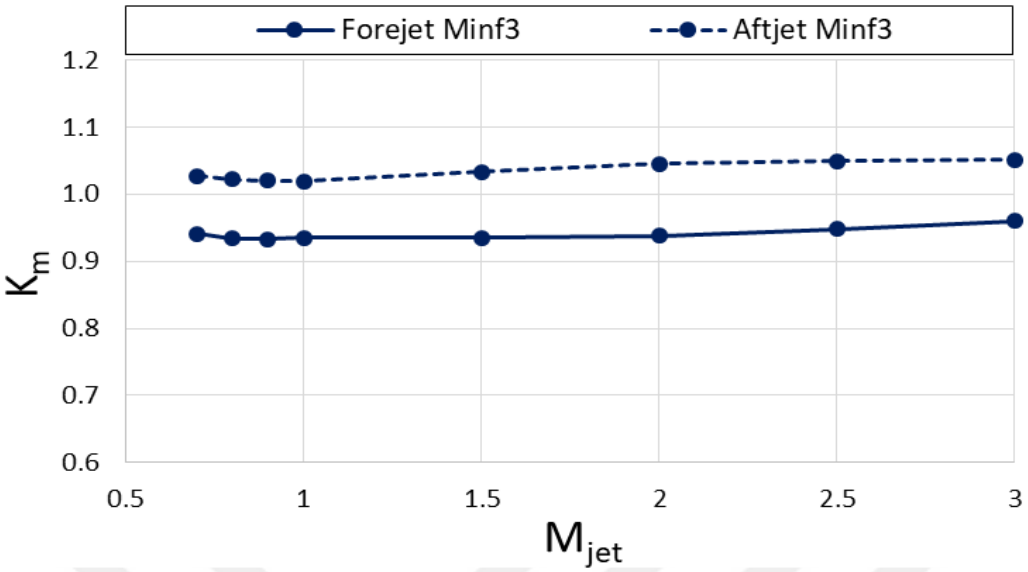

Figure 5.63. K_m Values at Several Jet Exit Velocities and M_{inf}=3

For supersonic jet exit velocities, better performance of the aftjet for a free-stream flow at a Mach number of 3 is explained by wake region shift, as before. In order to examine better performance of the aftjet for subsonic jet flows and free-stream flow at a Mach number of 3, pressure contours and distributions are presented in Figure 5.64, Figure 5.65 and Figure 5.66.

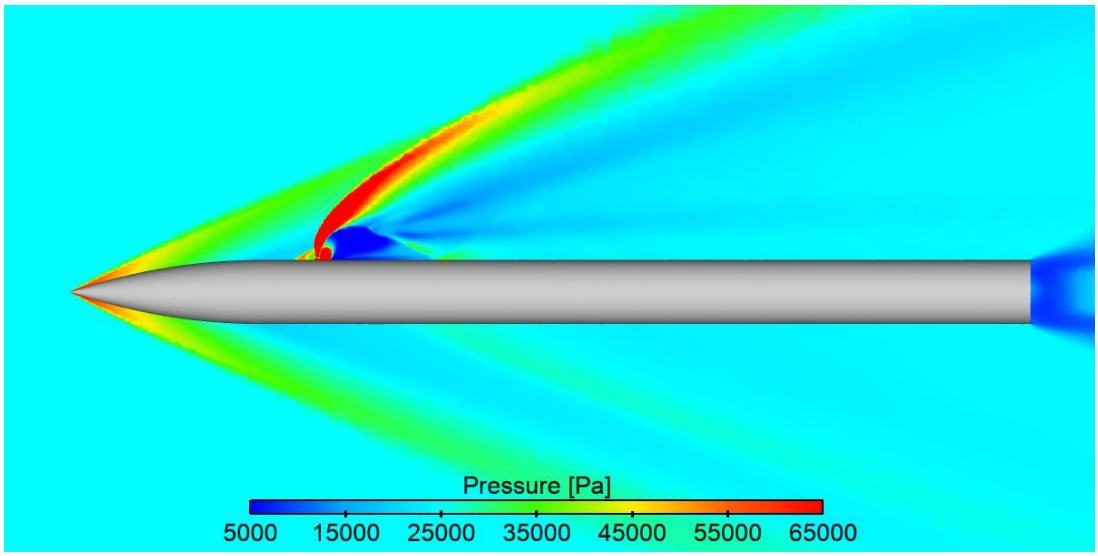

Figure 5.64. Pressure Contours for the Forejet Operating at M_{jet}=0.7, M_{inf}=3

Pressure contours for both jet locations for free-stream and jet flows at a Mach numbers of 0.7 and 3, are obtained and presented in Figure 5.64 and Figure 5.65. Pressure distributions at 180° line for the same flow conditions are presented in Figure 5.66. From the figure it is seen that, wake region length in axial direction is 1.60-D for the forejet case and that for the aftjet case is 0.93-D. Shift of the low-pressure region for M_{jet}=0.7 and M_{inf}=3, increases the pitching moment coefficient of the aftjet around 9.2% with respect to the one of the forejet case.

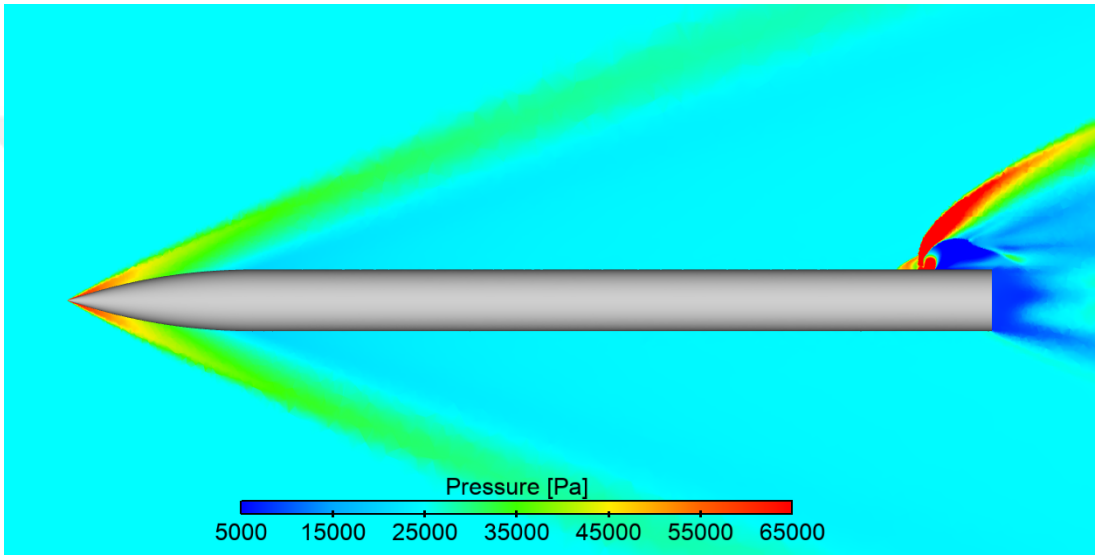

Figure 5.65. Pressure Contours for the Aftjet Operating at M_{jet}=0.7, M_{inf}=3

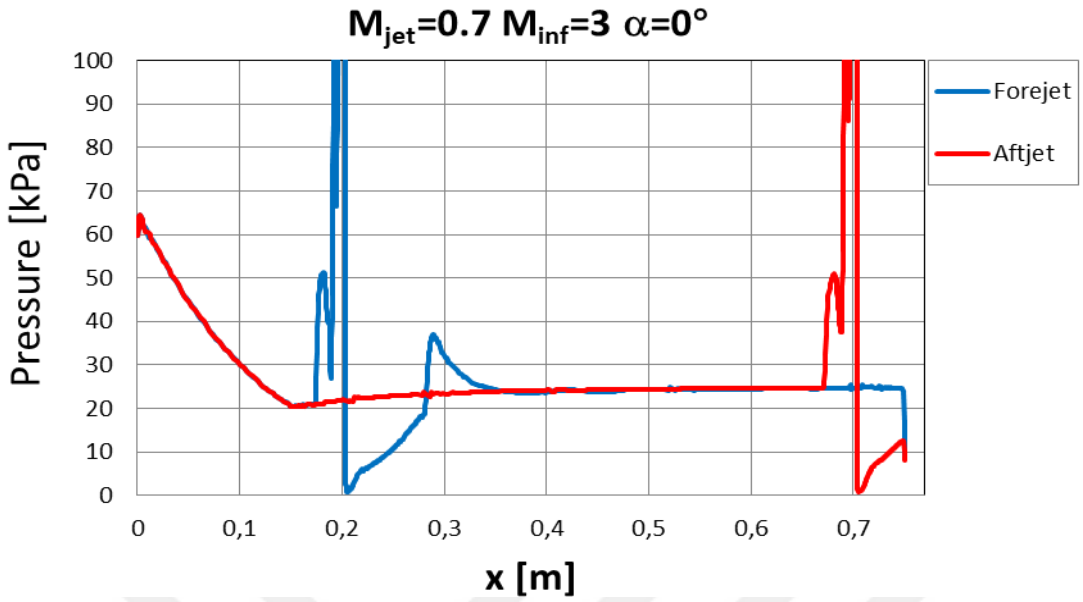

Figure 5.66. Pressure Coefficient Distribution for M_{jet}=0.7 and M_{inf}=3

5.5. Discussion

In this section, conducted parametric studies are presented. First, spouting angle effect is investigated, and concluded that, better flow interactions are obtained by changing the spouting angle while deflecting jet decreases jet performance drastically. At the end of this sub-section, it is decided to use a jet spouting at normal angle.

Next, effect of free-stream flow velocity on the supersonic jet exit velocity is investigated using the force and moment coefficients and their respective amplification factors. For relatively low free-stream velocities it is seen that, aftjet results in higher performance, while forejet results in higher performance for greater free-stream velocities. At greater free-stream velocities, reattachment shock at the downstream of the forejet and it increases the forejet performance.

At the last two sections, effect of the jet exit velocity is investigated at several free-stream flow velocities and incidence angles. At sonic and supersonic jet exit speeds,

aftjet shows a greater performance which is due to shift of low-pressure region to the out of the missile. For subsonic jet exit velocities and the cases zero incidence angle and ‘Jet – Body’, shift of the low pressure region increases performance of the aftjet case. Furthermore, for subsonic jet exit velocities and ‘Jet + Body’ case, both jet locations resulted in similar performances. However physical comments could not be obtained for the similar performance of the jet locations and commented that a further study on the subsonic lateral jets should be conducted in order to have a deeper understanding on the flow behavior at the subsonic jet exit velocities.

CHAPTER 6

CONCLUSION AND SUGGESTIONS FOR FUTURE WORK

6.1. Conclusion

Lateral jet control gives the ability of high maneuverability to the missile. Nevertheless, it results in strong interactions with other missile components due to its complicated flow domain. For a better insight about interactions, flow domain is explained in detail in the first part of the study. The performance of the lateral jet installed missile should be determined with the wind tunnel tests or numerical simulations. Numerical simulation is a cost-effective solution due to the advances in computers and CFD software over the years.

Additionally, numerical simulation requires a validation in order to prove that the grid, turbulence modelling, boundary condition definitions, etc. are adequate for solving the flow domain. In this study, a generic missile geometry with lateral jet obtained from literature is used for validation. Results of the validation study proved that the numerical simulation estimates the flow domain sufficiently close to the experimental results except some deviations. The deviations are observed especially at the reattachment shock region. From the general point of view, the CFD technique solves the jet in cross-flow case accurately.

Next, a parametric study for lateral jet installed missiles are conducted using a generic missile geometry and validated numerical simulation method. The aim of the parametric study is to determine the behavior of the interactions of jet and free-stream flows under several conditions and provide a database to the designer for the conceptual design phase of lateral jets. In this study, pitching moment is selected as a performance parameter since it expresses the maneuverability of the missile.

In the first phase of the parametric study, spouting angle of the jet flow is examined at the several free-stream flow velocities and incidence angles. It is concluded that, changing spouting angle of the jet may result in a positive interaction of the jet and free-stream flows. Meanwhile, changing the jet spouting angle decreases the vertical component of the jet thrust. In total, decrease of the vertical component of the jet thrust dominates the positive change of the flow interactions and pitching moment decreases. Therefore, 90° jet spouting angle is selected and used for the rest of the study.

At the second phase of the parametric study, effect of the free-stream flow velocity is examined. For low supersonic free-stream velocities, use of the aftjet results in a better maneuverability. This is explained by the shift of the low-pressure region to the out of the missile which is the wake region. At higher free-stream flow velocities, the forejet shows higher performance. It is observed that the higher performance of the forejet is caused by the reattachment shock that occurs at the downstream of the forejet.

In the final phase of the parametric study, the jet flow velocity is examined at several angles of attack and free-stream flow velocities. For sonic and supersonic jet flow velocities, the aftjet results in higher performance due to the shift of the low-pressure region, as explained before. Also, with increasing jet exit velocity, jet performance increases. Moreover, jet performance drops at sonic and subsonic jet exit velocities, as expected. Even little changes in the interaction of the flows influence the overall jet performance since the jet creates less thrust at subsonic and sonic jet flow velocities than the one for supersonic jet flow velocities.

6.2. Suggestions for Future Work

Based on the results presented by this study, investigations about lateral jets can be extended. A further study on lateral jets operating at subsonic velocities can be studied for an extensive understanding on the jet flow behavior at subsonic jet flow velocities. The numerical simulation technique used in the thesis can be used in this future study.

In the current study, jet and free-stream flow interactions are inspected with only missile body, and effect of jet on the aerodynamic surfaces are excluded from this study. Another future study may be conducted for the inspection of the jet effect on the aerodynamic surfaces.

Moreover, modelling of the internal flow in conjunction with the external flow may be another subject of the future studies.

Finally, more advanced turbulence models like, Detached Eddy Simulation, Large Eddy Simulation, etc. might be used for the jet in the cross-flow cases, when feasible computational times are applicable for these turbulence models with the help of the development in the high-performance computing systems.

REFERENCES

Ağsarlıoğlu, E. (2011). *Numerical Investigations of Lateral Jets for Missile Aerodynamics*. Middle East Technical University.

Anderson, J. D. (2017). *Fundamentals of Aerodynamics* (6th ed.). McGraw-Hill Education.

Ansys Inc. (2006). *Modeling of Turbulent Flows*. Retrieved from http://www.southampton.ac.uk/~nwb/lectures/GoodPracticeCFD/Articles/Turbulence_Notes_Fluent-v6.3.06.pdf

Ansys Inc. (2013). Ansys Fluent Theory Guide.

Arnold Engineering Development Center. (1976). *An Approximate Analysis of the Shock Structure in Underexpanded Plumes*.

Atak, B. (2012). *Slotlu Roket/Füze Modelleri İçin Aerodinamik Performans Kestirim Yöntemlerinin İyileştirilmesi*. İstanbul Technical University.

Bagley, C. J. (1990). *US4967982*. US.

Blazek, J. (2001). *Computational Fluid Dynamics: Principles and Applications* (1st ed.). Elsevier Science.

Cassel, L. A. (2003). Applying Jet Interaction Technology. *Journal of Spacecraft and Rockets*, *40*(4), 523–537. https://doi.org/10.2514/2.3992

Chang, I. S., & Chow, W. L. (1974). Mach Disk from Underexpanded Axisymmetric Nozzle Flow. *AIAA Journal*, *12*(8), 1079–1082. https://doi.org/10.2514/3.49415

Christie, R. (2010). *Lateral Jet Interaction with a Supersonic Crossflow*. Cranfield University.

Defense Industry Daily. (n.d.). No Title. Retrieved from https://www.defenseindustrydaily.com/i-think-i-camm-britains-versatile-air-defense-missile-07293/

DeSpirito, J. (2015). *Turbulence Model Effects on Cold-Gas Lateral Jet Interaction in a Supersonic Crossflow*. *Journal of Spacecraft and Rockets* (Vol. 52). https://doi.org/10.1016/S0294-1449(16)30238-4

Eckerle, W. A., & Langston, L. S. (1986). Horseshoe Vortex Formation Around a Cylinder. In *International Gas Turbine Conference and Exhibit*. Dusseldorf. https://doi.org/10.1115/1.3262098

Edgington-Mitchell, D., Honnery, D. R., & Soria, J. (2014). The Underexpanded Jet Mach Disk and its Associated Shear Layer. *Physics of Fluids*, *26*. https://doi.org/10.1063/1.4894741

Erdem, E. (2006). *Thrust Vector Control by Secondary Injection*. Middle East Technical University.

Fleeman, E. L. (2006). *Tactical Missile Design* (2nd ed.). American Institute of Aeronautics and Astronautics Inc.

Gerhart, P. M., Gerhart, A. L., & Hochstein, J. I. (2015). *Fundamentals of Fluid Mechanics* (8th ed.). Wiley.

Gligorijevic, N., Zivkovic, S., Subotic, S., Kozomara, S., Nikolic, M., & Citakovic, S. (2013). Side Force Determination in the Rocket Motor Thrust Vector Control System. *Scientific Technical Review*, *63*(1), 27–38.

Global Security. (n.d.). No Title. Retrieved from https://www.globalsecurity.org/military/library/budget/fy2000/dot-e/other/00thaad.html

Gnemmi, P. (2008). Computational Comparisons of the Interaction of a Lateral Jet on a Supersonic Generic Missile, (August), 1–9. https://doi.org/doi:10.2514/6.2008-6883

Hamed, A., & Kumar, A. (1994). Flow Separation in Shock Wave Boundary Layer Interactions. *Journal of Engineering for Gas Turbines and Power*, *116*, 98–103. https://doi.org/10.1115/1.2906816

Honeywell Inc. (2010). *Precision Control Technologies for Strategic Applications*.

Honeywell Inc. (2016). No Title. Retrieved from https://aerospace.honeywell.com/en/~/media/aerospace/files/brochures/n61-1575-000-000-actuationsolutions-bro.pdf

Irie, T., Yasunobu, T., Kashimura, H., & Setoguchi, T. (2003). Characteristics of the Mach Disk in the Underexpanded Jet in which the Back Pressure Continuously Changes with Time. *Journal of Thermal Science*, *12*(2), 132–137. https://doi.org/10.1007/s11630-003-0054-4

Jacquin. (1994). Phenomenological Description and Simplified Modelling of the Vortex Wake Issuing from a Jet in a Crossflow. *La Recherche Aerospatiale*.

Kostić, O., Stefanović, Z., & Kostić, I. (2017). Comparative CFD Analyses of a 2D Supersonic Nozzle Flow with Jet Tab and Jet Vane. *Tehnički Vjesnik*, *24*(5), 1335–1344. https://doi.org/10.17559/TV-20160208145336

Kovar, A., & Schülein, E. (2006). Effect of Side Jets in a Supersonic Flow Measured and Calculated on a Flat Plate and a Generic Missile Configuration. In *RTO-MP-AVT-135* (pp. 1–16).

Krishnan, S., Jouhari, A. K., & Balu, R. (2016). Numerical Simulation of Lateral Control Jets of an Interceptor Missile. *International Journal of Research in Engineering and Technology*, 189–193.

Lee, J., Min, B., & Byun, Y. (2004). Numerical Analysis and Design Optimization of Lateral Jet Controlled Missile. *XXI International Congress of Theoretical and Applied Mechanics*. Retrieved from http://fluid.ippt.gov.pl/ictam04/php/ext_www/abstract_view.php?id=1074

Li, X., Zhou, R., Yao, W., & Fan, X. (2017). Flow Characteristic of Highly Underexpanded Jets from Various Nozzle Geometries. *Applied Thermal Engineering*, *125*, 240–253. https://doi.org/10.1016/j.applthermaleng.2017.07.002

Lin, C., Ho, T. C., & Dey, S. (2008). Characteristics of Steady Horseshoe Vortex System near Junction of Square Cylinder and Base Plate. *Journal of Engineering Mechanics*, *134*(2), 184–197. https://doi.org/10.1061/(ASCE)0733-9399(2008)134:2(184)

Lockheed Martin. (n.d.). No Title. Retrieved from https://www.lockheedmartin.com/content/dam/lockheed-martin/mfc/photo/pac-3/rotator/mfc-pac-3-photo-02-h.jpg

Mazumdar, A. (2013). *Principles and Techniques of Schlieren Imaging Systems*.

MBDA Systems. (n.d.). No Title. Retrieved from https://www.mbda-systems.com/product/aster-15-30/

Min, B. Y., Lee, J. W., & Byun, Y. H. (2006). Numerical Investigation of the Shock Interaction Effect on the Lateral Jet Controlled Missile. *Aerospace Science and Technology*, *10*, 385–393. https://doi.org/10.1016/j.ast.2005.11.013

Moog Inc. (2017). *Precision Missile Steering*.

Orth, R. C., & Funk, J. A. (1967). An Experimental and Comparative Study of Jet Penetration in Supersonic Flow. *J. Spacecraft*, *4*(9), 1236–1242. https://doi.org/10.2514/3.29058

P. Champigny, R. G. L. (1994). *Special Course on Missile Aerodynamics*. *Agard Report 804*.

Pakistan Defence. (2012). No Title. Retrieved from https://defence.pk/pdf/threads/land-based-version-of-camm-flaads.165132/

Preston, K. G., Leal, M. A., Wilson, R. J., & Hussey, R. C. (2014). *US8735788*. US.

Sau, A., Sheu, T. W. H., Hwang, R. R., & Yang, W. C. (2004). Three-dimensional Simulation of Square Jets in Cross-Flow. *American Physical Society*. https://doi.org/10.1103/PhysRevE.70.019902

Schlichting, H., & Gersten, K. (2017). *Boundary Layer Theory* (9th ed.). Springer-Verlag. https://doi.org/10.1007/978-3662-52919-5

Sozer, E., Brehm, C., & Kiris C., C. (2014). Gradient Calculation Methods on Arbitrary Polyhedral Unstructured Meshes for Cell-Centered CFD Solvers. In *52nd Aerospace Sciences Meeting*. https://doi.org/10.2514/6.2014-1440

Spaid, F. W., & Zukoski, E. E. (1968). A Study of the Interaction of Gaseous Jets from Transverse Slots with Supersonic External Flows. *AIAA Journal*, *6*(2), 205–212. https://doi.org/10.2514/3.4479

Stahl, B., Emunds, H., & Gülhan, A. (2009). Experimental Investigation of Hot and Cold Side Jet Interaction with a Supersonic Cross-flow. *Aerospace Science and Technology*, *13*(8), 488–496. https://doi.org/10.1016/J.AST.2009.08.002

Stahl, B., Esch, H., & Gülhan, A. (2008). Experimental Investigation of Side jet interaction with a Supersonic Cross-Flow. *Aerospace Science and Technology*, *12*, 269–275. https://doi.org/10.1016/j.ast.2007.01.009

Viti, V., Neel, R., & Schetz, J. A. (2009). Detailed Flow Physics of the Supersonic Jet Interaction Flow Field. *Physics of Fluids*, *21*(4), 1–16. https://doi.org/10.1063/1.3112736

Viti, V., Wallis, S., Schetz, J. a., Neel, R., & W. Bowersox, R. D. (2004). Jet Interaction with a Primary Jet and an Array of Smaller Jets. *AIAA Journal*, *42*(7), 1358–1368. https://doi.org/10.2514/1.4850

Zhang, J.-M., Cai, J., & Cui, Y. (2009). Effect of Nozzle Shapes on Lateral Jets in Supersonic Cross-flows. *AIAA Journal*. https://doi.org/10.2514/6.2009-1477

Zhen, H., Gao, Z., & Lee, C. (2013). Numerical Investigation on Jet Interaction with a Compression Ramp. *Chinese Journal of Aeronautics*, *26*(4), 898–908. https://doi.org/10.1016/j.cja.2013.04.026

APPENDICES

A. Jet Flow Calculations

At the beginning of the conducted parametric study, the jet exit velocity is selected as one of the parameters. In this section, the calculations made for the jet flow properties are given. First, missile cruise speed is selected as Mach 2 at an altitude of 10.4 km. At that altitude flow properties of standard atmosphere are $P_{inf} \approx 25$ kPa and $T_{inf} \approx$ 220.7 K (Anderson, 2017). And jet exit and free-stream temperatures are assumed to be equal in order to exclude the effect of the heat transfer. Furthermore, side jet strength (or pressure ratio) PR is selected as 200 which is the ratio between the total pressure of jet flow and the static pressure of the free-stream flow. Hence, total jet pressure ($P_{jet,0}$) and static pressure of the jet flow (P_{jet}) is found approximately as 5 MPa and 639 kPa, respectively. Next, using the set of formulas which are given in the Equation 4.2 speed of sound and density at the jet exit are calculated. Using the variables speed of sound and density, mass flow rate of the jet is found approximately as 0.2312 kg/s using the Equation 4.1.

In the examination of jet exit flow velocity, jet exit area (A_{jet}) and mass flow rate is constant while the pressure at the jet exit (P_{jet}) is varying for different Mach numbers of jet flow. Calculation of the flow properties is summarized in the following. Mass flow rate, jet exit temperature (T_{jet}) and area (A_{jet}) are known, hence density of the flow at the jet exit (ρ_{jet}) is calculated using the Equation 4.1. Finally, jet exit pressure (P_{jet}) is calculated by using the equation of state for the full definition of the jet flow. Calculated jet flow properties for examined jet exit velocities are presented in the Table 0.1.

Table 0.1. *Summary of the Jet Flow Properties*

P_{jet} [kPa]	T_{jet} [K]	M_{jet}	$\dot{m}$ [kg/s]
1825.7	220.7	0.7	0.2312
1597.5	220.7	0.8	0.2312
1420.0	220.7	0.9	0.2312
1278.0	220.7	1	0.2312
852.0	220.7	1.5	0.2312
639.0	220.7	2	0.2312
511.2	220.7	2.5	0.2312
426.0	220.7	3	0.2312